

UNIVERSIDAD DE ANTIOQUIA
FACULTAD DE CIENCIAS EXACTAS Y NATURALES
INSTITUTO DE FÍSICA

THE PLACE OF THE MILKY WAY AND ANDROMEDA IN THE COSMIC WEB

Sebastian Bustamante Jaramillo

Facultad de Ciencias Exactas y Naturales
Instituto de Física

Advisor: Jaime E. Forero-Romero

Co-advisor: Jorge I. Zuluaga



UNIVERSIDAD DE ANTIOQUIA
FACULTAD DE CIENCIAS EXACTAS Y NATURALES
INSTITUTO DE FÍSICA

THE PLACE OF THE MILKY WAY AND ANDROMEDA IN THE COSMIC WEB

Sebastian Bustamante Jaramillo

Facultad de Ciencias Exactas y Naturales
Instituto de Física

Advisor: Jaime E. Forero-Romero

Co-advisor: Jorge I. Zuluaga

Student

Advisor

Co-advisor

Medellín, January 2013

to my family, my girlfriend and my friends.

The place of the Milky Way and Andromeda in the cosmic web

Author: Sebastian Bustamante

Advisor: Jaime E. Forero-Romero

Co-advisor: Jorge I. Zuluaga

In the next link it could be found updated information about this work and some topics related to it:

<https://github.com/sbustamante/Thesis>

Printed in Medellín, Colombia

First edition, january 2013

Abstract

As it has been widely demonstrated from observations and cosmological simulations, the present universe harbours a complex large-scale structure of entangled filaments of clumped matter permeated by vast low-density regions. This structure is called cosmic web and is one of the mainly emergent features of the non-linear regime of the universe. Numerous studies have been performed aimed to quantify the effects of the cosmic web on different physical properties of systems like dark matter halos, galaxies and galaxy clusters. Some important correlations have already been found for some of those properties, such as the mass of the halos, the spin parameter and their shape. There is also a growing interest in studying the properties of the local group of galaxies (dominated gravitationally by the Milky Way and Andromeda galaxy) in a cosmological context as a test of the standard cosmological model.

Motivated to continue this line of research, the current work is pointed to study LG-like systems in a set of dark matter cosmological simulations in a cosmological context. It is used three constrained simulations (CLUES) aimed to mimic our local environment and an unconstrained simulation (Bolshoi) used for the statistic treatment. As one of the key proposals of this work is to introduce a new method for constructing LG-like systems in simulations by using the V-web scheme to classify the local environment in the constrained simulations. It is demonstrated that the LG-like sample constructed by this way is consistent and has biases in some physical properties with respect to the distribution of halos. Specially, it is found that unlike halos, which are formed in high-density regions, LG-like systems rather lie in low-density regions, like voids and sheets.

Contents

| | |
|--|-----------|
| List of Figures | v |
| 1 Preliminaries | 1 |
| 1.1 Prehistory | 1 |
| 1.2 The Current Cosmology Picture | 4 |
| 1.3 Cosmological Observations | 8 |
| 2 Theoretical Framework in Cosmology | 11 |
| 2.1 Isotropic and Homogeneous Universe | 11 |
| 2.1.1 Metric of Curved Spaces | 12 |
| 2.1.2 General Relativity and Friedmann's Equations | 16 |
| 2.1.3 Simple Solutions of the Universe | 18 |
| 2.2 Linear Regime of Structure Formation | 22 |
| 2.2.1 Newtonian Approximation | 23 |
| 2.2.2 Jeans Instability | 26 |
| 2.2.3 Statistical Properties and Transfer Function | 31 |
| 2.3 Non-Linear Regime of Structure Formation | 37 |
| 2.3.1 Zeldovich Approximation | 38 |
| 3 Computational Methods in Cosmology | 41 |
| 3.1 N-body Simulations | 42 |
| 3.1.1 P-P Method | 43 |
| 3.1.2 PM Method | 44 |
| 3.1.3 P ³ M Method | 46 |

CONTENTS

| | | |
|---------------------|---|-----------|
| 3.2 | Types of Simulations | 48 |
| 3.2.1 | Unconstrained Simulations (Bolshoi) | 49 |
| 3.2.2 | Constrained Simulations (CLUES) | 51 |
| 3.3 | Environment Characterization | 54 |
| 3.3.1 | T-web Scheme | 54 |
| 3.3.2 | V-web Scheme | 56 |
| 3.4 | Detecting Halos and Defining the Samples | 58 |
| 3.4.1 | FOF Method | 58 |
| 3.4.2 | Defining the Samples | 60 |
| 3.4.3 | Method to Detect Pairs | 63 |
| 4 | The Cosmological Environment and the Local Group | 65 |
| 4.1 | Properties of the Simulations | 65 |
| 4.1.1 | Halo Mass Function | 66 |
| 4.1.2 | Distributions of the Cosmological Environment | 68 |
| 4.2 | Properties of the <i>CLG</i> Sample | 73 |
| 4.2.1 | Determining the Environment | 73 |
| 4.2.2 | Mass of <i>CLG</i> Systems | 79 |
| 4.2.3 | Distributions of Energy and Angular Momentum | 83 |
| 4.2.4 | Angular Momentum Alignment | 85 |
| 4.3 | Conclusions | 86 |
| Bibliography | | 89 |

List of Figures

| | | |
|-----|--|----|
| 1.1 | William Herschel's model for our galaxy based upon a count of stars with the assumption of equal intrinsic luminosity. [14]. | 2 |
| 1.2 | Different geometries according to variations on Euclid's fifth postulate. | 4 |
| 1.3 | Cosmic background radiation. Taken from http://upload.wikimedia.org/wikipedia/commons/3/3c/I1c_9yr_moll4096.png | 5 |
| 1.4 | Local Group. Taken from http://commons.wikimedia.org/wiki/File:Local_Group.svg | 7 |
| 1.5 | Map of the large-scale universe according to the Sloan Digital Sky Survey. Taken from the official web page of the project http://www.sdss.org/ | 9 |
| 2.1 | Metric of a spherical surface. | 12 |
| 2.2 | Curved spaces according to the curvature parameter. | 13 |
| 2.3 | Different solutions of the universe according to the Friedmann's equations. | 22 |
| 2.4 | Evolution of the Jean mass for different stages of the universe. Coloured regions illustrate the typical mass range of some types of structures, since open stellar clusters to superclusters of galaxies. | 29 |
| 2.5 | Evolution of the normal modes of the density field. For the sake of the illustration, each solution has been normalized with respect to the initial conditions. | 31 |
| 2.6 | Initial distribution of perturbations for the density contrast field from the Gaussian distribution 2.57 and the Harrison-Zeldovich power spectrum $\sigma_k \propto k$ | 33 |

LIST OF FIGURES

| | | |
|-----|--|----|
| 2.7 | Transfer function for cold dark matter perturbations at the current epoch [26] (left panel). Comparison between the initial power spectrum, Harrison-Zeldovich spectrum and the processed power spectrum (right panel) | 36 |
| 2.8 | Evolution of a dark matter numerical simulation in a comoving volume of $(40 \text{ Mpc}/h)^3$, starting from a high homogeneity stage (upper left panel), until the present epoch with highly non-linear structures (lower right panel). Taken from http://www.astro.utu.fi/research/CosmoS/lss/lss_p1.shtml | 37 |
| 2.9 | Comparison of the evolution in non-linear regime between a N-body simulation (a) and the Zeldovich approximation (b). In both cases are used the same initial conditions. Taken from [26]. | 39 |
| 3.1 | Formulation of the N-body problem. | 42 |
| 3.2 | Illustrative diagram of the PM method. The map that is plotted over the distribution of particles corresponds to the density field evaluated in each cell of the grid. Dark cells corresponds to overdensity regions whereas white cells to lower values of the density field, which agrees with the amount of mass of the particles per cell. | 44 |
| 3.3 | Illustrative diagram of the P ³ M method. For the reference particle, shown in the center, interactions with distant particles is calculated through the PM method, whereas for close particles (gray and white regions), the interaction is calculated by using the PP method. | 46 |
| 3.4 | An illustrative example of the building of a tree code for a N-body simulation. Upper panels show the iterations for a 2D problem whereas lower panel illustrates the resultant tree built using each particle of the simulation. | 47 |
| 3.5 | Evolution of the Bolshoi simulation. It is illustrated the density field in a rectangular volume of $16 \text{ Mpc}/h$ of thick and $250 \text{ Mpc}/h$ of side for different stages of the evolution. $z = 9.5$ (upper left), $z = 3$ (upper right), $z = 1$ (lower left) y $z = 0$ (lower right). Taken from http://spectrum.ieee.org/aerospace/astrophysics/the-cosmological-supercomputer | 50 |

LIST OF FIGURES

| | | |
|------|--|----|
| 3.6 | Initial density and peculiar velocity field built by using constraints in order to reproduce the local environment at a scale of $160 h^{-1}\text{Mpc}$. Some of the identified structures are: <i>Coma</i> , coma cluster, <i>PP</i> , Perseus-Pisces supercluster, <i>LS</i> , local supercluster, <i>GA</i> , the great attractor. The upper arrow indicates the scale of the peculiar velocities field as 1000 km/s. Taken from [22]. | 51 |
| 3.7 | Three constrained simulations of the CLUES project where it is possible to identify systems like the local group. It is illustrated the density field of each simulations along with the dark matter halos (black dots), and the LG-like systems found (red points). | 52 |
| 3.8 | An example of a simulation of the CLUES project. In this figure it is shown the large-scale structures of the local universe and it can be appreciated clearly the most significant members of the Local Group. Taken from the official webpage of the project http://www.clues-project.org | 53 |
| 3.9 | Classification scheme for the cosmological environment for both T-web and V-web schemes. The threshold value λ_{th} is taken as free parameter. | 56 |
| 3.10 | It is illustrated for each one of the simulations (CLUES 1, CLUES 2, CLUES 3, Bolshoi) the difference between both classification schemes, T-web and V-web, and for different threshold values λ_{th} (Black - Knot, Dark gray - Filament, Gray - Sheet, White - Vacuum). In the upper figures it is shown the visual impression obtained from the respective density fields ($\log(\delta + 1)$), these impressions are used to calibrate the threshold value λ_{th} . The resolution of the used grid in each simulation is approximately $1.0h^{-1} \text{ Mpc}/\text{cell}$ and for each one it is performed a Gaussian softening of one cell size. The width of each slide is one cell. | 57 |
| 3.11 | Illustrative diagram of the FOF method. Gray circles around each particle represents the linking region and the red curve represents one of the bounded structures found by the method. | 59 |
| 3.12 | Halos detected by using the FOF scheme for one of the CLUES simulations. The color gradient indicates the depth with respect to the x axe, where black dots are the nearest halos. | 60 |

LIST OF FIGURES

| | | |
|------|---|----|
| 3.13 | Cosmological environment obtained by using the V-web scheme (with $\lambda_{th} = 0.3$) for each one of the LG-like systems in the CLUES simulations (red dots). | 62 |
| 3.14 | Two-dimensional of the method for detecting the pair samples. Random distribution of a set of dark matter halos (left), definition of cells (right). | 64 |
| 4.1 | Spatial distribution of dark matter halos, exhibiting the characteristic structure of the cosmic web. The colour gradient indicates the depth with respect to the x axis, where black dots are the nearest halos. | 66 |
| 4.2 | Cumulative mass functions of the dark matter halos (<i>GH</i> sample) for each simulation. | 67 |
| 4.3 | Distributions of eigenvalues of the V-web scheme calculated over all the volume cells (continuous lines) and over the host cells of the dark matter halos defined in the FOF catalogue (dashed lines). All the distributions are normalized such that their area is the unity. Resolution of $1.0h^{-1}$ Mpc/cell and softening parameter of one cell size. | 68 |
| 4.4 | Mean density parameter for different type of regions in terms of the threshold value λ_{th} (left panels). Volume fractions normalized for different type of regions, also according to the threshold value λ_{th} (right panels). . | 70 |
| 4.5 | Comparison between the visual impression obtained by the V-web scheme for several values of the threshold parameter λ_{th} . It is used the next classification scheme (Black - Knot, Dark gray - Filament, Gray - Sheet, White - Vacuum). The resolution of each grid is $1.0h^{-1}$ Mpc/cell with a Gaussian softening of one cell size. The width of each slide is one cell. . . . | 71 |
| 4.6 | Pathological situation regarding the environment of a pair system. . . . | 73 |
| 4.7 | Comparison between the distributions of the eigenvalues of the V-web for the two halos of each pair system of the <i>LG</i> , <i>CLG</i> and <i>IP</i> samples. . . . | 74 |

LIST OF FIGURES

| | |
|--|----|
| 4.8 2D distributions of the cosmological environment for the defined samples, $\lambda_1-\lambda_3$ (left panel) and $\lambda_1-\lambda_2$ (right panel). The background histogram, plotted in colours, corresponds to the distribution of environment for all the halos in Bolshoi (<i>GH</i> sample), its resolution is 100×100 for the shown range and it is normalized with respect to its area. The black dots corresponds to the distribution of the <i>IP</i> sample and finally the white dots to the <i>CLG</i> sample. | 75 |
| 4.9 Object fractions in different regions in terms of the threshold value λ_{th} . In the case of the <i>GH</i> sample, it is counted the number of halos, whereas for the <i>IP</i> and <i>CLG</i> samples it is counted the number of pair systems. | 77 |
| 4.10 Integrated histogram of the fractional anisotropy for the <i>IP</i> and <i>CLG</i> samples. | 78 |
| 4.11 Integrated histograms for the total mass $M_A + M_B$ (left panel) and the mass ratio M_B/M_A (right panel), of the pair samples in Bolshoi. | 80 |
| 4.12 Diagram of dispersion for the defined mass parameters (M_{tot}, χ) and for each one of the pair samples. The square regions are made from the mean value and the standard deviation of the respective sample (same colour). The gray regions in the bottom corresponds to a cut off artificially imposed due to the minim mass range of the halos (M_*) for constructing the pair samples. | 81 |
| 4.13 Diagrams of dispersion for the fractional anisotropy with respect to the mass parameters. The background map and the contour curves correspond to the <i>IP</i> sample. | 82 |
| 4.14 Diagram of dispersion for the total energy and the orbital angular momentum of pair systems. The background map corresponds to the distribution of the <i>P</i> sample, while the contour lines to the distribution of the <i>IP</i> sample, in both cases the value corresponds to the number of pairs. | 83 |
| 4.15 Diagrams of dispersion for the fractional anisotropy with respect to the energy and the angular momentum. The background map and the contour curves correspond to the number of pairs of the <i>IP</i> sample. | 84 |

LIST OF FIGURES

- 4.16 Integrated histograms for the angle formed between the angular momentum of each pair, that determines the orbital plane, and each one of the eigen-vectors defined by the V-web regarding the cosmological environment. It is performed for each one of the pair samples, *IP* and *CLG*, whereas the *LG*systems in CLUES are plotted with vertical red dashed lines. 85

“Equipped with his five senses, man explores the universe around him and calls the adventure Science”

Edwin Hubble

CHAPTER

1

Preliminaries

“What is our place in the cosmos?” This is one of the simpler and transcendental question that human beings have wondered from ancient times; furthermore, this, being powered by our innate curiosity, has led to a relatively understandable and structured picture of our Universe. Despite of that, this knowledge is very new regarding our whole history, so the astronomy can only be considered as a scientific rigorous discipline since the seventeenth century.

1.1 Prehistory

Almost in every scientific discipline, a significant theoretical development is accompanied by a technical and instrumental improvement. That is why at the beginning of the seventeenth century, Johannes Kepler could establish his three well-known empirical laws of the planetary movements based upon the very precise data of astronomical bodies compiled by Tycho Brahe. This event was very remarkable in the history of the astronomy since it was the first of many strikes against the well established anthropocentric notion of the cosmos. Although Kepler’s laws constituted the most crucial test to the Nicolaus Copernicus’s heliocentric model, it was only until 1685, when Isaac Newton formulated the law of universal gravitation (from which can be derived all the Kepler’s laws), when the astronomers could

1. PRELIMINARIES

count with enough powerful theoretical tools to start a depth and serious discussion about the real nature of our universe on scales bigger than the solar system, and thus inaugurating the *sciences of gravity* [26].

After the establishment of the law of universal gravitation, the next significant theoretical achievement in this area came in the centuries eighteenth and nineteenth with the development of classical mechanics, i.e. Hamiltonian and Lagrangian formalism, and powerful numerical tools. All those achievements propelled the study of key topics like the many body problem, chaotic phenomena, etc. Allowing a depth understanding of the dynamic of complex gravitational systems, such as planetary systems, star clusters, etc.

Parallel to the previous theoretical advances, on the observational branch was beginning to arise the idea of *island universe*, from which would evolve the concept of galaxy. All of this was powered by the development of the telescope, furthermore allowing understanding that galaxies are just a large collection of stars like our sun. It was also very remarkable the pioneer work of William Herschel, who tried to build a complete map of our galaxy determining distances from the assumption of stars with the same intrinsic luminosity and with the inverse square law for the intensity decay (see Figure 1.1). Although his results were very imprecise due to the incorrect assumption on which were based, the importance of his work lies on the recognition of some structure (disk-like) for our galaxy.

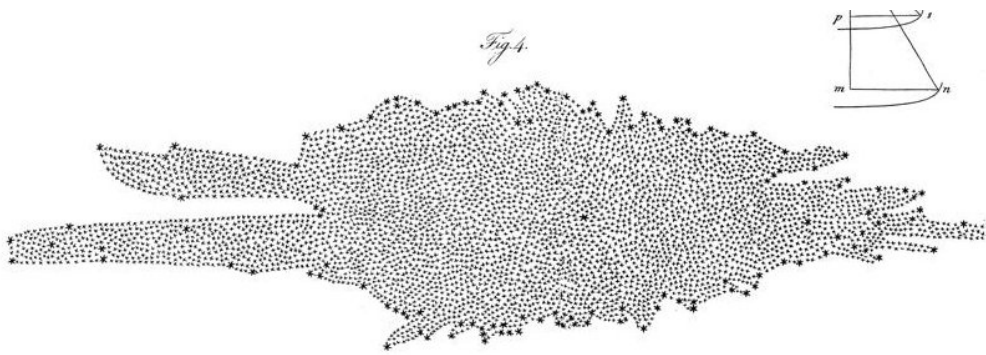


Figure 1.1: William Herschel's model for our galaxy based upon a count of stars with the assumption of equal intrinsic luminosity. [14].

1.1 Prehistory

Another important observational question, that was emerging among scientists by that time, was the existence of *island universes* like ours. It was already well-known the existence of extended objects that do not fit to the definition of stars or planets, like nebulae, planetary disks and galaxies. Even, William Herschel and his son, John Herschel, contributed with the realization of a large (for the epoch) catalogue of extended bodies known as *Catalogue of Nebulae and Clusters of Stars* and a subsequent improved and expanded version finished by John Dreyer in 1888, *New General Catalogue of Nebulae and Clusters of Stars*, which together with *Index Catalogues* of 1895 and 1908 constitute a large collection of bodies widely used in current astronomy, referred with the abbreviations *NGC* and *IC* respectively [26]. Despite of those observational advances, the real nature of these objects was a complete mystery, specially if they lie within our own galaxy or are completely independent systems.

This question remained unsolved until the twentieth century, and together with the indetermination of the real size of the universe, were the two big issues treated on the well-known *Great Debate*, or also called the *Shapley-Curtis Debate*. In this important event in the history of astronomy, the astronomers Harlow Shapley and Herber Curtis discussed about these topics, giving, respectively, different arguments for and against if these objects are within our galaxy and if the Milky Way is our whole universe or not [4] [32]. Despite of that, their arguments were not very conclusive and the definitive solution to these issues had to wait until 1924, when Edwin Hubble measured the distance to Andromeda Galaxy (M31 or NGC 224) and demonstrated unquestionably the real extragalactic nature of this object, and in following years for other ones [18]. This achievement along with the observational verification of the expanding universe (also due to Hubble) were the beginning of the modern observational cosmology.

It also happened in the twentieth century a key event for the modern sciences of gravity, Albert Einstein formulated his theory of General Relativity [6], challenging and changing completely the previous conception of space and time and laying the foundation of current cosmology picture.

1. PRELIMINARIES

1.2 The Current Cosmology Picture

The theoretical basis on which are based the theory of general relativity began to arise with the zenith of non-euclidean geometries in the nineteenth century and the beginning of twentieth, when it was demonstrated that the Euclid's fifth postulate is not needed to build self-consistent geometries, thus giving rise to non-planar geometries (see Figure 1.2). In particular, it was highlighted the work of Nikolai Lobachevsky, father of non-euclidean geometries, and Bernhard Riemann, the founder of the Riemannian geometry.

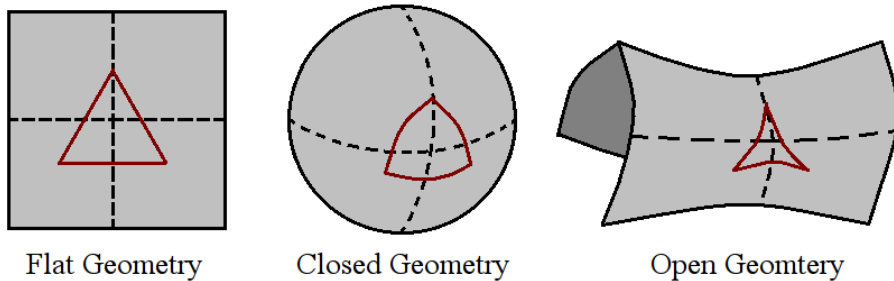


Figure 1.2: Different geometries according to variations on Euclid's fifth postulate.

In spite of these first developments contributed widely to the current cosmological paradigm, bringing forward discussions on what kind of geometry the universe has, the concepts of space and time were completely misunderstood yet, being interpreted as unrelated and absolute entities. That is why the foundation of the theory of general relativity opened the door to our whole current understanding.

Once obtained the equations of metric field of the general relativity, it was possible to build global and self-consistent models of the universe. A first rough attempt was also due to Einstein, who formulated, influenced by his own belief, a static and closed model of the universe. To achieve it, he must use the well-known cosmological constant in order to compensate the expansion/contraction obtained naturally by the theory.

Few years later, Aleksander Friedmann demonstrated on two articles a set of solutions for closed and hyperbolic universes' expanding from a singularity [10] [11].

1.2 The Current Cosmology Picture

These expanding solutions were in agreement with the observations made by Hubble for redshift of far galaxies. Because of that, the inclusion of the cosmological constant for stationary solutions it is historically known and recognized by Einstein himself as the biggest blunder of his life. This theoretical finding prompted a set of studies on the real nature of the universe in the light of those new solutions, like large-scale dynamics, global geometry and precise measurements of different cosmological parameters of those models.

The next important advance came with the formulation of the Big Bang theory by George Gamow. This theory proposes that early stages of the universe had been very dense and hot, starting from a singularity and reaching the current stage, a constantly cooling and expanding universe. All this is in agreement with the Friedmann's solutions. One of the first predictions of this theory was the early nucleosynthesis, which is responsible of the creation of heavy elements like helium and lithium through fusion reactions of primordial hydrogen. Because of the current abundances of helium and lithium cannot be given account by the standard nuclear processes in stars, this was the first of many achievement of the Big Bang theory; furthermore the early nucleosynthesis was later demonstrated by Ralph Alpher and Robert Herman and it has been observationally corroborated very precisely nowadays.

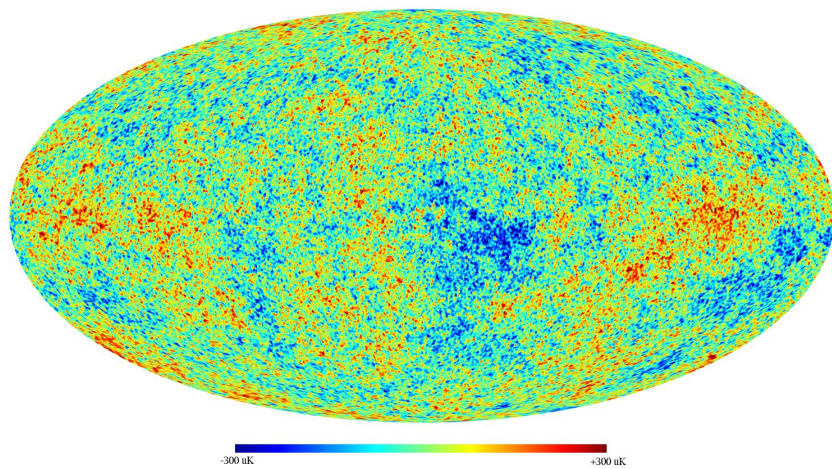


Figure 1.3: Cosmic background radiation. Taken from http://upload.wikimedia.org/wikipedia/commons/3/3c/I1c_9yr_moll4096.png

1. PRELIMINARIES

The next remarkable prediction of the Big Bang theory was the current existence of a residual black-body radiation from early stages, when, due to the conditions of high density and temperature, the universe was radiation-dominated. This remainder was verified observationally by Arno Penzias and Robert Wilson in 1965 with the discovery of the cosmic background radiation (CMBR). The spectrum of this residual radiation proved to be produced by an almost perfect black-body with a characteristic temperature of $T = 2.725$ K. These predictions have made this theory being adopted as a fundamental part of the standard cosmological paradigm.

Although the discovery of the CMBR was certainly one the most important hits of the astronomy along the century twenty, as it has been established in many scientific disciplines, new answers lead to new questions. In this case, the horizon problem. This is originated by the high angular isotropy measured from the CMBR spatial spectrum (see Figure 1.3), which suggests a causal connection between regions of the universe very far apart from each other that, in theory, they should not be correlated. The widely accepted solution to this problem was proposed by Alan Guth in 1980, the inflationary theory. This postulates an exponential expansion of the early universe powered by a scalar field, the inflaton. During the time of expansion, vacuum quantum fluctuations of each field present in the universe was magnified by the expansion itself, producing small perturbations in the density field, from which would evolve current large-scale structures. According to this, the inflationary theory can explain satisfactorily the problem of small perturbations of the very early universe, becoming thus an essential part of the current paradigm.

The existence of dark matter was proposed since early 1930s, initially by Jan Oort in 1932 and then by Fritz Zwicky in 1933, in order to give account of non-luminous matter of galaxies and galaxy clusters, which is manifested through dynamical interactions of their single components, like stars or galaxies in the case of clusters. In spite of that, the real nature of this new type of matter remained as a complete mystery. In 1984 Joel Primack, George Blumenthal, Sandra Moore and Martin Rees proposed a model called cold dark matter (CDM), in which is postulated that dark matter is made of certain unknown type of non-relativistic particle which only interacts gravitationally and electromagnetically (more weakly). Under this scheme, it is possible to demonstrate that large-scale structure formation follows a *top-down* hierarchical process, in which the smallest structures are

1.2 The Current Cosmology Picture

formed first and the biggest, composed by the first, are formed later. This has been observationally verified through galaxy surveys (see section 1.3).

In the 1990s, some cosmological observations suggested an accelerated rate of expansion of the universe, which only can be explained (see subsection 2.1.3) with the inclusion of the cosmological constant in the field equations of the general relativity. Because this constant can be placed as an energy density term with negative pressure, the term of *dark energy* was quickly coined, even though its real nature is completely unknown. Very precise measurements have proved that our universe is currently vacuum-dominated, reaching 70% of all content of matter-energy of it. This last fact completes our overall picture of the current cosmological paradigm and it is called standard Λ CDM model or concordance model.

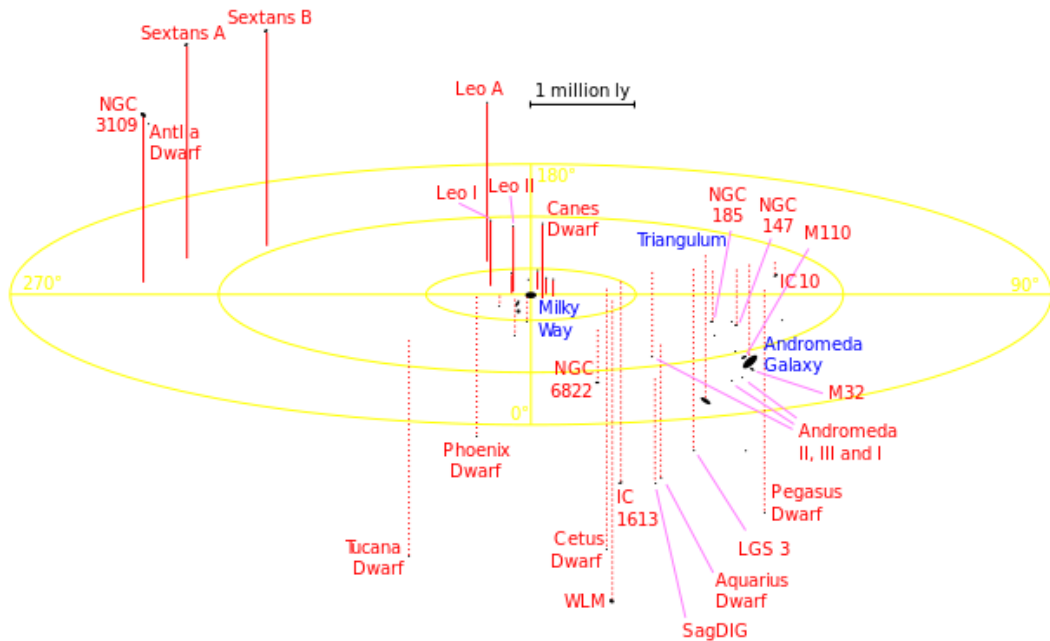


Figure 1.4: Local Group. Taken from http://commons.wikimedia.org/wiki/File:Local_Group.svg

The local group (LG) is a local system composed of 30 galaxies approximately, which interact gravitationally between them and evolve relatively isolated from other large-scale structures. The Milky Way and Andrómeda (M31) galaxies are

1. PRELIMINARIES

its more representative members and even in this work we shall simplify the local group just as systems of two galaxies similar to these (see Figure 1.4).

The importance of our local group in a cosmological context is because it is by far the best known large-scale structure, thereby allowing verifying some current predictions of the concordance model. Among the issues originated by these predictions, we highlight the over abundance of satellite galaxies in the Milky Way, the possible link between the flows of the Magellanic clouds and M31 galaxy, tidal forces in the local group, the kinematic of M31 and Milky Way galaxies in a cosmological context [9] and the influence of the cosmological environment on the formation properties of systems like the local group.

1.3 Cosmological Observations

The boom produced by the space age along with the significant technological development of measuring instruments and sensors have powered enormously observational research in cosmology, thereby allowing, together with the theoretical advances previously discussed, reaching the current cosmological picture. Next, we shall present some of the larger and more important observational projects in cosmology and which are widely used in current research.

2DF Galaxy Redshift Survey

The 2DF Galaxy Redshift Survey (2DFGRS), or Two-Degree-Field Galaxy Redshift Survey¹, is a galaxy redshift survey performed within an angular area of 1500 square degrees of regions near to the north and south galactic poles in order to avoid extinction produced by the galactic disk. This survey was made by the 3.9 m telescope of the Anglo-Australian observatory from 1997 to 2002. Among the main results of this survey are remarkable the mapping of the local structure of the large-scale environment around the local group of galaxies. This was achieved through photometric measurements of 382 323 objects within a redshift range of $z = 0.3$ to $z = 0.0$. It is also remarkable the measuring of the density parameter of non-relativistic matter (dark + baryonic) of the standard cosmological model.

¹Official web page of the project at <http://magnum.anu.edu.au/~TDFgg/>.

Sloan Digital Sky Survey

The Sloan Digital Sky Survey (SDSS), like the 2DFGRS, is a redshift survey of the large-scale universe made by the 2.5 m telescope of the Apache Point observatory in New Mexico since 2000.

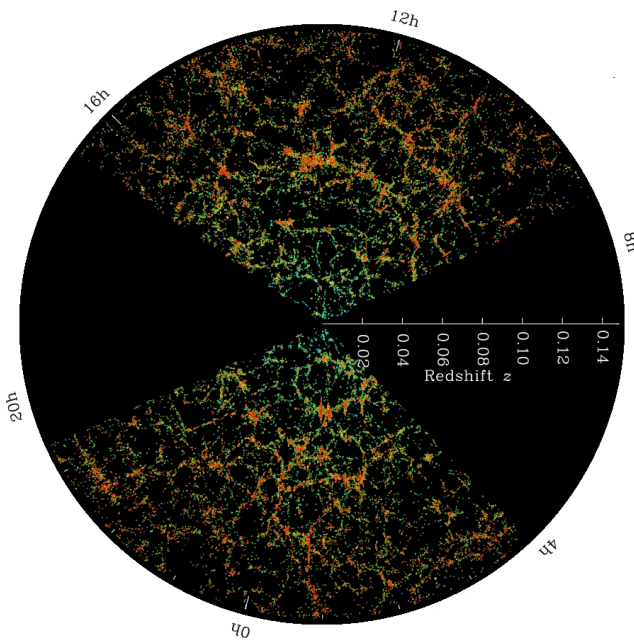


Figure 1.5: Map of the large-scale universe according to the Sloan Digital Sky Survey.

Taken from the official web page of the project <http://www.sdss.org/>

The survey covers an area significantly larger than 2DFGRS, approximately 7500 square degrees, and has catalogued around 2 million of objects, thereby allowing building a map of the large-scale universe in which it was first seen the structure of the cosmic web (see Figure 1.5).

WMAP

The Wilkinson Microwave Anisotropy Probe (WMAP), is a NASA spacecraft launched in 2001 and placed in the lagrange point L2. Its main objective is to measure, with very high precision, small temperature contrasts and polarization of the cosmic background radiation (see Figure 1.3). Approximately every two years, NASA releases the accumulated results obtained, called as WMAP1, WMAP3, WMAP5,

1. PRELIMINARIES

WMAP7 and finally WMAP9 for data released in 2012. These results have been up to date the most reliable proof of the standard cosmological Λ CDM model. Specially it is remarkable the precise measuring of the age of the universe, the cosmological density parameters, the Hubble's constant, also the determination of the global geometry of the universe (flat geometry) and the confirmation of the inflationary model.

| Parameter | Notation | Value | Unit |
|--|------------------|-----------------------|------------|
| Age of universe | t_0 | 13.75 ± 0.13 | Ga |
| Hubble's constant | H_0 | 71.0 ± 2.5 | km/(Mpc s) |
| Hubble's parameter | h | 0.71 ± 0.025 | – |
| Barion density | Ω_b | 0.0449 ± 0.0027 | – |
| Dark matter density | Ω_c | 0.222 ± 0.026 | – |
| Dark energy density | Ω_Λ | 0.734 ± 0.029 | – |
| Radiation density | Ω_r | 8.24×10^{-5} | – |
| Amplitude of Fluctuations at $8h^{-1}$ Mpc | σ_8^2 | 0.801 ± 0.030 | – |
| Spectral index | n_s | 0.963 ± 0.014 | – |
| Reionization optic depth | τ | 0.088 ± 0.015 | – |
| Total density of the Universe | Ω_0 | $1.080 +0.093/-0.071$ | – |

Table 1.1: WMAP7 cosmological parameters [20].

In Table 1.1 is tabulated all the results of the WMAP7 release [20], which are widely used in next chapters and specially in the different cosmological simulations presented below in the chapters 3 and 4.

“The Cosmos is all that is or was or ever will be. Our feeblest contemplations of the Cosmos stir us: there is a tingling in the spine, a catch in the voice, a faint sensation, as if a distant memory, of falling from a height. We know we are approaching the greatest of mysteries”

Carl Sagan

CHAPTER

2

Theoretical Framework in Cosmology

The aim of this chapter is to cover, in a self-contained and summarized way, all the theoretical framework needed for the study of the large-scale universe. From the simplest models of the universe given by Friedman’s solutions, the theory of perturbations for the formation of complex structures like galaxies and galaxy clusters, until the schemes to quantify the cosmic web.

2.1 Isotropic and Homogeneous Universe

The two big pillars of the modern cosmology are the cosmological principle and the theory of the general relativity. The first one is a principle where it is assumed that the universe is isotropic and homogeneous at very large scales, while the second one gives the theoretical support needed in order to understand properly the relation between the matter content of the universe and the structure of the space-time.

As it has been evidenced by observations of large-scale structures and the CMB, the universe appears to be isotropic and homogeneous at large scales, which is in agreement with the cosmological principle. Moreover, this fact simplifies quite

2. THEORETICAL FRAMEWORK IN COSMOLOGY

enough the complex tensorial formulation of the general relativity, thereby allowing finally leading to the Friedmann's equations.

2.1.1 Metric of Curved Spaces

In the construction of an isotropic and homogeneous model of universe, it is necessary to establish an adequate metric which describes it properly. An illustrative example that could be generalized is a 2D spherical surface, which clearly satisfies the criteria of homogeneity and isotropy.

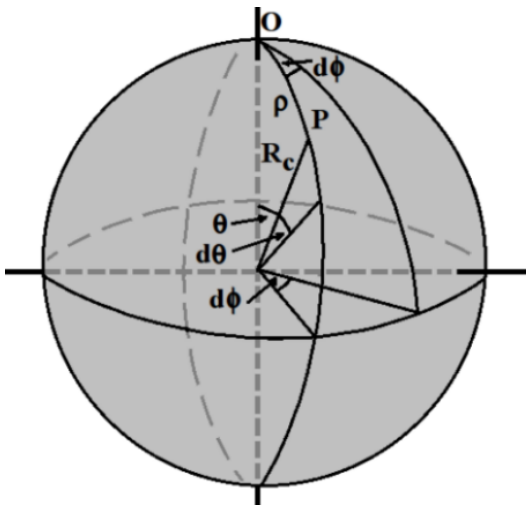


Figure 2.1: Metric of a spherical surface.

A line element over the surface shown in Figure 2.1 can be described as

$$dl^2 = d\rho^2 + R_c^2 \sin^2 \left(\frac{\rho}{R_c} \right) d\phi^2$$

where it have been introduced a new length coordinate over the surface, defined as $\rho = \theta R_c$ and R_c is the curvature radius of the sphere. Another very convenient way to rewrite this expression, and that allowing a very useful generalization, it is reached defining the curvature parameter k and the coordinate $r = \sin(\rho/a)$, obtaining:

$$dl^2 = a^2(t) \left[\frac{dr^2}{1 - kr^2} + r^2 d\phi^2 \right]$$

2.1 Isotropic and Homogeneous Universe

with $k = -1$ and it is assumed a time-dependent curvature radius $R_c = a(t)$. The metric in this case is 3D and is obtained by replacing the differential element of angle $d\phi^2$ by the solid angle differential $d\Omega^2 = d\theta^2 + \sin^2 \theta d\phi^2$.

$$dl^2 = a^2(t) \left[\frac{dr^2}{1 - kr^2} + r^2(d\theta^2 + \sin^2 \theta d\phi^2) \right] \quad (2.1)$$

Finally, time is included, so the space-time interval for the metric of isotropic and homogeneous curved spaces is:

$$ds^2 = c^2 dt^2 - a^2(t) \left[\frac{dr^2}{1 - kr^2} + r^2(d\theta^2 + \sin^2 \theta d\phi^2) \right] \quad (2.2)$$

The direct generalization of this expression consists in varying the different values of the curvature parameter k in order to obtain the metric of flat ($k = 0$), spherical closed ($k = -1$) or opened spaces ($k = 1$), as it is shown in [26] or [27].

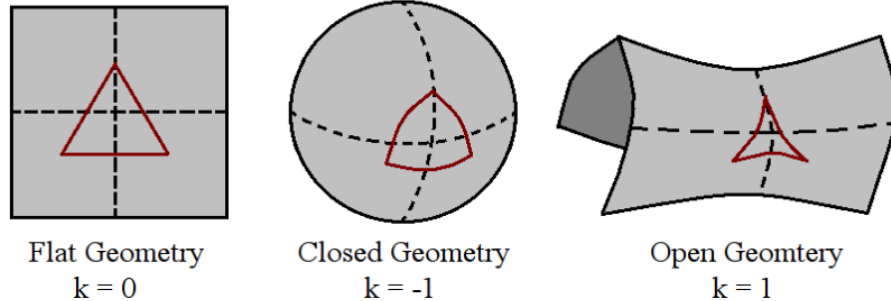


Figure 2.2: Curved spaces according to the curvature parameter.

An alternative way to rewrite the metric is introducing two changes of coordinates defined as

$$\chi = \int \frac{dr'}{\sqrt{1 - kr'^2}}$$

$$\tau = \int \frac{cdt'}{a(t')}$$

where each one is respectively interpreted as a length coordinate over the hyper-surface that defines the space (χ) and as the proper time measured locally (τ). It is obtained the next expressions for the metric

2. THEORETICAL FRAMEWORK IN COSMOLOGY

$$ds^2 = c^2 dt^2 - a^2(t) [d\xi^2 + f_k^2(\xi)(d\theta^2 + \sin^2 \theta d\phi^2)] \quad (2.3)$$

$$ds^2 = \bar{a}^2(\tau) [d\tau^2 - d\xi^2 - f_k^2(\xi)(d\theta^2 + \sin^2 \theta d\phi^2)] \quad (2.4)$$

where the function $f_k(\chi)$ is defined according to the value of the curvature parameter.

$$f_k(\chi) = \begin{cases} \sin \chi & k = 1 \\ \chi & k = 0 \\ \sinh \chi & k = -1 \end{cases} \quad (2.5)$$

In spite of the derived expressions for the metric 2.2 2.3 and 2.4 are completely equivalent, the usage of one or another depends on the specific problem. Specially the expression 2.3 is usually more used and is defined as the Friedmann's metric.

It could be shown that in Riemannian manifolds ¹, the space-time interval is expressed in terms of the metric tensor as [33]

$$ds^2 = g_{\mu\nu} dx^\mu dx_\nu$$

where it has been introduced the cuadrvector $x^\mu = (ct, r, \theta, \phi)$.

Due to the assumption of isotropy and homogeneity, the metric tensor must be diagonal, furthermore, comparing with the expression 2.2, it is possible to obtain the next explicit form

$$g_{\mu\nu} = \begin{pmatrix} 1 & 0 & 0 & 0 \\ 0 & -a^2(t)(1 - kr^2)^{-1} & 0 & 0 \\ 0 & 0 & -a^2(t)r^2 & 0 \\ 0 & 0 & 0 & -a^2(t)r^2 \sin^2 \theta \end{pmatrix} \quad (2.6)$$

From this metric and the Einstein's field equations, it is possible to build simple models of the universe, such as it shall be shown in the subsection 2.1.2.

¹A Riemannian manifold is a space where it can be defined (well-defined) a metric.

Measuring Distances

Once defined the metric of curved spaces, it is very useful to introduce some concepts related with distances, which are used recurrently [26]. For the sake of simplicity it will be assumed a flat metric ($k = 0$).

- **Comoving radial distance:** by definition, a light signal has an associated null interval, i.e. $ds^2 = 0$. Using the expression 2.2 for the metric, it is obtained

$$r = \int_t^{t_0} \frac{cdt'}{a(t')} = \int_a^1 \frac{cda}{a\dot{a}} \quad (2.7)$$

where the specific form of $a(t)$ depends on the specific chosen cosmology (see subsection 2.1.3) and t_0 is the reference time, which is taken as the current age of the universe.

Due to the assumption of an expanding metric, the distance between two objects depends on the time in which the measurement is performed. Moreover, the distance cannot be determined from a beam of light since light has a finite velocity ¹. Because of that, it must be performed a projection on the light-cone traced by the beam in the current time, such as it is made in the expression 2.8. The latter allows interpreting r as the distance to an object in the current time, and it is quite different to the apparent distance which corresponds to the time when the object in question emitted the observed light.

- **Proper radial distance:** by virtue of the definition of scale factor, to obtain the distance to an object in any time, it is enough to multiply the comoving distance by the scale factor evaluated in the same time, that is

$$r_{\text{prop}} = a(t) \int_t^{t_0} \frac{cdt'}{a(t')} = a \int_a^1 \frac{cda}{a\dot{a}} \quad (2.8)$$

- **Particle horizon:** considering a beam travelling through vacuum since the beginning of all time, at $t = 0$; the maxim proper distance that could be travelled by the light in a time t is denominated particle horizon and determines

¹ $c = 299\,792\,458$ m/s

2. THEORETICAL FRAMEWORK IN COSMOLOGY

all regions in the universe that could have been causally connected in that time.

$$r_H = a(t) \int_0^t \frac{cdt'}{a(t')} = a \int_0^a \frac{cda}{a\dot{a}} \quad (2.9)$$

2.1.2 General Relativity and Friedmann's Equations

The Einstein's field equations of the general relativity play a fundamental role since they express explicitly the relation between the matter content of the universe and the local geometry of the space-time.

$$R_{\mu\nu} - \frac{1}{2}Rg_{\mu\nu} - g_{\mu\nu}\Lambda = \frac{8\pi G}{c^4}T_{\mu\nu} \quad (2.10)$$

or equivalently

$$R_{\mu\nu} + g_{\mu\nu}\Lambda = \frac{8\pi G}{c^4} \left(T_{\mu\nu} - \frac{1}{2}Tg_{\mu\nu} \right) \quad (2.11)$$

where T is the trace of the energy-momentum tensor (see 2.14), $R_{\mu\nu}$ the Ricci curvature tensor and R the scalar curvature. The last two terms are calculated from different traces of the Riemann curvature tensor, as $R_{\mu\nu} = R^\eta_{\mu\eta\nu}$ and $R = R^\mu_\mu$. For convenience, it has been introduced the term associated with the cosmological constant, which will be used below to calculate different models of the universe with dark energy contribution.

The Riemann curvature tensor quantifies deviations of the metric of curved space-times with respect to the Euclidean metric and allows to determinate completely the geometrical properties like the local curvature, different measures of distances and angles, etc. [33]. This tensor is built from the Levi-Civita connection as

$$R^\mu_{\nu\alpha\beta} = \Gamma^\mu_{\nu\alpha,\beta} - \Gamma^\mu_{\nu\beta,\alpha} + \Gamma^\mu_{\sigma\alpha}\Gamma^\sigma_{\nu\beta} - \Gamma^\mu_{\sigma\beta}\Gamma^\sigma_{\nu\alpha} \quad (2.12)$$

with the Levi-Civita connection defined from the metric as

$$\Gamma^\nu_{\alpha\beta} = \frac{1}{2}g^{\mu\sigma}(g_{\sigma\alpha,\beta} + g_{\sigma\beta,\alpha} - g_{\alpha\beta,\sigma}) \quad (2.13)$$

2.1 Isotropic and Homogeneous Universe

The right-hand side of the equation 2.10 contains the energy-momentum tensor $T_{\mu\nu}$, which characterizes the density and the matter-energy flux of the universe. By virtue of the cosmological principle, this tensor must also be diagonal and if, furthermore, it is assumed an ideal fluid model, the next form is obtained

$$T_{\nu}^{\mu} = \begin{pmatrix} c\rho^2 & 0 & 0 & 0 \\ 0 & -P & 0 & 0 \\ 0 & 0 & -P & 0 \\ 0 & 0 & 0 & -P \end{pmatrix} \quad (2.14)$$

Finally, using the equations 2.6, 2.11 and 2.14, it is possible to reduce the complex system of tensorial equations to two scalar coupled equations which are usually called Friedmann's equations [26]. These equations describe completely the evolution of an isotropic and homogeneous universe in terms of the scale factor $a(t)$ (see equation 2.1)

$$\frac{\ddot{a}}{a} = -\frac{4\pi G}{3} \left(\rho + \frac{3P}{c^2} \right) + \frac{c^2 \Lambda}{3} \quad (2.15)$$

$$\frac{\ddot{a}}{a} + 2\frac{\dot{a}^2}{a^2} + 2\frac{c^2 k}{a^2} = 4\pi G \left(\rho - \frac{P}{c^2} \right) + c^2 \Lambda \quad (2.16)$$

In order to solve this equation system in terms of $a(t)$ and thereby obtaining the evolution of the scale factor, it is necessary to know the explicit time-dependent expression of the density ρ and the pressure P , or equivalently, the dependence on the scale factor. This must be done for each type of energy-matter of the universe. A detailed derivation of these explicit expressions could be found in [26] and they are summarized in Table 2.1.

By convention, it has been taken the current scale factor as $a_0 = a(t_0) = 1$ and the reference values are defined as $\rho_0 = \rho(a_0)$, $P_0 = P(a_0)$ and $T_0 = T(a_0)$. Using the Friedmann's equations, defining the Hubble parameter as $H(t) = \dot{a}/a$ and the vacuum density as $\rho_\Lambda = c^2 \Lambda / 8\pi G$, it is obtained

$$\left(\frac{\dot{a}}{a} \right)^2 = H^2(t) = \frac{8\pi G}{3} \left[\rho_m \frac{1}{a^3} + \rho_r \frac{1}{a^4} + \rho_\Lambda \right] - \frac{c^2 k}{a^2}$$

Evaluating this expression in the current epoch $H(t_0) = H_0$, with H_0 the Hubble constant and defining the critical density ρ_c as the density that the universe must have in order to be flat.

2. THEORETICAL FRAMEWORK IN COSMOLOGY

| Property | Density | Pressure | Temperature |
|---|---------------------------|---------------------|---------------------|
| Matter (baryonic + dark) | $\rho = \rho_0 a^{-3}(t)$ | $p = p_0 a^{-5}(t)$ | $T = T_0 a^{-2}(t)$ |
| Radiation (+ relativistic matter) | $\rho = \rho_0 a^{-4}(t)$ | $p = p_0 a^{-4}(t)$ | $T = T_0 a^{-1}(t)$ |
| Vacuum | $\rho = \rho_0$ | $p = p_0$ | — |

Table 2.1: Dependence of some quantities on the scale factor $a(t)$ [26].

$$\rho_c = \frac{3H_0^2}{8\pi G} \quad (2.17)$$

it leads to the equation of evolution for the Hubble parameter

$$H^2(t) = H_0^2 \left[(1 - \Omega_0) \frac{1}{a^2} + \Omega_m \frac{1}{a^3} + \Omega_r \frac{1}{a^4} + \Omega_\Lambda \right] \quad (2.18)$$

where it has been introduced the density parameters Ω_i , defined as the current density of the i -th specie in the current epoch, normalized with the critical density 2.17, and $\Omega_0 = \sum_i \Omega_i$. These density parameters along with the Hubble constant are part of the free parameters of the theory and must be determined by observations. This allows to characterize different particular cosmologies ¹

2.1.3 Simple Solutions of the Universe

Although in this stage it has not been introduced the complete formalism of small perturbations and structure formation, the set of equations 2.15, 2.16 and 2.18 leads to a first and rough understanding of the evolution of the Universe.

In this subsection, it will be presented some analytic solutions to the Friedmann's equations. In spite of the ideal assumptions on which are based, in some

¹Cosmology must be understood in this context as a specific solution of the Friedmann's equations.

2.1 Isotropic and Homogeneous Universe

cases, they can be used as approximations in some stages of evolution of the universe, thus allowing a physical understanding more adequate than exact numerical solutions.

Einstein - de Sitter Universe

The Einstein-de Sitter Universe is a cosmological model with a flat metric and composed entirely of matter, this implies that $\Omega_0 = \Omega_m = 1$ and $k = 0$. Applying this in equation 2.18, it is obtained the next expression

$$H^2(t) = \left(\frac{\dot{a}}{a}\right)^2 = H_0^2 \frac{1}{a^3} \quad (2.19)$$

Integrating, it leads to the explicit time-dependent solution for the scale factor

$$t(a) = \frac{2}{3H_0} a^{3/2} \quad (2.20)$$

Although in this case it is possible to obtain the explicit form of $a(t)$, most of the time it is only possible to have the implicit solution $t(a)$. Another very useful way to describe this solution is by using the redshift z , which is related with the scale factor as [26]

$$z + 1 = \frac{a_0}{a} \quad (2.21)$$

to finally obtain

$$t(a) = \frac{2}{3H_0} (1+z)^{-3/2} \quad (2.22)$$

This solution is quite close to the real behaviour of the universe in the matter-dominated epoch, between 70000 and 5 millions of years after the Big Bang [27].

Radiation-Dominated Universe

In this case, it will be assumed that the universe is radiation-dominated, that is $\Omega_0 = \Omega_r$, but not necessarily flat. The Friedmann's equations lead to the next expression

2. THEORETICAL FRAMEWORK IN COSMOLOGY

$$H^2(t) = \left(\frac{\dot{a}}{a}\right)^2 = H_0^2 \left[(1 - \Omega_r) \frac{1}{a^2} + \Omega_r \frac{1}{a^4} \right] \quad (2.23)$$

Integrating this expression, it is obtained the next implicit solution for the scale factor

$$t = \begin{cases} H_0^{-1}(\Omega_r - 1)^{-1} \left(\Omega_r^{1/2} - [a^2(1 - \Omega_r) + \Omega_r]^{1/2} \right) & \Omega_r \neq 1 \\ H_0^{-1}a^2/2 & \Omega_r = 1 \end{cases} \quad (2.24)$$

or in terms of redshift

$$t = \begin{cases} H_0^{-1}(\Omega_r - 1)^{-1} \left(\Omega_r^{1/2} - [(1+z)^{-2}(1 - \Omega_r) + \Omega_r]^{1/2} \right) & \Omega_r \neq 1 \\ H_0^{-1}(1+z)^{-2}/2 & \Omega_r = 1 \end{cases} \quad (2.25)$$

This solution is useful as an approximation for the radiation-dominated epoch, which happened from the big bang until the recombination epoch, approximately 380000 years after the big bang, or equivalently in a redshift of $z = 1100$ [27].

Vacuum-dominated Universe

This type of hypothetical universe is completely vacuum-dominated, or equivalently dominated by the cosmological constant. Making $\Omega_0 = \Omega_\Lambda$ in the Friedmann's equations, it is obtained

$$H^2(t) = \left(\frac{\dot{a}}{a}\right)^2 = H_0^2 \left[(1 - \Omega_\Lambda) \frac{1}{a^2} + \Omega_\Lambda \right] \quad (2.26)$$

Solving for $t(a)$

$$t = \frac{1}{H_0^2 \Omega_\Lambda^{1/2}} \ln \left[a \left(\frac{\Omega_\Lambda}{1 - \Omega_\Lambda} \right)^{1/2} + \left(1 + \frac{\Omega_\Lambda}{1 - \Omega_\Lambda} a^2 \right)^{1/2} \right] \quad (2.27)$$

and using the redshift

$$t = \frac{1}{H_0^2 \Omega_\Lambda^{1/2}} \ln \left[\frac{1}{1+z} \left(\frac{\Omega_\Lambda}{1 - \Omega_\Lambda} \right)^{1/2} + \left(1 + \frac{\Omega_\Lambda}{1 - \Omega_\Lambda} \frac{1}{(1+z)^2} \right)^{1/2} \right] \quad (2.28)$$

2.1 Isotropic and Homogeneous Universe

This solution is very interesting because, unlike the previous solutions, is only valid for values of the density parameter within the range $0 < \Omega_\Lambda < 1$. This implies that it is not possible to have a universe with flat or hyperbolic geometry when it is vacuum-dominated. Another aspect equally remarkable is the concavity of the scale factor $a(t)$ obtained from 2.27 (see Figure 2.3), which shows an accelerated expansion of the universe. This characteristic is only possible when there is a non-null term associated to the vacuum energy.

Finally and like the previous solutions, the expression 2.27 can be used as an approximation for the vacuum-dominated epoch of the universe, which lasts from the end of the matter-dominated epoch, 5 millions of years after the big bang, until nowadays [26].

WMAP7 Universe

The set of parameters associated to the standard cosmological model has been measured on several occasions by different spacecraft missions (see section 1.3). Among those measurements it is notable the one conducted by WMAP. The data obtained after seven years of observation (WMAP7) are adopted in this work [20]. Among the cosmological parameters measured are the Hubble constant and the density parameters Ω_i . Taking the values given in Table 1.1 and for simplicity assuming $\Omega_0 = 1$ it is possible to integrate the Friedmann's equations

$$H^2(t) = H_0^2 \left[\Omega_m \frac{1}{a^3} + \Omega_r \frac{1}{a^4} + \Omega_\Lambda \right] \quad (2.29)$$

to obtain

$$t = \frac{1}{H_0} \int_0^a \left[\Omega_m \frac{1}{a'} + \Omega_r \frac{1}{a'^2} + \Omega_\Lambda a'^2 \right]^{-1/2} da' \quad (2.30)$$

It is possible to obtain an analytic solution of this integral in terms of elliptic functions, but for simplicity it is chosen the numerical solution. In Figure 2.3 is shown the solution for a WMAP7 universe and it is compared to other cosmologies, derived previously.

An interesting characteristic of the solution for the WMAP7 universe is the change of concavity (black curve in Figure 2.3), which indicates a transition from

2. THEORETICAL FRAMEWORK IN COSMOLOGY

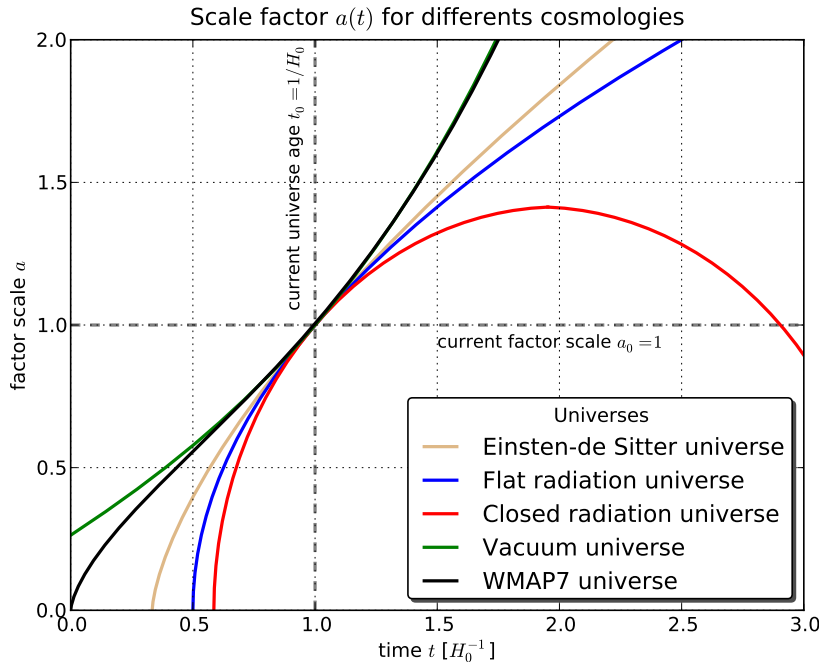


Figure 2.3: Different solutions of the universe according to the Friedmann's equations.

the matter/radiation-dominated epoch to an accelerated expanding regime associated to the vacuum energy. Another important aspect is the prediction of the age of the universe. Taking into account the previously defined normalization for the scale factor $a(t_0) = a_0$, it is straightforward to see that $t_0 = H_0^{-1} \approx 13.75 \times 10^9$ years. Other cosmologies under the same normalization predict different ages, since larger values such as a vacuum-dominated universe, until smaller and even a collapse time (usually known as big crunch time) such as a radiation-dominated and closed universe.

2.2 Linear Regime of Structure Formation

The previous section deals about the universe as a whole, assuming as valid the condition of isotropy and homogeneity. Although the real universe has this asymptotic behaviour at very large scales, at smaller local scales the behaviour is quite different, being even completely anisotropic and highly non-homogeneous. Life is

2.2 Linear Regime of Structure Formation

certainly the most illustrative example of that, one of the highest non-linearities of the universe, and thus, planets, stars, galaxies, galaxy clusters, in the same decreasing order of inhomogeneity and anisotropy.

The standard way to introduce these local structures in the universe is by assuming as valid the solutions of the Friedmann's equations at very large scales, but considering inhomogeneities as perturbations of the model. First, in the linear regime, where the perturbations in the density field are much smaller than the background mean density ($\delta\rho \ll \rho_b$), and after, in the non-linear regime, where the perturbations are comparable or even larger ($\delta\rho \sim \rho_b$) (see section 2.3).

2.2.1 Newtonian Approximation

The frame of linear evolution can be presented in two ways. The first one is by considering a perturbative term in the energy-momentum tensor $\delta T_{\mu\nu}$ and linearizing the Einstein's field equations 2.10 and finally solving for $\delta R_{\mu\nu}$

$$\mathcal{L}(R_{\mu\nu}, \delta R_{\mu\nu}) = \frac{8\pi G}{c^2} (T_{\mu\nu} + \delta T_{\mu\nu}) \quad (2.31)$$

Although this method is, rigorously, more adequate, it has an inconvenience which makes it very complicated of applying. Non-perturbative terms are not necessarily small in all the coordinate systems, inclusively, they can reach values with the same order or even bigger than the background mean density [27].

The second method consists in assuming perturbations with a comoving size smaller than the Hubble radius ($r_\delta \ll r_H \sim cH_0^{-1}$)¹, thereby being possible to neglect relativistic effects due to the curvature of the space-time. Once this is done, it is possible to use a Newtonian scheme to evolve perturbations of the background universe. This scheme assumes that the matter content of the universe is a fluid described by three basic equations of fluid mechanics. The first one is the continuity equation, which expresses mass conservation in a fluid

$$\frac{d\rho}{dt} = -\rho \nabla \cdot \mathbf{u} \quad (2.32)$$

¹The Hubble radius r_H is a length unit that defines the order of magnitude of the size of the observable universe.

2. THEORETICAL FRAMEWORK IN COSMOLOGY

The second one, Euler's equation, characterizes the velocity field of the fluid, and physically it expresses the momentum conservation law

$$\frac{d\mathbf{u}}{dt} = -\frac{\nabla P}{\rho} - \nabla\varphi \quad (2.33)$$

And finally the Poisson's equation, which is the non-relativistic version of the Einstein's field equations and expresses the relation between the matter content of the universe and sources of gravitational field.

$$\nabla^2\varphi = 4\pi G\rho \quad (2.34)$$

In order to complete the Newtonian frame of perturbations is necessary to include in the previous system of equations (2.32, 2.33 and 2.34) the effect of the expansion of the universe by making a change of coordinates of the proper distance \mathbf{x} to comoving distance \mathbf{r}

$$\mathbf{x} = a\mathbf{r}$$

this implies that

$$\mathbf{u} = \frac{d\mathbf{x}}{dt} = \frac{\dot{a}}{a}\mathbf{x} + \mathbf{v} = \dot{a}\mathbf{r} + \mathbf{v}$$

This way to rewrite \mathbf{u} allows separating the contribution of the expansion of the universe ($\dot{a}/a\mathbf{x}$), also called Hubble's law, from the component due to the movement of the fluid, called peculiar velocity field and it is defined as $\mathbf{v} = a\dot{\mathbf{r}}$.

For the sake of simplicity it is decomposed the density field of the fluid into two parts, the background contribution and a perturbative term, that is $\rho = \bar{\rho} + \delta\rho = \bar{\rho}(1 + \delta)$, where δ is called the density parameter and is dimensionless. In the case of the gravitational potential φ , it is defined a new field given by $\Phi = \phi + \ddot{a}ar^2/2$ [26]. With these considerations it is finally obtained the final set of equations for describing a fluid in the Newtonian frame.

| | |
|------------------------|--|
| Continuity equation | $\frac{\partial\delta}{\partial t} = -\frac{1}{a}\nabla_r \cdot [(1 + \delta)\mathbf{v}] \quad (2.35)$ |
|------------------------|--|

2.2 Linear Regime of Structure Formation

$$\begin{array}{ll} \text{Euler's} & \frac{\partial \mathbf{v}}{\partial t} + \frac{\dot{a}}{a} \mathbf{v} + \frac{1}{a} (\mathbf{v} \cdot \nabla_r) \mathbf{v} = -\frac{\nabla_r P}{a \bar{\rho}(1+\delta)} - \frac{1}{a} \nabla_r \Phi \end{array} \quad (2.36)$$

$$\begin{array}{ll} \text{Poisson's} & \nabla_r^2 \Phi = 4\pi G \bar{\rho} a^2 \delta \\ \text{equation} & \end{array} \quad (2.37)$$

Until this stage it has not made explicit what type of matter-energy content is described by the above perturbative fluid equations (e.g. radiation, dark matter, dark energy). Taking into account the followed procedure to derive the previous system of equations, it can be noticed that no *a priori* assumption has been made about the explicit dependence of the state variables on the scale factor (see Table 2.1), therefore they are valid for any of the different species¹ present in the universe. Bearing in mind that the structures of the current universe are completely composed of matter, it will be only used the Newtonian frame for this specie.

The physical quantities that must be determined by the fluid equations together with the Friedmann's equations are: the density parameter δ , the peculiar velocity field \mathbf{v} , the effective potential Φ , the pressure P and finally the scale factor a . It is then so clear that another extra equation is needed in order to get a completely self consistent problem. This is reached by introducing an equation of state for the pressure. For simplicity it is assumed a mono-atomic gas model for the matter, with an associated equation of state given by

$$\nabla_r P = c_s^2 \bar{\rho} \nabla \delta + \frac{2}{3} \bar{T} \rho \nabla s \quad (2.38)$$

where c_s is the velocity of sound in the medium, \bar{T} the background temperature and s the specific entropy. Using this expression along with 2.35 and 2.36, it is obtained the general equation for the evolution of the perturbations

$$\frac{\partial^2 \delta}{\partial t^2} + 2 \frac{\dot{a}}{a} \frac{\partial \delta}{\partial t} = 4\pi G \bar{\rho} \delta + \frac{c_s^2}{2} \nabla^2 \delta + \frac{2}{3} \frac{\bar{T}}{a^2} \nabla^2 s \quad (2.39)$$

In the linear regime, $\delta \ll 1$, the modes of the density field evolve independently from each other, thus allowing decoupling the perturbations at different size scales. A very standard way to solve this type of problems is by using Fourier transform because in the reciprocal space the modes of the field are decoupled naturally.

¹Henceforth, each one of the different matter-energy contents that contributes to the momentum-energy tensor, will be called *specie*.

2. THEORETICAL FRAMEWORK IN COSMOLOGY

Since it has been assumed perturbations with characteristic lengths smaller than the Hubble's radius, the volume of the observable universe can be considered finite, and therefore decomposition of the fields in comoving coordinates becomes discrete, obtaining

$$\begin{aligned}\delta(\mathbf{r}, t) &= \sum_{\mathbf{k}} \delta_{\mathbf{k}} e^{i\mathbf{k} \cdot \mathbf{x}} & \mathbf{v}(\mathbf{r}, t) &= \sum_{\mathbf{k}} \mathbf{v}_{\mathbf{k}} e^{i\mathbf{k} \cdot \mathbf{x}} \\ s(\mathbf{r}, t) &= \sum_{\mathbf{k}} s_{\mathbf{k}} e^{i\mathbf{k} \cdot \mathbf{x}} & \Phi(\mathbf{r}, t) &= \sum_{\mathbf{k}} \Phi_{\mathbf{k}} e^{i\mathbf{k} \cdot \mathbf{x}}\end{aligned}\quad (2.40)$$

If adiabatic perturbations are assumed, that is, perturbations that cannot interchange heat with their environment (the background universe) while they are evolving, the specific entropy must remain homogeneous and therefore $\nabla_r s = 0$ [26]. Considering this and using the previous decompositions of the fields, it is reached the next set of equations for evolving the modes of the density and peculiar velocity fields associated to the perturbations.

$$\frac{d^2 \delta_{\mathbf{k}}}{dt^2} + 2 \frac{\dot{a}}{a} \frac{d\delta_{\mathbf{k}}}{dt} = \left[4\pi G \bar{\rho} - \frac{c_s^2}{a^2} k^2 \right] \delta_{\mathbf{k}} \quad (2.41)$$

$$-k^2 \Phi_{\mathbf{k}} = 4\pi G \bar{\rho} a^2 \delta_{\mathbf{k}} \quad (2.42)$$

$$\mathbf{v}_{\mathbf{k}} = \frac{i a \mathbf{k}}{k^2} \frac{d\delta_{\mathbf{k}}}{dt} \quad (2.43)$$

2.2.2 Jeans Instability

Solutions to the equation 2.41 for the modes of the density field can be classified into two different families. The first one is a set of solutions where the amplitude of each mode oscillates over time and does not collapse. The second family is a set of solutions where each mode grows up over time, collapsing and becoming highly non-linear ($\delta_k \gg 1$). A quite simple example that illustrates the above discussed and can be generalized, involves taking perturbations in a static universe, that is $\dot{a} = 0$. Taking this into account, the equation 2.41 is rewritten as

2.2 Linear Regime of Structure Formation

$$\frac{d^2\delta_k}{dt^2} - \omega_k^2 \delta_k = 0, \quad a = \text{cte} \quad (2.44)$$

where it has been defined the characteristic frequency ω_k as

$$\omega_k^2 = \left[\frac{c_s^2}{a^2} k^2 - 4\pi G \bar{\rho} \right] \quad (2.45)$$

Expression 2.44 is called Jeans equation and it has the form of a wave equation. Based upon this, solutions can be classified according to the value of ω_k , such as it has been said initially.

- If $\omega_k^2 > 0$, the mode δ_k behaves like an oscillator, while it maintains its oscillation amplitude constant over time. This solution is not of interest in the context of structure formation because it is not possible to lead gravitational collapse.
- If $\omega_k^2 < 0$, the amplitude of the mode δ_k grows up over time, thereby allowing gravitational collapse and formation of non-linear structures.

Expression 2.45 for ω_k , along with the previously defined criteria to determine the type of solution, allow to define the Jeans length λ_J

$$\lambda_J = \frac{2\pi a^2}{k_J} = c_s \left(\frac{\pi}{G \bar{\rho}} \right)^{1/2} \quad (2.46)$$

This length can be interpreted as the minimal size in comoving coordinates that must have a perturbation in a homogeneous and static medium with a density value $\bar{\rho}$, in order to collapse gravitationally. In this same context it is possible to define the Jeans mass as the minimal mass value needed for the collapse.

$$M_J = \frac{4}{3} \pi \lambda_J^3 \propto \frac{c_s^3}{G^{3/2} \bar{\rho}^{1/2}} \quad (2.47)$$

In spite of the results previously derived are only strictly valid for static mediums, the importance of considering it lies in two reasons: the first one is the historic interest, just because the problem of perturbations that grow up in homogeneous mediums emerged initially in the context of stellar astronomy, where it is necessary

2. THEORETICAL FRAMEWORK IN COSMOLOGY

to calculate the minimal mass of a perturbation in a gas cloud needed for its collapse and subsequent formation of stars and planetary systems. The second reason is that the solution for static mediums allows evaluating the asymptotic behaviour and the validation of general solutions for expanding mediums.

Before to continue with the solutions for expanding mediums, it is convenient to use the definitions of the Jean mass and length as an approach for the general case. In order to obtain this, Table 2.1 is used to evaluate the dependence on the scale factor of each physical property, furthermore the definition of the velocity of sound in a medium [28]

$$c_s^2 = \left(\frac{\partial P}{\partial \rho} \right)_s \quad (2.48)$$

- In the case of baryonic matter perturbations, it is used the equation of state for an ideal gas assumed of monoatomic hydrogen, and this leads the below expression for the Jeans mass

$$M_J \approx 9.97 \times 10^5 \left(\frac{a_{rc}}{a} \right)^{3/2} M_\odot \quad (2.49)$$

For convenience it has been introduced the scale factor that corresponds to the recombination epoch ¹ a_{rc} .

- For radiation and relativistic matter perturbations, it is used the equation of state for the radiation pressure of the electromagnetic field [19] $P = c^2 \rho / 3$ and the Stefan-Boltzmann law $\rho \propto T^4$. It is obtained the next expression for the Jeans mass

$$M_J \approx 8.39 \times 10^{27} a^3 M_\odot \quad (2.50)$$

Both cases can be used as approximations for different stages of the universe. Before to the epoch of recombination, when matter and radiation were coupled via Compton scattering, perturbations collapse only if they have a mass value close

¹Epoch in which matter and radiation got decoupled, it happened in a redshift of $z_{rc} \approx 1000$, approximately

2.2 Linear Regime of Structure Formation

to the Jean mass 2.50. After of this epoch, when matter evolves independently, expression 2.49 becomes valid.

In Figure 2.4 is illustrated how the Jeans mass changes with the scale factor. It is interesting to notice that before to the epoch of recombination, formation of low-mass structures was impeded due to the homogenization process produced by diffusion of photons in the medium. After of this epoch, when baryonic matter perturbations arises, it is possible to form low-mass structures (like globular clusters), what is in agreement with the theory of hierarchical large-scale structure formation.

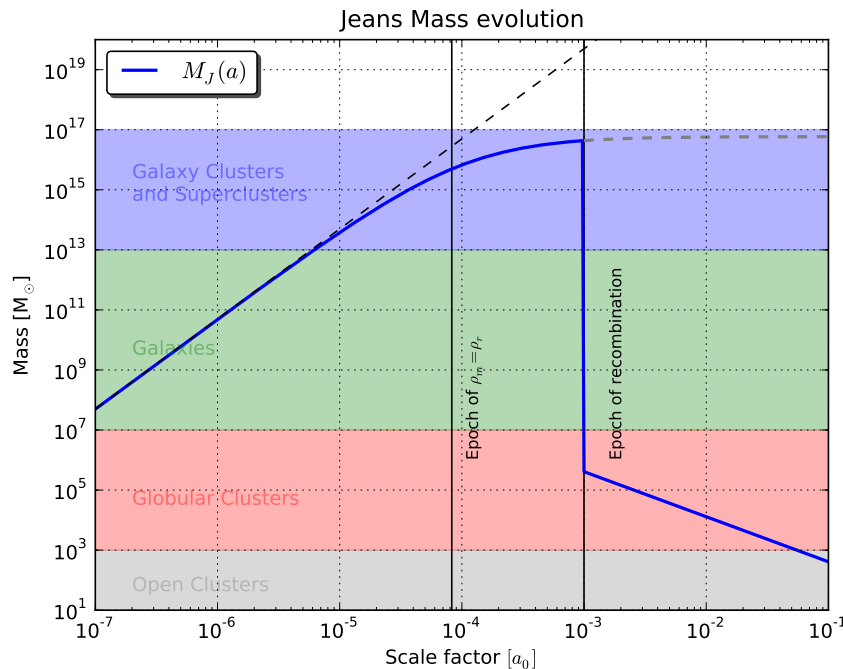


Figure 2.4: Evolution of the Jean mass for different stages of the universe. Coloured regions illustrate the typical mass range of some types of structures, since open stellar clusters to superclusters of galaxies.

The previous analysis has allowed to establish the minimal mass of a perturbation in order to collapse. Next it is studied the evolution of such perturbations in expanding mediums. For this it is used the models of the universe derived in the subsection 2.1.3 and the general equation 2.41 for evolving perturbations.

2. THEORETICAL FRAMEWORK IN COSMOLOGY

- **Einstein - de Sitter universe**

Bearing in mind that for this type of universe $\Omega_m = \Omega_0 = 1$, using the Hubble's function 2.19, the solution for the scale factor 2.20, the velocity of sound derived from 2.48 and the equation of state for an ideal gas, it leads to the below expression for the evolution of the perturbations

$$\delta_k(a) = \delta_{k,0} \left(\frac{a}{a_{\text{ref}}} \right)^1 \quad (2.51)$$

where $\delta_{k,0}$ are the conditions of the field over the reference time t_{ref} . Another possible solution is $\delta_k \propto a^{-3/2}$, but because this solution does not decrease over time, it is not interesting.

- **Radiation-dominated universe**

For perturbations in a radiation-dominated universe with $\Omega_r = \Omega_0 = 1$, using the equation 2.24, it is obtained

$$\delta_k(a) = \delta_{k,0} \left(\frac{a}{a_{\text{ref}}} \right)^{1.22} \quad (2.52)$$

where $\delta_{k,0}$ again represents the initial modes of the field, divergent solutions are ignored.

- **Vacuum-dominated universe**

For a universe with cosmological constant Ω_Λ ¹ it is obtained the next behaviour for the evolution of each mode

$$\delta_k(a) = \delta_{k,0} \left(\frac{a}{a_{\text{ref}}} \right)^{0.58} \quad (2.53)$$

Plotting each one of these solutions, Figure 2.5 is obtained. For simplicity and in order to illustrate in a better way the behaviour of the scale factor, it is normalized each solution with respect to their respective value in the reference time $\delta_{k,0}$.

¹ $\Omega_\Lambda < 1$ in order to guarantee the convergence of solutions to the Friedmann's equation (see subsection 2.1.3).

2.2 Linear Regime of Structure Formation

Initial conditions depend on the comoving wavenumber k and must be determined from the statistical properties of the density field (see subsection 2.2.3) and observational measurements, for instance the cosmic background radiation.

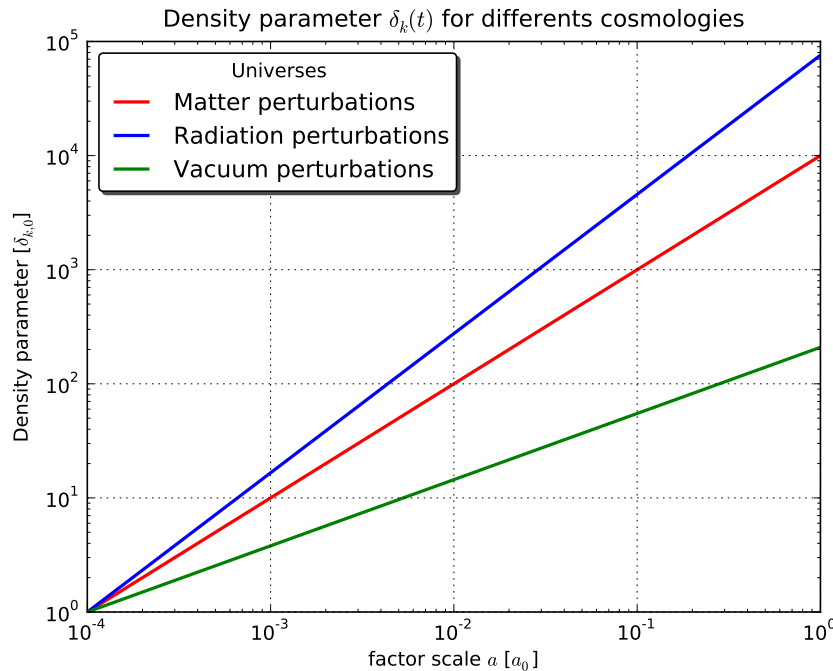


Figure 2.5: Evolution of the normal modes of the density field. For the sake of the illustration, each solution has been normalized with respect to the initial conditions.

2.2.3 Statistical Properties and Transfer Function

Once determined how each mode of the density field evolves, it is necessary to compare this with observations of the real universe. Due to the continuous nature of fields, it is infeasible to try to determine observationally the density distribution. Moreover, taking into account that most of matter is dark, which just can be measured by indirect methods, it is technically impossible, with the current instruments, carrying out this enterprise.

In spite of the above, it is still possible to measure the statistical properties of the density distribution of the universe and to compare them with theoretical predictions. In order to do this, it is introduced the concept of probability functional

2. THEORETICAL FRAMEWORK IN COSMOLOGY

of a continuous field $P[\delta(\mathbf{r}, t)]$, defined as the probability that a certain function has an explicit functional form $\delta(\mathbf{r}, t)$.

A computationally more convenient way to apply the formalism of probability functional is by discretizing the volume in a set of cells $\Delta^3 \mathbf{r}_i$, such that a certain explicit functional form of the density field $\delta(\mathbf{r}, t)$ is equivalent to have simultaneously in each cell \mathbf{r}_i of the grid the value $\delta_i = \delta(\mathbf{r}_i)$, so the probability functional becomes equal to a joint probability function.

$$P[\delta(\mathbf{r}, t)] \longrightarrow \mathcal{P}_{\mathbf{r}}(\delta_1, \delta_2, \dots, \delta_N; t) \quad (2.54)$$

Taking into account the Fourier decomposition of the density field $\delta(\mathbf{r}, t)$ introduced in the equations 2.40, it is possible to define a joint probability function in the reciprocal space $\mathcal{P}_{\mathbf{k}}(\delta_{\mathbf{k}_1}, \delta_{\mathbf{k}_2}, \dots, \delta_{\mathbf{k}_N}; t)$ that completely characterizes the probability of a given distribution $\delta_{\mathbf{k}}(t)$.

The main motivation to work over the reciprocal space is because it is possible to use the approach of uncorrelated modes, where it is assumed that each mode evolves independently of the others. In the real space it is not possible to assume this since the long-range nature of the gravitational interaction couples strongly the density field between different locations. A direct consequence of the previous approach is to express the joint probability function as the product of N single distributions [27]

$$\mathcal{P}_{\mathbf{k}}(\delta_{\mathbf{k}_1}, \delta_{\mathbf{k}_2}, \dots, \delta_{\mathbf{k}_N}; t) = \prod_{\mathbf{k}_i} g_{\mathbf{k}_i}(\delta_{\mathbf{k}_i}; t) \quad (2.55)$$

where

$$\delta_{\mathbf{k}} = \int_V \delta(\mathbf{r}) e^{-i\mathbf{k}\cdot\mathbf{r}} d^3\mathbf{r} \quad (2.56)$$

$g_{\mathbf{k}_i}$ is the single distribution of each mode, $V = L^3$ the normalization volume and $\mathbf{k} = (2\pi/L)\mathbf{n}$, with \mathbf{n} a vector of integer components that characterizes the specific mode.

Assuming that primordial perturbations of the density field were originated by the process of cosmic inflation, it is possible to demonstrate that the distribution of normal modes $g_{\mathbf{k}_i}$ is a Gaussian function [27]. For convenience, it is decomposed

2.2 Linear Regime of Structure Formation

into complex polar coordinates the $\delta_{\mathbf{k}}$ mode of the density field, $\delta_{\mathbf{k}} = r_{\mathbf{k}} \exp(i\phi_{\mathbf{k}})$, which leads to the next distribution

$$g_{\mathbf{k}}(r_{\mathbf{k}}, \phi_{\mathbf{k}}; t) = \frac{2(r_{\mathbf{k}} dr_{\mathbf{k}})}{\sigma_k^2} \left(\frac{d\phi_{\mathbf{k}}}{2\pi} \right) \exp \left(-\frac{r_{\mathbf{k}}^2}{\sigma_k^2} \right); \quad \sigma_k^2 = 2\mu_k^2 \quad (2.57)$$

where μ_k^2 is the variance of the distribution and σ_k^2 is the power spectrum. Due to the assumption of isotropy and homogeneity for the background universe, both quantities only depends on the norm of the wave vector $|\mathbf{k}| = k$. Furthermore it is direct to demonstrate the below properties of the distribution of the field

$$\langle \delta_{\mathbf{k}} \rangle = 0; \quad \langle |\delta_{\mathbf{k}}|^2 \rangle = \sigma_k^2; \quad \langle \delta_{\mathbf{k}} \delta_{\mathbf{p}} \rangle = 0 \quad \text{si } \mathbf{k} \neq \mathbf{p} \quad (2.58)$$

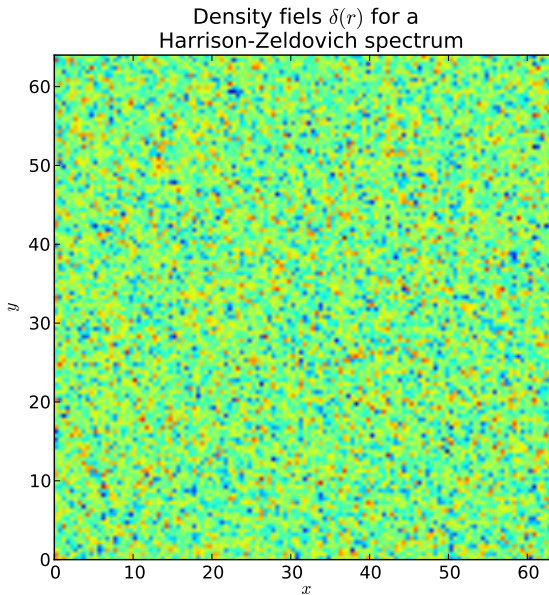


Figure 2.6: Initial distribution of perturbations for the density contrast field from the Gaussian distribution 2.57 and the Harrison-Zeldovich power spectrum $\sigma_k \propto k$.

A quantity that can be directly evaluated is the two-point correlation function $\xi(\mathbf{r}) \equiv \langle \delta(\mathbf{r}' + \mathbf{r}) \delta(\mathbf{r}') \rangle$, defined as the probability of a perturbation at a distance \mathbf{r} from another. It is a direct measurement of the anisotropy degree and the clustering properties of a certain distribution.

2. THEORETICAL FRAMEWORK IN COSMOLOGY

$$\begin{aligned}\xi(\mathbf{r}) = \langle \delta(\mathbf{r}' + \mathbf{r})\delta(\mathbf{r}') \rangle &= \frac{1}{V^2} \sum_{\mathbf{k}, \mathbf{p}} \langle \delta_{\mathbf{k}} \delta_{\mathbf{p}}^* \rangle \exp [i\mathbf{k} \cdot (\mathbf{r}' + \mathbf{r}) - i\mathbf{p} \cdot \mathbf{r}'] \\ &= \int \frac{V^{-1}}{(2\pi)^3} \sigma_k^2 e^{i\mathbf{k} \cdot \mathbf{r}} d^3 \mathbf{k}\end{aligned}\quad (2.59)$$

where in the last line has been performed the continuous approximation. The expression 2.59 shows that σ_k^2 is the Fourier transform of the correlation function, that is

$$V^{-1} \sigma_k^2 = \int \xi(\mathbf{r}) e^{-i\mathbf{k} \cdot \mathbf{r}} d^3 \mathbf{r} \quad (2.60)$$

The previous relation along with the Gaussian distribution of the field show that both, the power spectrum and the correlation function, contain all the statistical information of the density field in the linear regime. If it is assumed a non-Gaussian distribution, it would be necessary to have more moments of the distribution, such as the three-point correlation function, etc.

Harrison-Zeldovich Power Spectrum

A first approximation to the power spectrum of primordial perturbations and that can be demonstrated from the model of cosmic inflation [27] is the next power law expression

$$\sigma_k^2 = A k^{n_s} \quad (2.61)$$

where A is a normalization factor and n is the spectral index. In the specific case where this index is taken to be $n_s = 1$, it is called Harrison-Zeldovich power spectrum and is scale invariant¹.

In order to determine the normalization factor, it is common to apply a filter to the normal modes that contributes to the density field, which leads to the next form of the correlation function

$$\xi(\mathbf{r}; R) = \int \frac{V^{-1}}{(2\pi)^3} \sigma_k^2 e^{i\mathbf{k} \cdot \mathbf{r}} \tilde{W}(k; R) d^3 \mathbf{k} \quad (2.62)$$

¹The observed value is very close to 1, $n_s = 0.963$ (see Table 1.1).

2.2 Linear Regime of Structure Formation

where R determines the maximum scale from which is applied the filter to the modes of the density field and $\tilde{W}(k; R)$ is the Fourier transform of the filter function. Specially, it is defined the dispersion in the real space associated to a scale R as $\sigma_R^2 = \langle \delta^2 \rangle = \xi(0; R)$, this parameter can be determined observationally from galaxy surveys and the cosmic background radiation. The value measured by the WMAP7 release is $\sigma_8^2 = \xi(0; R = 8 \text{ Mpc}/h) = 0.801$ (see Table 1.1), this leads to

$$\sigma_8^2 = A \int \frac{V^{-1}}{(2\pi)^3} k^{n_s} \tilde{W}(k; R = 8 \text{ Mpc}/h) d^3 k \quad (2.63)$$

thus, from the measured values of n_s and σ_8^2 , it is possible to find the correct normalization of the power spectrum.

Transfer Function

Finally for the linear regime, it is introduced the concept of transfer function $T_k(t)$, defined from the below expression

$$\delta_k(t) = T_k(t) \delta_k(t_i) \quad (2.64)$$

where t_i is a reference time, normally taken to be the recombination epoch for matter perturbations.

From the expression 2.64 can be inferred that the transfer function contains all the information about the dynamics of the perturbations, moreover, from the definition 2.58 for the power spectrum it is obtained

$$\sigma_k(t) = \sigma_k(t_i) |T_k(t)|^2 = A k^{n_s} |T_k(t)|^2 \quad (2.65)$$

where it has been assumed a Harrison-Zeldovich power spectrum for the reference time. With this, finally it is concluded that the transfer function also allows to obtain all the statistical properties of the density field during the time when the linear regime is valid.

Calculating the transfer function is generally a complex process and requires numerical computations ¹, furthermore, it depends on the specific properties of the

¹CMBFAST is a widely known software for this purpose http://lambda.gsfc.nasa.gov/toolbox/tb_cmbfast_ov.cfm

2. THEORETICAL FRAMEWORK IN COSMOLOGY

specie that composes the perturbation. For instance, in the case of dark matter perturbations, it must be specified what specific type of particles compose the perturbation, either relativistic lightweight particles (hot dark matter) or non-relativistic heavy particles (cold dark matter). In both cases the transfer function and the processed spectrum 2.65 are quite different due to the equations of state associated to each type.

In the case of adiabatic perturbations (isentropic) of cold dark matter, it can be used the next analytic approximation for the current epoch [26]

$$T_k \approx \frac{\ln(1 + 2.34q)}{2.34q} \left[1 + 3.89q + (1.61q)^2 + (5.46q)^3 + (6.71q)^4 \right]^{-1/4} \quad (2.66)$$

where $q \equiv k/\Omega_0 h^2 \text{ Mpc}^{-1}$.

The next Figure illustrates the transfer function 2.66 along with the processed power spectrum

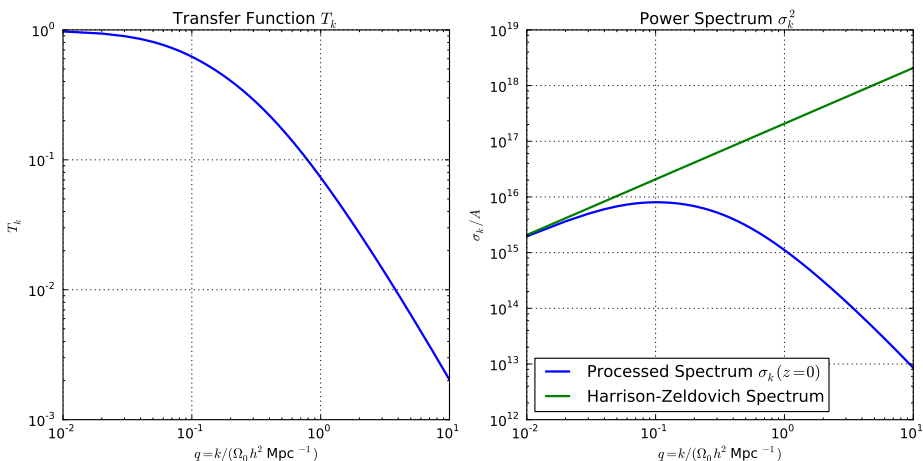


Figure 2.7: Transfer function for cold dark matter perturbations at the current epoch [26] (left panel). Comparison between the initial power spectrum, Harrison-Zeldovich spectrum and the processed power spectrum (right panel).

From all the formalism developed so far in this section, it is concluded that the final objective to characterize the linear regime is to obtain the transfer function, since it determines completely the evolution of the universe at early stages, where there were conditions of high isotropy and homogeneity at all the scales.

2.3 Non-Linear Regime of Structure Formation

In the linear regime, it is described the process of structure formation as perturbations within the isotropic and homogeneous background universe. When perturbations grow up such that $\delta \gtrsim 1$, the self-gravity of the modes couples strongly the local density field and invalidates the linear approximation. The physical processes associated to the non-linear regime are highly complex and even some of them are not currently well understood, this makes possible to tackle satisfactorily this problem only through numerical simulations (see chapter 3).

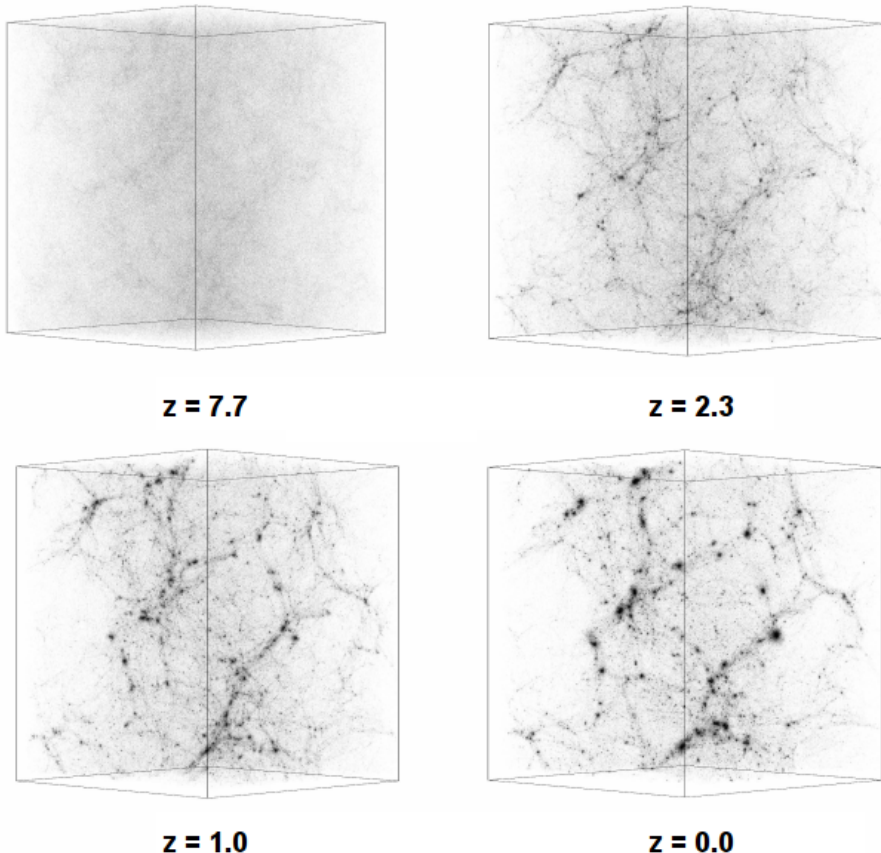


Figure 2.8: Evolution of a dark matter numerical simulation in a comoving volume of $(40 \text{ Mpc}/h)^3$, starting from a high homogeneity stage (upper left panel), until the present epoch with highly non-linear structures (lower right panel). Taken from http://www.astro.utu.fi/research/CosmoS/lss/lss_p1.shtml

2. THEORETICAL FRAMEWORK IN COSMOLOGY

Figure 2.8 corresponds to different stages of a dark matter numerical simulation for the non-linear universe. The Figure illustrates some emergent properties such as the anisotropy and inhomogeneity at small scales (\sim Mpc), formation and clustering of highly non-linear structures and the emergence of a web pattern at large scales (the cosmic web).

2.3.1 Zeldovich Approximation

In spite of the high complexity of the non-linear regime, when the perturbations of the density field are not much bigger than the background value, it is possible to perform an analytic approach to their evolution. This procedure is called the Zeldovich approximation and was developed by Yakov Zeldovich in 1970 [36]. In order to formulate this approximation, it is convenient to express again the contrast density field $\delta(\mathbf{r})$ in terms of comoving coordinates instead of Fourier normal modes. That is because in this regime the Fourier modes are not longer independent from each other and using them does not simplify the problem, unlike the linear regime.

Using the Lagrangian frame of reference of a certain portion of the fluid, its trajectory \mathbf{r}_f can be described through the next expression

$$\mathbf{r}_f(t, \mathbf{q}) = a(t)\mathbf{r} = a(t)[\mathbf{q} + \Psi(\mathbf{q}, t)] \quad (2.67)$$

where \mathbf{r} is the comoving position of the portion of the fluid, \mathbf{q} its initial Lagrangian coordinate when the fluid is not perturbed and $\Psi(\mathbf{q}, t)$ is the displacement function that accounts for the perturbations of the medium.

From the equation for the evolution of the contrast density field 2.39, it is possible to demonstrate that the displacement field $\Psi(\mathbf{q}, t)$ satisfies [34]

$$\frac{\partial^2 \Psi}{\partial t^2} + 2H \frac{\partial \Psi}{\partial t} = \frac{3}{2} H^2 \Psi \quad (2.68)$$

from this, it is finally obtained

$$\Psi = \frac{3}{2} H_0^{-2} a(t) \nabla \Phi \quad (2.69)$$

2.3 Non-Linear Regime of Structure Formation

where Φ is the effective gravitational potential associated to the density field through the Poisson's equation 2.37.

Rewriting the law of conservation of mass in terms of comoving coordinates and the initial Lagrangian coordinates, it must be fulfilled

$$\rho(\mathbf{r}, t) d^3 \mathbf{r} = \bar{\rho}(t) d^3 \mathbf{q} \quad (2.70)$$

now calculating the Jacobian $\partial q_i / \partial r_j$ of the transformation $\mathbf{r} \rightarrow \mathbf{q}$, the perturbed density field can be rewritten as [27]

$$\rho(\mathbf{r}, t) = \frac{\bar{\rho}(t)}{(1 - a(t)\lambda_1(\mathbf{q})) (1 - a(t)\lambda_2(\mathbf{q})) (1 - a(t)\lambda_3(\mathbf{q}))} \quad (2.71)$$

where $-\lambda_i(\mathbf{q})$ are the eigenvalues of the Jacobian and are sorted such that $\lambda_1 \geq \lambda_2 \geq \lambda_3$. Each one of these eigenvalues can be interpreted in a geometric way as an indicator of the collapse or the expansion of a portion of the fluid into the direction corresponding to the respective eigenvector, thus for example if $\lambda_i > 0$, that implies that the density field is collapsing locally into the direction of the eigenvector \mathbf{u}_i , whereas if $\lambda_i < 0$ it implies an expansion into the same direction.

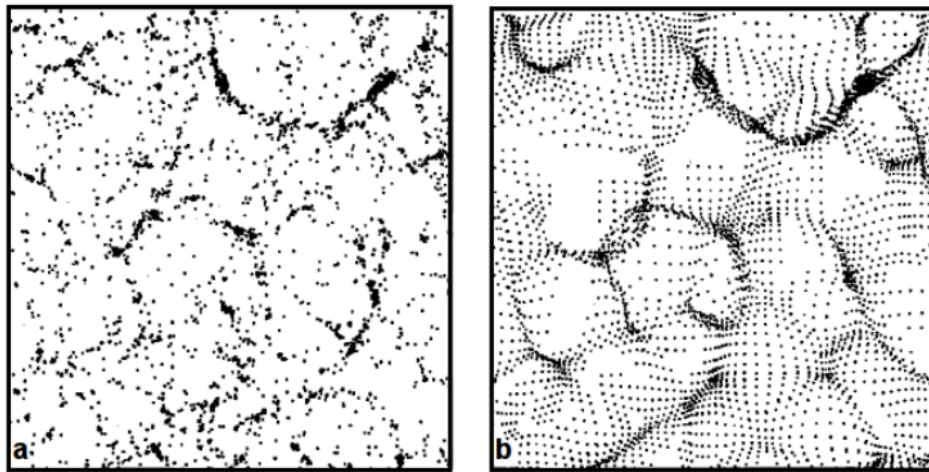


Figure 2.9: Comparison of the evolution in non-linear regime between a N-body simulation (a) and the Zeldovich approximation (b). In both cases are used the same initial conditions. Taken from [26].

2. THEORETICAL FRAMEWORK IN COSMOLOGY

Finally, Figure 2.9 shows a comparison between a numerical N-body simulation and the Zeldovich approximation. It can be seen a high visual similarity of the obtained structures at the end of the evolution, thereby showing the high precision of the Zeldovich scheme. In section 3.3 it will be used the general idea proposed in the Zeldovich approximation regarding the eigenvalues of the Jacobian of the transformation, but for building classification schemes of the cosmological environment based upon the eigenvalues of other physical quantities that are more adequate for describing the local dynamics of the density field, such as the tidal tensor or the tensor of peculiar velocities.

*“All the effects of Nature are only
the mathematical consequences of a
small number of immutable laws”*

Pierre Simon Laplace

CHAPTER

3

Computational Methods in Cosmology

In recent years, computational physics has acquired an important role in physics, allowing modelling many high-complexity systems without the necessity of recurring to experiments and/or observations. Among the methods covered by computational physics is highlighted the N-body problem since many phenomena require the computation of the interactions between a large number of bodies. Some illustrative examples of this are the modelling of molecular systems, plasma physics and specially gravitational problems in astrophysics. The development of specific methods to solve this type of problems precedes the advent of computer systems, even so, their development has powered enormously this discipline such that it is considered a new branch of physics.

In this chapter will be covered in detail some specific methods for solving gravitational problems in astrophysics, specially those related with simulations of the large-scale universe in the non-linear regime, ranging from basic algorithms to compute forces, methods to detect dark halos, to basic classification schemes for the cosmological environment.

3. COMPUTATIONAL METHODS IN COSMOLOGY

3.1 N-body Simulations

Generally, the most suitable type of phenomena that can be modelled through N-body simulations is those where the interactions are strongly correlated between the constituent particles, such as long-range forces or non-local interactions. Figure 3.1 illustrates an arbitrary set of point particles which interact each other under the influence of a force field \mathbf{f} . Those conditions shape the classical formulation of the N-body problem.

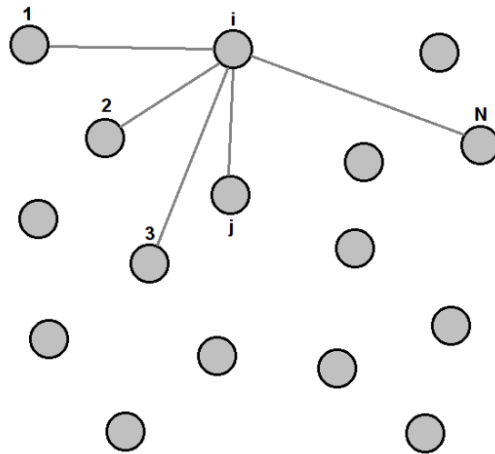


Figure 3.1: Formulation of the N-body problem.

Assuming interactions that depends on the position¹, it is obtained the below equation of movement of the i -th particle shown in the Figure 3.1 [29] [3]

$$\ddot{\mathbf{r}}_i = \sum_{j=1}^N \mathbf{f}(\mathbf{r}_i, \mathbf{r}_j) = -\nabla \phi(\mathbf{r}_i) \quad i = 1, 2, \dots, N \quad (3.1)$$

where it has been introduced the potential function $\Phi(\mathbf{r})$. For the case of gravitational interactions, the potential acquires the form

$$\phi(\mathbf{r}) = - \sum_{j=1}^N \frac{Gm_j}{|\mathbf{r} - \mathbf{r}_j|} \quad (3.2)$$

¹ In the generalized problem, interactions can depend on other parameters like the velocity or intrinsic degrees of freedom like the spin.

The general solution to the problem is obtained from the set $\{\mathbf{r}_1(t), \dots, \mathbf{r}_N(t)\}$, which is determined from the equations 3.1. For this it is necessary to implement numerical approximations due to the non-solvable (analytically) nature of the problem.

3.1.1 P-P Method

The first approximation to find a solution of the equations of movement 3.1 is to compute all the $N - 1$ interactions of the i -th particle with all of the others in a specific time t and this for $i = 1, 2, \dots, N$, then, from a numerical integration scheme it is calculated the positions in a discretized later time $t + \Delta t$ and thus until a given maximum time t_{\max} . This method is called P-P (Particle to Particle) and is one of the three standard methods for solving the N-body problem.

When interactions present singularities, such as Coulombic potentials in electrostatic and gravitational problems (equation 3.2), the integration of the equation of movement is very sensitive to close encounters between particles and therefore the resolution of the time step must be increased, thereby implying a considerable increasing of the computing time. A standard solution is to introduce a softening parameter that removes these singularities, but at the cost of losing accuracy in the solution. For the gravitational potential 3.2, this leads to

$$\phi_s(\mathbf{r}) = - \sum_{j=1}^N \frac{Gm_j}{|\mathbf{r} - \mathbf{r}_j| + \epsilon_j^2} \quad (3.3)$$

where ϵ_j is the softening parameter and can be interpreted as a measure of the physical dimension of the particle.

In spite of the high precision achieved by this method, the computing time scales as $t_{\text{comp}} \propto N^2$, what makes it highly non-viable to apply for a large number of particles (generally $N \gtrsim 10^4 - 10^5$ [27]). For simulations of planetary systems, computation of orbits of minor bodies and studies of star clusters dynamics, this methods is good enough, but for cosmology and galaxy astrophysics, where the number of implicated particles must be the maximum possible in order to reproduce the real continuous nature of the matter distribution, it becomes necessary to develop methods lesser computational cost.

3. COMPUTATIONAL METHODS IN COSMOLOGY

3.1.2 PM Method

A second scheme used for solving the N-body problem is the PM scheme (Particle Mesh) [5], this consists of determining a continuous distribution for the density field from the position and the mass value of each particle, for this it is divided the space of the simulation into a grid of $M \times M \times M$ cells and then a count of particles per cell is made in order to associate a specific mass value and therefore a density to each cell. An illustrative diagram is shown in Figure 3.2

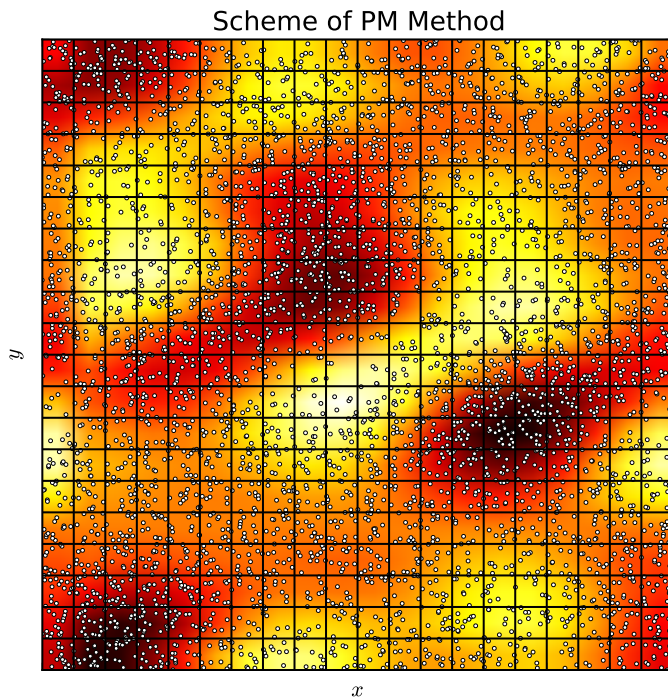


Figure 3.2: Illustrative diagram of the PM method. The map that is plotted over the distribution of particles corresponds to the density field evaluated in each cell of the grid. Dark cells corresponds to overdensity regions whereas white cells to lower values of the density field, which agrees with the amount of mass of the particles per cell.

3.1 N-body Simulations

The method can be summarized into the next steps

1. From the grid established over all the simulation, it is calculated a continuous density field $\rho(\mathbf{r})$, interpolating the value between adjacent cells.
2. Once it is obtained the density field, it is calculated the potential of the equation of movement 3.1 by using the Poisson's equation

$$\nabla^2 \phi = 4\pi G \rho \quad (3.4)$$

In order to reach this, it is usually used integration schemes based upon Fourier transform, such as the Fast Fourier Transform (FFT).

3. Finally, using the previous potential field, it is calculated the position of each particle in the next discrete time $t + \Delta t$, and it is repeated over and over again until a given final time.

This method is less precise than the direct sum, but it is possible to demonstrate that the computing time scales as $t_{\text{comp}} \propto N + M \log M$, with an asymptotic behaviour as $t_{\text{comp}} \propto N$ for high resolutions M of the grid and as $t_{\text{comp}} \propto N$ for low resolutions [29]. In any case, its efficiency is much better than the PP method 3.1.1 when the number of particles of the simulation is large enough $N \ll 10^4 - 10^5$, which makes this method very useful to tackle problems with a large number of particles.

However, there are some pathological situations where this method can not be applied satisfactory [29].

- Highly non-homogeneous distributions of particles.
- Strongly correlated systems.
- Systems with non-trivial geometries.

Because those conditions are satisfied in the non-linear universe, like strong gravitational couplings for modes of the density field after $z \gtrsim 8$, this methods is not very useful for solving the late universe.

3. COMPUTATIONAL METHODS IN COSMOLOGY

3.1.3 P³M Method

The last of the three standard scheme for solving N-body simulations is the P³M method (PP + PM) [15]. This method can be thought as a combination of the previous methods, making the most of each one of them.

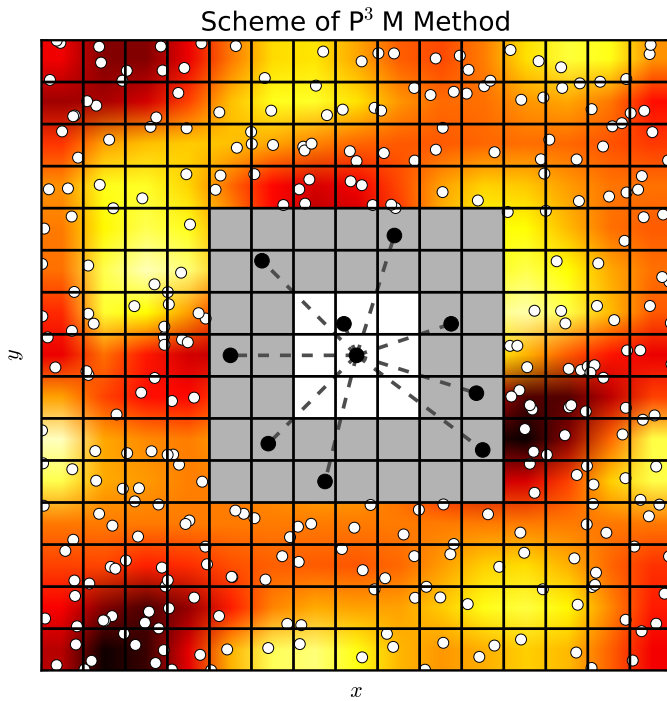


Figure 3.3: Illustrative diagram of the P³M method. For the reference particle, shown in the center, interactions with distant particles is calculated through the PM method, whereas for close particles (gray and white regions), the interaction is calculated by using the PP method.

Figure 3.3 illustrates the P³M method. For each one of the integration step of the system, it is calculated a hierarchical grid for each particle. Hierarchies are defined with respect to the relative distance between particles and they determines which approximation should be used for computing the equation of movement. For close particles (first hierarchy) it is used the PP method, what allows tackling strong local correlations and highly non-homogeneous regions. Interactions with

3.1 N-body Simulations

particles embedded into the next hierarchies are calculated by decomposing the potential field into its multipolar terms, i.e. the second hierarchy corresponds to the dipolar contribution of the potential (if applicable), and so on. Finally for more distant cells (last hierarchy), it is used the PM scheme, interpolating the density field and solving the Poisson's equation 3.4 for the potential.

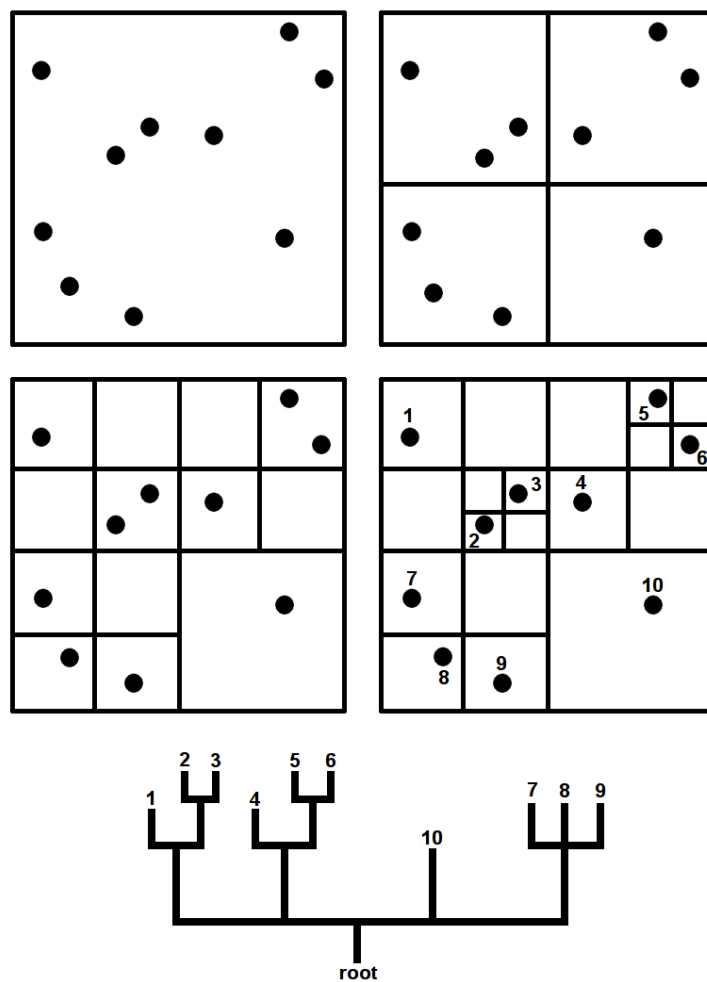


Figure 3.4: An illustrative example of the building of a tree code for a N-body simulation. Upper panels show the iterations for a 2D problem whereas lower panel illustrates the resultant tree built using each particle of the simulation.

3. COMPUTATIONAL METHODS IN COSMOLOGY

One of the main disadvantages of this method lies in the building of the hierarchical structure for evaluating which scheme must be used. The original scheme, proposed simultaneously by [1] [21] and [30], has some inconsistencies produced by the lack of physical basis in the building of the hierarchical structure [29].

A better physically based method for constructing the hierarchical structure of a N-body simulation is the so-called octant tree code. It was initially developed by [2]. In this algorithm, the space of the simulation is embedded into a cubic volume denominated *root*, then this volume is divided into 8 regions of equal size which are denominated octant, these are the first hierarchy of the tree. This procedure is repeated recursively until each cell or octant has only one particle inside, thereby constructing a set of hierarchies that determines the neighbourhood of all the particles of the simulation. Figure 3.4 illustrates the iterations needed in order to construct the tree of a simulation (with the aim of simplicity, it is 2D). The lower panel of the same figure shows the structure of the tree. In this way it is possible to compute, for instance, the interaction between particles 7, 8 and 9 by using direct sum, because they are the closer neighbours each other, whereas the interaction with other particles that belong to other branches is calculated through multipolar expansion or the PM scheme.

3.2 Types of Simulations

Using the methods above described, it is possible to carry out simulations of the late universe in the non-linear regime and studying its behaviour numerically. Because in the non-linear regime all the large-scale astrophysical processes are dominated mainly by dark matter, it is usual not considering the contribution of other components like radiation or baryonic matter, furthermore, including the different physical processes dominated by these other contributions would increase considerably the computing time of the simulation without much profit regarding physical understanding. This specific type of simulations is called *dark matter simulations*.

In this subsection are shown the dark matter simulations that are used throughout this work, moreover they are classified with respect to the adopted criterion for setting the initial conditions, thus, simulations can be unconstrained when the initial conditions are set in a completely random way, or constrained when they are

3.2 Types of Simulations

chosen such that they satisfy some conditions fixed a priori like observational constraints or reproducing the very local structure ($\sim 10 \text{ Mpc}/h$) of the real universe.

3.2.1 Unconstrained Simulations (*Bolshoi*)

Since the evolution of the universe in the linear regime is well-known through the transfer function (see section 2.2), dark matter cosmological simulations are only used for studying the non-linear regime, however it is necessary to establish a set of initial conditions in order to evolve the system properly. Generally these conditions are determined from computing the linear regime, so that it is required another set of primordial conditions for the homogeneous background density field. Because of that, the last set will be henceforth called simply the initial conditions.

As has been mentioned in the subsection 2.2.3, the statistical properties of the initial density field correspond to a Gaussian distribution of the Fourier modes with a Harrison-Zeldovich power spectrum, which agrees with the inflationary model and cosmological observations (see subsection 1.3). The modes of the density field $\delta_{\mathbf{k}} = r_{\mathbf{k}} e^{i\phi_{\mathbf{k}}}$ follow then the distributions given by the equation 2.57

$$P_r(r_{\mathbf{k}})dr_{\mathbf{k}} = \exp\left(-\frac{r_{\mathbf{k}}^2}{\sigma_k^2}\right) \frac{2r_{\mathbf{k}}dr_{\mathbf{k}}}{\sigma_k^2} \quad (3.5)$$

$$P_{\phi}(\phi_{\mathbf{k}})d\phi_{\mathbf{k}} = \left(\frac{1}{2\pi}\right) d\phi_{\mathbf{k}} \quad (3.6)$$

The unconstrained nature of this type of simulations lies in the randomness of the phases $\phi_{\mathbf{k}}$ according to the distribution 3.6, without any kind of observational constraint for the final stage of the simulation.

Bolshoi is a cosmological simulation of the large-scale universe with unconstrained initial conditions, the official website of the project is <http://hipacc.ucsc.edu/Bolshoi/>.

3. COMPUTATIONAL METHODS IN COSMOLOGY

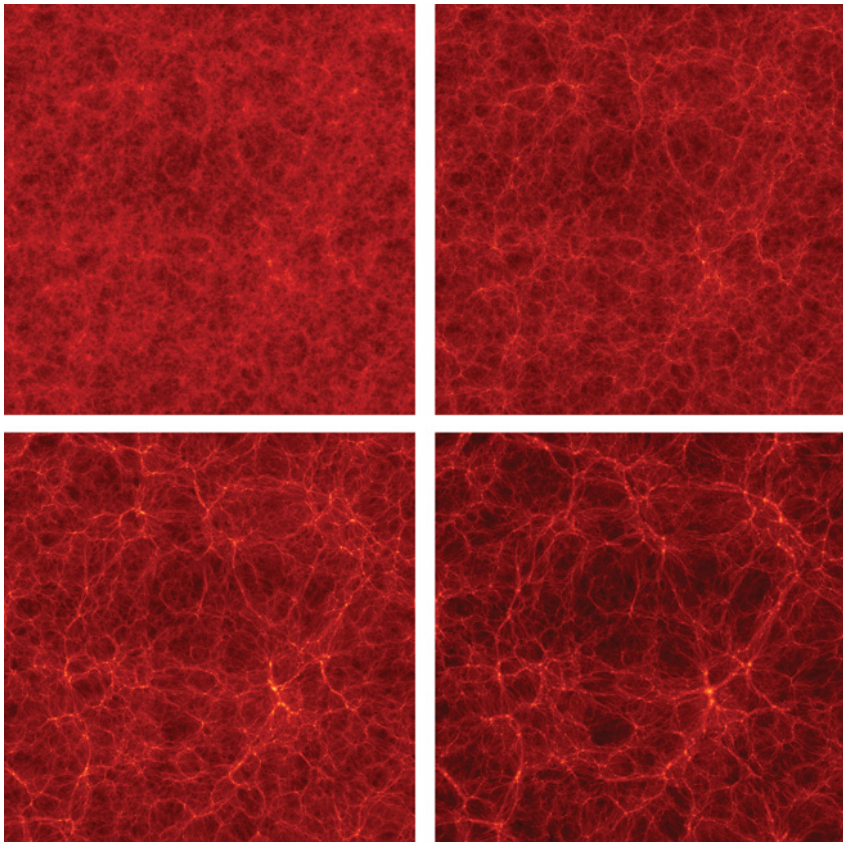


Figure 3.5: Evolution of the Bolshoi simulation. It is illustrated the density field in a rectangular volume of $16 \text{ Mpc}/h$ of thick and $250 \text{ Mpc}/h$ of side for different stages of the evolution. $z = 9.5$ (upper left), $z = 3$ (upper right), $z = 1$ (lower left) y $z = 0$ (lower right). Taken from <http://spectrum.ieee.org/aerospace/astrophysics/the-cosmological-supercomputer>

Due to its larger comoving size compared to constrained simulations (a cubic volume of $250 \text{ Mpc}/h$), Bolshoi is used for obtaining the fine-grained statistics for the results computed in the chapter 4. The cosmological model used in this simulation is the WMAP7 universe (see Table 1.1), the number of particles used is 2048^3 , what implies a mean mass per particle of $1.35 \times 10^8 h^{-1} \text{ M}_\odot$. More precise and technical information about can be consulted in [23].

3.2.2 Constrained Simulations (CLUES)

As has been mentioned in the chapter 2, the standard way to compare the results produced by cosmological simulations and observations is through the statistical properties of the distributions, such as the two-point correlation functions or the power spectrum. In spite of that, some studies require more detailed description of the local universe in a cosmological context. Due to technical issues, like the direct measuring of the dark matter distribution or the lack of data in high redshifts, it is necessary to appeal to cosmological simulations that reproduce properly the local universe. One of the first work aimed to reproduce the local universe is [22]. Here it is reproduced our local group of galaxies along with the local supercluster and the Virgo cluster.

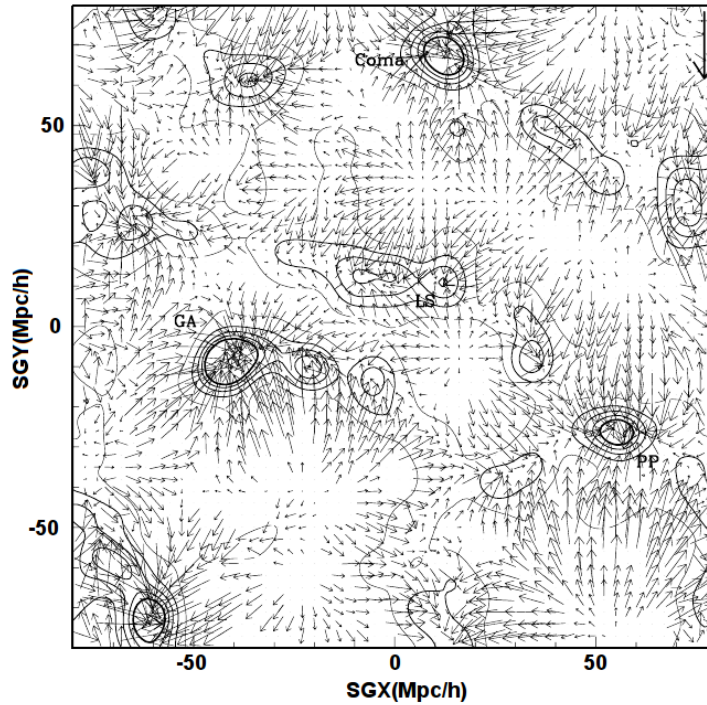


Figure 3.6: Initial density and peculiar velocity field built by using constraints in order to reproduce the local environment at a scale of $160 h^{-1}\text{Mpc}$. Some of the identified structures are: *Coma*, coma cluster, *PP*, Perseus-Pisces supercluster, *LS*, local supercluster, *GA*, the great attractor. The upper arrow indicates the scale of the peculiar velocities field as 1000 km/s. Taken from [22].

3. COMPUTATIONAL METHODS IN COSMOLOGY

The method proposed by [22] and [16] consists in building the initial density and peculiar velocities field from surveys of radial velocities and redshifts (see section 1.3). For the treatment and reduction of noise and measuring errors of data, it is used a Bayesian method, Wiener filters (for more detailed information, see [35]). At small scales, this method is limited because the applied filters suppress some modes in the initial power spectrum and therefore they must be generated randomly according to the Gaussian distribution 2.57 in order to guarantee consistency with the standard cosmological model. Figure 3.6 illustrates the initial conditions obtained by this method for the local universe at a scale of $160 h^{-1}\text{Mpc}$.

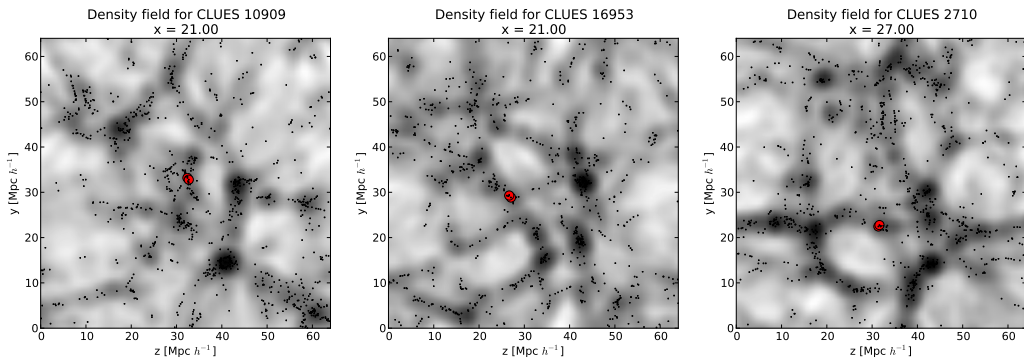


Figure 3.7: Three constrained simulations of the CLUES project where it is possible to identify systems like the local group. It is illustrated the density field of each simulations along with the dark matter halos (black dots), and the LG-like systems found (red points).

CLUES (Constrained Local UniversE Simulations) is a project aimed to reproduce the local universe with the best resolution up to date. The official webpage of the project is <http://www.clues-project.org>. In this simulations, initial conditions are built by using the Hoffman-Ribak algorithm [16] for reproducing a comoving volume of $(64 h^{-1}\text{Mpc})^3$. Due to the unconstrained nature of initial conditions at small scales ($\sim 5 h^{-1}\text{Mpc}$), it becomes necessary to carry out 200 different simulations, of which only 3 are successful regarding the imposed observational constraints (see Figure 3.7). For the evolution it is used the package

3.2 Types of Simulations

GADGET2¹ with 1024^3 particles of dark matter and a cosmology consistent with the WMAP7 (see Table 1.1). More technical details and further information of the project can be found in [12].

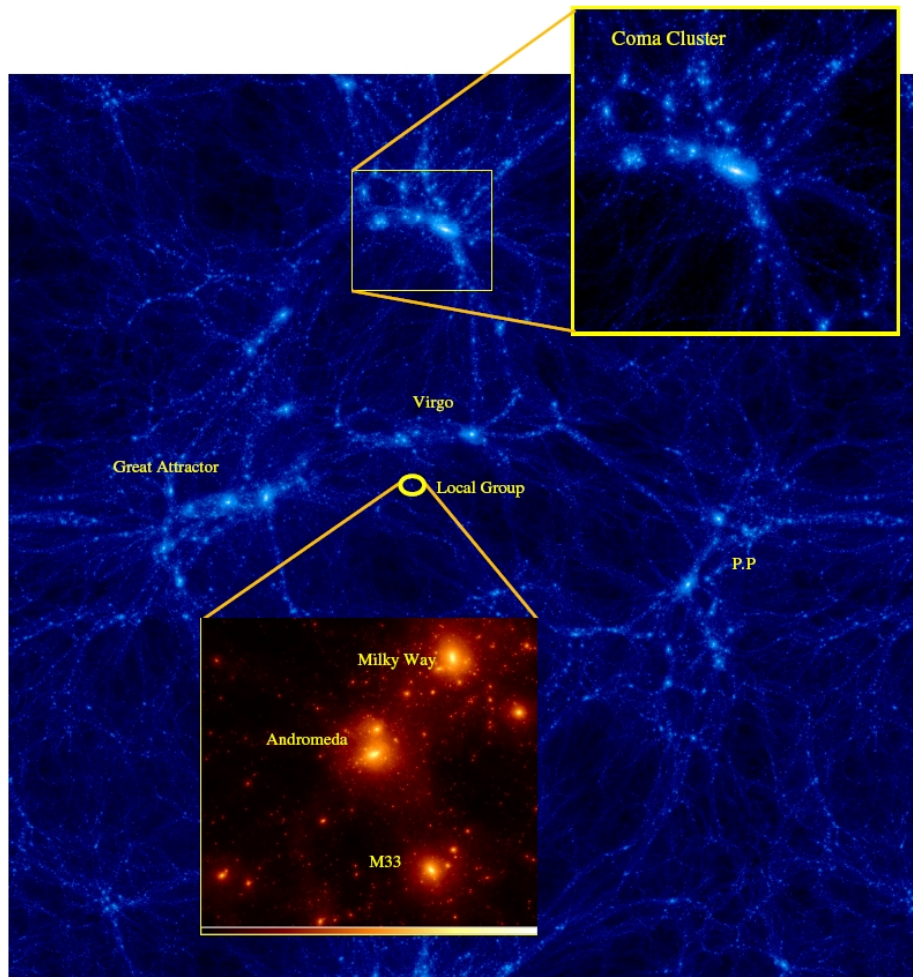


Figure 3.8: An example of a simulation of the CLUES project. In this figure it is shown the large-scale structures of the local universe and it can be appreciated clearly the most significant members of the Local Group. Taken from the official webpage of the project <http://www.clues-project.org>

¹ GADGET2 is a very popular code for N-body simulations developed by Volker Springel. It is available for free download in the official webpage of the project <http://www.mpa-garching.mpg.de/gadget/>

3. COMPUTATIONAL METHODS IN COSMOLOGY

3.3 Environment Characterization

Once obtained the numerical simulations for the evolution of the universe in non-linear regime, one of the main objectives is to characterize the emergent structures typical of this regime. Among these structures, it is highlighted the cosmic web, which is constituted by regions of different dimensionality, where vast void regions are limited by planar regions, these are, in turn, limited by one-dimensional filaments which joint to form high density point regions.

From cosmological observations, it has been possible to establish the relation between the properties of halos, such as the spin parameter, the concentration, the shape, etc. And the host environment. Because of this, it is important to quantify the structure of the cosmic web in cosmological simulations. One of the pioneer works in quantifying the cosmic web was the Zeldovich approximations discussed in subsection 2.3.1), later schemes use stratifications in the density field in order to quantify the environment, these schemes are called geometric methods, but due to their local nature, they cannot give account of global properties like large-scale matter streams or the influence of large neighbouring structures. In this section is shown two recently developed classification schemes.

3.3.1 T-web Scheme

The first of these methods was proposed by [13] and it consists in using the theory of dynamical systems in order to perform an analysis of the local stability of test orbits around dark matter halos, thereby quantifying their environment for a set time (or set redshift). For this, the Newtonian approximation is assumed to be correct (see subsection 2.2.1) and the equation of movement of a test particle embedded into a peculiar potential of the distribution is

$$\ddot{\mathbf{r}} = -\nabla\phi(\mathbf{r}) \quad \text{con} \quad \nabla^2\phi = 4\pi G\bar{\rho}\delta \quad (3.7)$$

It is reasonable to assume that in the center of mass $\bar{\mathbf{r}}_i$ of each halo there is a minimum of the potential, i.e. $\nabla\phi = 0$, thereby forming a local potential well. This allows linearizing the equation of movement 3.7 around these points, obtaining

$$\ddot{r}_i = -T_{ij}(\bar{r}_i)(r_j - \bar{r}_{k,j}) \quad (3.8)$$

where it is defined the tidal tensor as the Hessian matrix of the peculiar potential

$$T_{ij} \equiv \frac{\partial^2 \phi}{\partial r_i \partial r_j} \quad (3.9)$$

According the theory of dynamical systems, a negative eigenvalue indicates an unstable point in the direction of the respective eigenvector, thereby implying an outward flux of matter. For positive eigenvalues, it is presented a completely analogous situation. Base upon the Zeldovich approximation (see subsection 2.3.1), it is proposed a classification scheme for the cosmological environment from the eigenvalues of the tidal tensor T_{ij} (see Figure 3.9).

- **Vacuum:** in this case, the three eigenvalues are positive, thereby indicating an expansion into all directions of space.
- **Sheet:** in this case $\lambda_1 \geq \lambda_2 > 0$ and $\lambda_3 < 0$, thereby implying an one-dimensional collapse, and leading to a region with a planar local geometry.
- **Filament:** for this type of regions, only the value of λ_1 is positive, implying a collapse into two directions and an expansion into the other one, thereby forming a region with a linear geometry.
- **Knot:** finally, for this type of region, the three eigenvalues are negative, so there is a collapse into all the directions, leading a highly compressed zone.

The most remarkable of this scheme compared to geometric methods is its dynamical nature, since it allows differentiating regions with the same density value but with different stability properties. In spite of the latter, assuming a local minimum is only justified in the center of each halo, therefore it is meaningless to generalize this scheme for any other region of the space. Another inconvenient is that, according to the original scheme, using the sign of each eigenvalue instead of using the threshold value, it is not reproduced the visual impression obtained from the dark matter distribution of the simulations (see Figure 3.10).

3. COMPUTATIONAL METHODS IN COSMOLOGY

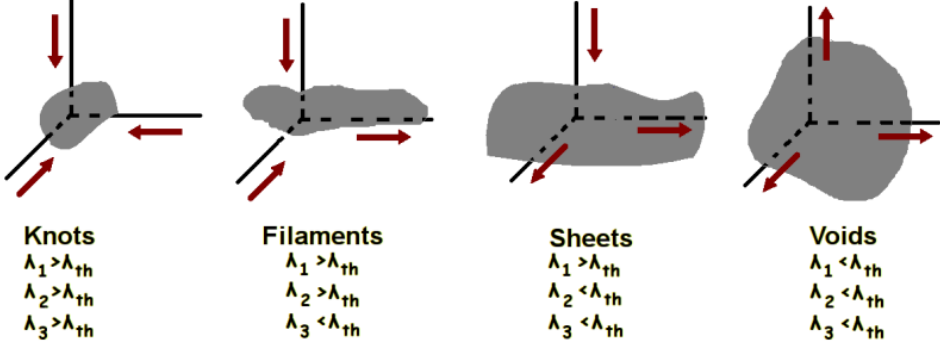


Figure 3.9: Classification scheme for the cosmological environment for both T-web and V-web schemes. The threshold value λ_{th} is taken as free parameter.

A significant improvement of this method is reached by generalizing the classification scheme respect to a certain threshold value λ_{th}^T , which is taken as a free parameter and is adjusted according to the visual impression obtained [7]. Specifically, the original scheme is recovered by setting $\lambda_{th}^T = 0$.

3.3.2 V-web Scheme

The second dynamical scheme to classify the cosmic web presented in this chapter is due to [17] and it is based upon the peculiar shear velocity tensor

$$\Sigma_{ij} = -\frac{1}{2H_0} \left(\frac{\partial v_i}{\partial r_j} + \frac{\partial v_j}{\partial r_i} \right) \quad (3.10)$$

analogously to the T-web scheme, the eigenvalues of the tensor Σ_{ij} are calculated and the environment is defined according to a threshold value λ_{th}^V (see Figure 3.9).

As it has been demonstrated by [17], in the linear regime both tensors T_{ij} and Σ_{ij} are proportional, therefore both schemes are completely equivalent in this time. This fact is partially evidenced through the visual impression obtained for both schemes from the large-scale structure in the Bolshoi simulation (see Figure 3.10), and that is due to the linearity of individual Fourier modes at very large scales.

For small modes, where non-linear effects are more dominant, both schemes differ significantly, as it can be seen in the visual impression of the CLUES simulations. Specifically, the V-web scheme quantifies in a more precise way the fine

3.3 Environment Characterization

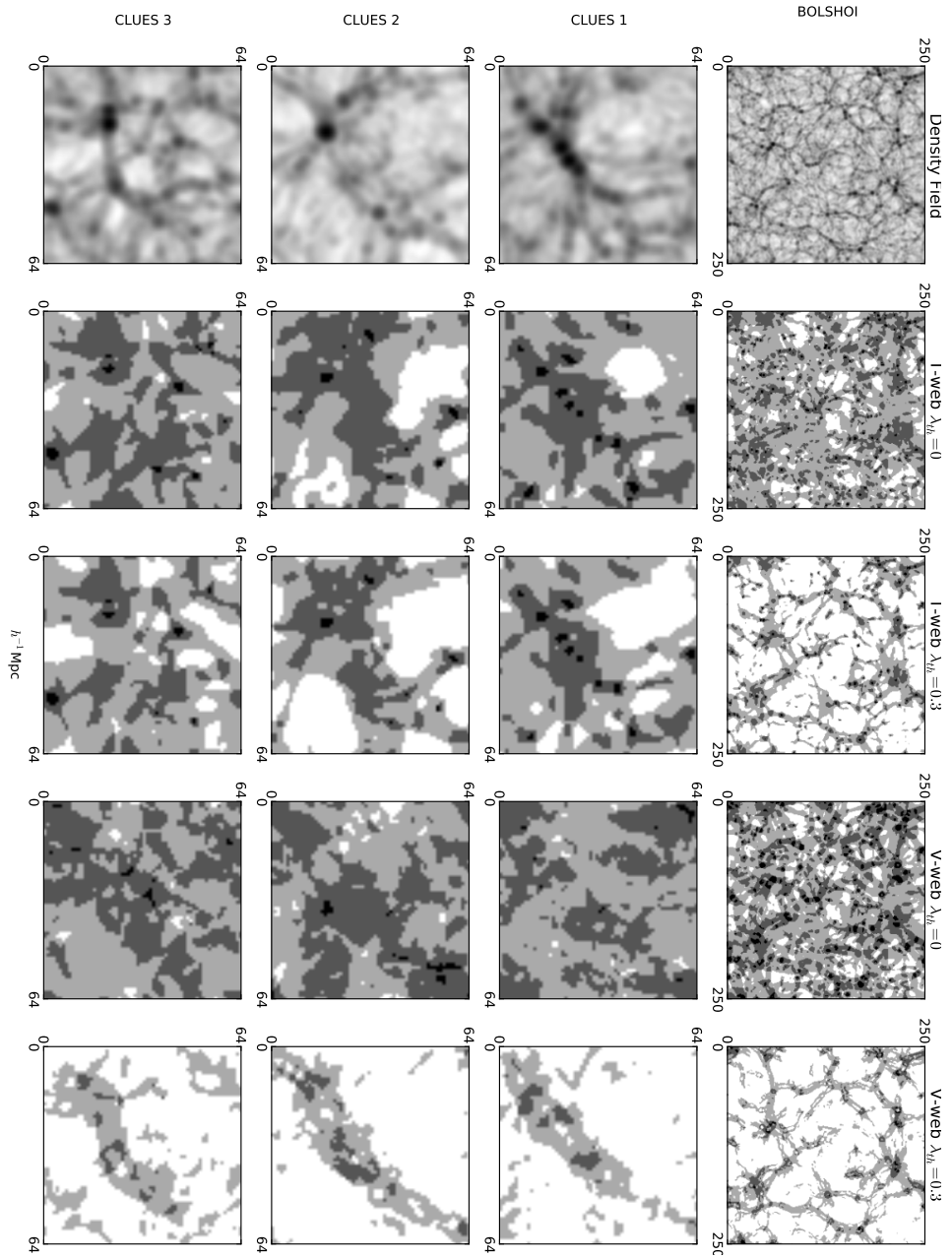


Figure 3.10: It is illustrated for each one of the simulations (CLUES 1, CLUES 2, CLUES 3, Bolshoi) the difference between both classification schemes, T-web and V-web, and for different threshold values λ_{th} (Black - Knot, Dark gray - Filament, Gray - Sheet, White - Vacuum). In the upper figures it is shown the visual impression obtained from the respective density fields ($\log(\delta + 1)$), these impressions are used to calibrate the threshold value λ_{th} . The resolution of the used grid in each simulation is approximately $1.0h^{-1}$ Mpc/cell and for each one it is performed a Gaussian softening of one cell size. The width of each slide is one cell.

3. COMPUTATIONAL METHODS IN COSMOLOGY

structure of the cosmic web at small scales, thereby allowing defining a more appropriate environment for cosmologically small structures like dark matter halos or small groups of them.

Another advantage of the V-web scheme regarding the T-web is because the V-web is based upon the shear velocity field instead of the density field, thereby giving more information about the dynamic of the local environment and making possible to quantify more directly non-local effects, like fluxes of matter or the influence of neighbour structures. Because of this, this scheme will be adopted as standard for quantifying the environment of halos and pairs (Local Group-like systems) and statistical distributions of the cosmic environment in the chapter 4.

3.4 Detecting Halos and Defining the Samples

Once the cosmological environment has been characterized, the next step is to find the structures formed in the simulations, specifically dark matter halos. Due to the continuous nature of the matter distribution of the universe, it is complicated and subjective to define discrete and spatially limited structures, like dark matter halos and the embedded galaxies within them. In spite of this, the rough nature of numerical solutions requires a priori discretization of the density field through point particles with an associated representative mass (generally in the order of $10^7 \sim 10^9 h^{-1} M_\odot$, though this depends specifically on the resolution of the simulation). The latter implies that the selection of discrete physical structures¹ is reduced to find clusters of particles which represents these systems.

3.4.1 FOF Method

One of the most used methods for detecting structures in N-body simulations is the FOF (Friend of Friend method).

¹ In spite of the particles that maps the density distribution have also a discrete nature, their individuality lacks of physical sense and it is only a consequence of the used numerical schemes.

3.4 Detecting Halos and Defining the Samples

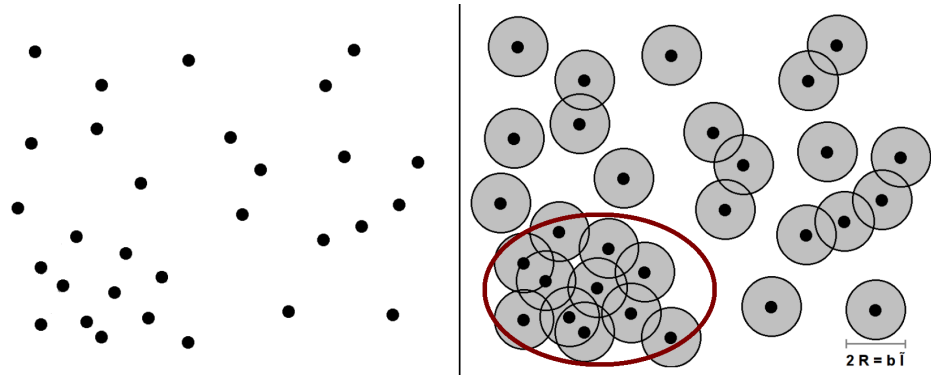


Figure 3.11: Illustrative diagram of the FOF method. Gray circles around each particle represents the linking region and the red curve represents one of the bounded structures found by the method.

In this method, it is associated a finite volume to each particle which is called the linking region. Once defined these volumes, the structures are found by detecting intersections between them. An illustrative example is shown in the Figure 3.11, where the structure enclosed by the red curve, corresponding to a dark matter halo, is made of the 11 adjacent linking regions which intercept each other. The geometry of the linking regions is generally spherical, with a radius R_i given by the next expression

$$R_i = \frac{1}{2}b \bar{l} \quad (3.11)$$

where b is the linking parameter and \bar{l} the mean free path of the particles of the simulation. The linking parameter b is free and depends on each simulation particularly, being given a priori before the construction of the catalogue of halos.

Figure 3.12 shows the result of applying the FOF method to construct a catalogue of halos for the CLUES 3 simulation. The distribution of the halos is in accordance with the density distribution (see Figure 3.10), following the same pattern of filaments and knots that the cosmic web. In the subsection 3.4.2 the defined samples of halos in each simulation are built by using this scheme, with a linking parameter $b = 0.17$.

3. COMPUTATIONAL METHODS IN COSMOLOGY

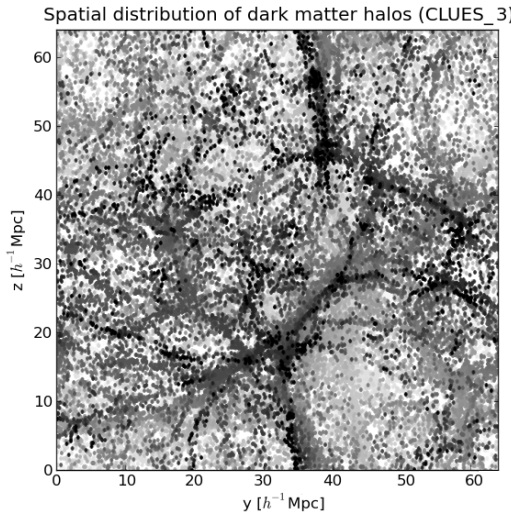


Figure 3.12: Halos detected by using the FOF scheme for one of the CLUES simulations. The color gradient indicates the depth with respect to the x axis, where black dots are the nearest halos.

3.4.2 Defining the Samples

In this subsection, it is presented the samples that will be used in the chapter 4 for determining the effects of the environment on LG-like systems and the characterization of each simulation. These samples are an extended version of the samples defined by [8].

- **General Halos (GH):** these halos correspond to all halos found in the simulations by using the FOF method, independently of the mass range.
- **Individual Halos (IH):** they are a subset of the previous sample and represent all halos that are within the mass range $5.0 \times 10^{11} h^{-1} M_{\odot} - 5.0 \times 10^{12} h^{-1} M_{\odot}$. This mass range is selected because it corresponds to the range in which disc galaxies form, such as the main members of the local group, Andromeda and the Milky Way.
- **Pairs (P):** this sample is built from the IH sample and is composed by all halos that satisfy the criterion to be the closest neighbour to each other. It is

3.4 Detecting Halos and Defining the Samples

constructed as a primitive sample in order to find isolated pairs and LG-like systems.

- **Isolated Pairs (*IP*):** this sample is built from the systems of the Pair sample which furthermore satisfy the next conditions [8] [9].

- The distance between the center of each halo should be less than $0.7h^{-1}$ Mpc, what is consistent with the distance between Andromeda and the Milky Way.
- The relative radial velocity of the pair system should be negative.
- There should be no objects more massive than both halos at a distance less than $2.0h^{-1}$ Mpc with respect to the position of the pair.
- There should be no objects more massive than $5.0 \times 10^{13}h^{-1} M_{\odot}$ at a distance less than $5h^{-1}$ with respect to both halos.

These conditions guarantee the isolation of the pairs with respect to the gravitational influence of larger structures and other halos.

- **LG-like Systems (*LG*):** this sample is defined in the CLUES simulations and corresponds to the halo pairs built a priori for reproducing the local group. By definition, there is only a *LG* system in each one of three simulations.
- **Constructed Local Groups (*CLG*):** with the aim to obtain a *LG*-like sample in unconstrained simulations, it is proposed a novel construction method base upon the cosmological environment of the *LG* sample previously defined in the CLUES simulations (see Figure 3.13). For this it is computed the three eigenvalues fields of the shear velocity tensor onto a grid with a resolution of $1.0h^{-1}$ Mpc/cell and a Gaussian softening of one cell size. In the next Table is tabulated the obtained values for the eigenvalues of the environment for the *LG*-like systems.

Finally, from the extreme values of the eigenvalues previously found, it is defined the *CLG* sample as all the pairs *IP* whose respective eigenvalues are within the set range. In order to guarantee self-consistency, it is constructed a *CLG* sample in the CLUES simulations.

3. COMPUTATIONAL METHODS IN COSMOLOGY

| Description | $\lambda_1 [10^{-1}]$ | $\lambda_2 [10^{-1}]$ | $\lambda_3 [10^{-1}]$ |
|---------------|-----------------------|------------------------|------------------------|
| CLUES 1 H1 | 1.82 | 1.20 | -1.59 |
| CLUES 1 H2 | 1.82 | 1.20 | -1.59 |
| CLUES 2 H1 | 1.78 | 9.54×10^{-1} | -8.85×10^{-1} |
| CLUES 2 H2 | 2.19 | 4.45×10^{-2} | -1.29 |
| CLUES 3 H1 | 3.23 | -6.29×10^{-2} | -1.98 |
| CLUES 3 H2 | 3.49 | 1.21 | -1.29 |
| Maximum value | 1.78 | -6.29×10^{-2} | -1.98 |
| Minimum value | 3.49 | 1.21 | -8.85×10^{-1} |

Table 3.1: Eigenvalues associated to the environmental properties of each Local Group found in the CLUES simulations.

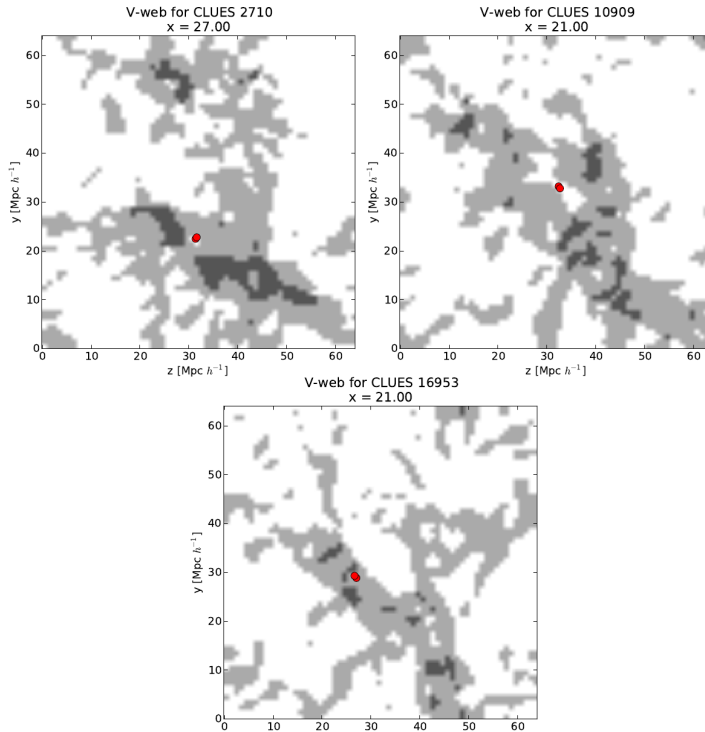


Figure 3.13: Cosmological environment obtained by using the V-web scheme (with $\lambda_{th} = 0.3$) for each one of the LG-like systems in the CLUES simulations (red dots).

3.4 Detecting Halos and Defining the Samples

| Sample | CLUES 1 | CLUES 2 | CLUES 3 | Bolshoi |
|------------|---------|---------|---------|---------|
| <i>GH</i> | 56632 | 57707 | 56799 | 432000 |
| <i>IH</i> | 1493 | 1490 | 1493 | 88068 |
| <i>P</i> | 386 | 380 | 387 | 23037 |
| <i>IP</i> | 20 | 12 | 18 | 1256 |
| <i>LG</i> | 1 | 1 | 1 | – |
| <i>CLG</i> | 1 | 2 | 3 | 30 |

Table 3.2: Size of the defined samples in each one of the simulations.

To finish, in Table 3.2 is tabulated the size of each one of the defined samples in each simulation. It can be noticed that their sizes scale approximately in the same proportion that the volume of the simulations ($1/60 - \text{CLUES} / \text{Bolshoi}$). Specially, the *CLG* sample in Bolshoi has a proportional size that the *LG* in CLUES, thereby indicating that the proposed construction scheme reproduces LG-like systems in unconstrained simulations.

3.4.3 Method to Detect Pairs

Next, it shall be described the algorithm developed for detecting each one of the samples of pair in the simulations (Pair Finder)¹.

- It is partitioned the space of the simulation into $N \times N \times N$ cells, then for each cell it is performed an indexation of the Halos within, storing the identification of each one of them.
- Next, for each cell it is identified the first neighbours, taking into account periodic boundary conditions, such as the cell i in the Figure 3.14.
- For a halo within a given cell, it is calculated the distance to all the other halos within the same cell and the neighbour cells, then it is stored the distance to the closest halo, the distance to the closest halo with a mass greater than the current mass and finally the distance to the closest halo with a mass grater than $5.0 \times 10^{13} h^{-1} M_{\odot}$.

¹ An updated version of this code can be found in the next github repository https://github.com/sbustamante/Thesis/tree/master/codes/Halo_Finder

3. COMPUTATIONAL METHODS IN COSMOLOGY

- Repeating the previous step for all the halos, if two halos are the closest to each other, they are catalogued as a pair system, constructing in that way the P sample defined in the previous subsection 3.4.2.
- Finally, for each one of the pair systems it is evaluated the defining conditions for the IP systems, thereby determining this sample.

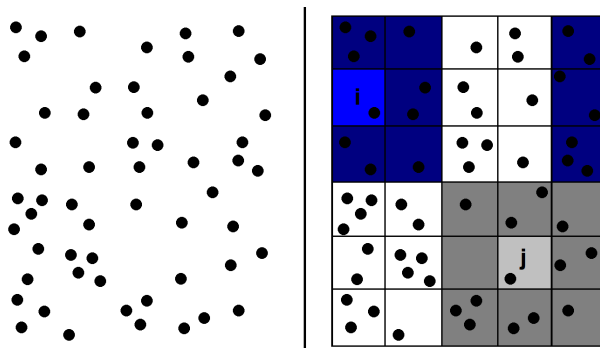


Figure 3.14: Two-dimensional of the method for detecting the pair samples. Random distribution of a set of dark matter halos (left), definition of cells (right).

The efficiency of this method lies in avoiding evaluating distances between all the halos of the simulations, being only necessary just for the closest neighbours. The structure of the grid makes this scheme similar to a tree code (see subsection 3.1.3), excepting the hierarchical structure performed in the latter. At first, this code should be more efficient as it is increased the resolution N of the grid, but there are two limitations to this. First, the number of halos per cell should not be very large, but neither that there are just a few halos per cell¹ The second limitation is related with the conditions of distance used for defining the IP sample, the physical size of each cell cannot be less than any of these distances.

¹This threshold is not well-defined and depends on each simulation particularly, for instance for the used simulation (Bolshoi and CLUES), a value of $N = 8$ is generally enough.

*“The most incomprehensible thing
about the universe is that it is com-
prehensible”*

Albert Einstein

CHAPTER

4

The Cosmological Environment and the Local Group

In this chapter, it is presented the results obtained from the simulations described in the previous chapter 3 for the dependence of the properties of LG-like systems on the cosmological environment in which they are embedded. It is firstly characterized each one of the used simulations (CLUES and Bolshoi) with the aim to guarantee consistency between the used cosmologies and between the distribution of the environmental properties (see section 4.1). After this, in the section 4.2 it is determined the physical and statistical properties of each one of the defined samples in 3.4.2 and it is analysed the correlations between the computed properties and the cosmological environment of each simulation.

4.1 Properties of the Simulations

One of the first steps for determining the influence of the environment on LG-like systems is to construct a *CLG* sample in unconstrained simulations and thereby obtaining a more robust statistics. In order to guarantee the consistency of this

4. THE COSMOLOGICAL ENVIRONMENT AND THE LOCAL GROUP

sample is necessary to establish the equivalence between the distributions of dark matter halos and analyse the distributions of the cosmological environment of each simulation.

4.1.1 Halo Mass Function

The spatial distribution of the halos exhibits the fine structure of the cosmic web, which it is constituted by dark matter. This is exhibited both in simulations (see Figure 4.1) and in cosmological observations (see section 1.3). This suggests possible correlations between the properties of the halos and the environment in which they are embedded, such as it has been demonstrated for dark matter halo shapes, the spin parameter and the alignment of satellite halos in [25], and for the halo mass [24]. Specially, in the work of [25] it is demonstrated that the V-web classification scheme is more appropriated for studying correlations with respect to directional properties, like the angular momentum of *IP* or *CLG* systems in the section 4.2.

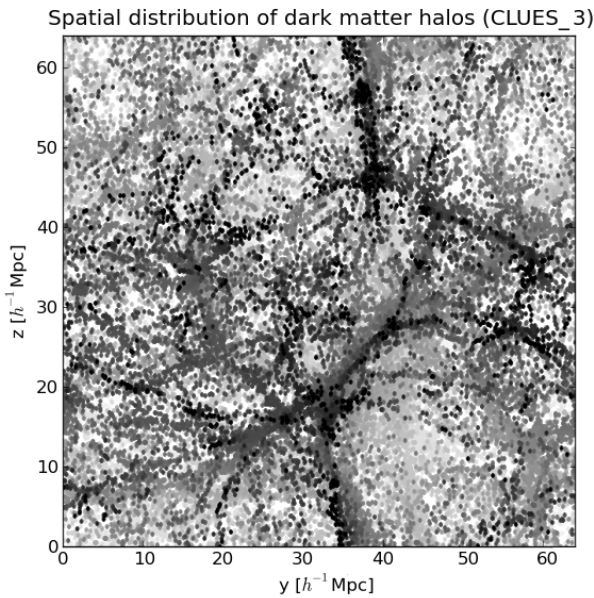


Figure 4.1: Spatial distribution of dark matter halos, exhibiting the characteristic structure of the cosmic web. The colour gradient indicates the depth with respect to the x axis, where black dots are the nearest halos.

4.1 Properties of the Simulations

According to the defining conditions of the *IP* and *CLG* samples presented in the subsection 3.4.2, the main property of the halos that is necessary for constructing these samples is the halo mass. Therefore it is important to establish the equivalence between the mass distribution of each simulation. The next Figure 4.2 shows the results of calculating the cumulative mass functions for the Bolshoi simulation and for the three CLUES simulations.

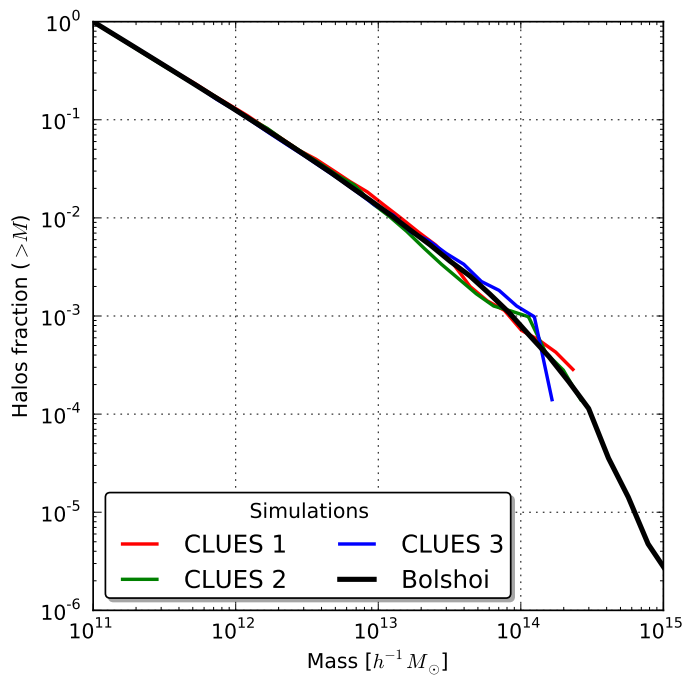


Figure 4.2: Cumulative mass functions of the dark matter halos (*GH* sample) for each simulation.

For high mass values, the distributions are slightly different due to the smaller number of halos in the CLUES simulations, what makes the statistics less significant in this case. In spite of this, within the mass range where the *IP* samples are defined ($5.0 \times 10^{11} h^{-1} M_\odot - 5.0 \times 10^{12} h^{-1} M_\odot$), the distributions are consistent with the Press-Schechter mass function formalism [31] using the cosmological parameters of WMAP7, thereby indicating the equivalence between the defined samples for all the used simulations.

4. THE COSMOLOGICAL ENVIRONMENT AND THE LOCAL GROUP

4.1.2 Distributions of the Cosmological Environment

As it has been shown in the section 3.3, the characterization of the cosmological environment is reached by using physical quantities that indicate the geometric or the dynamical local nature of a certain region in the spatial matter distribution. Specially, the V-web scheme allows to give account of the dynamics at smaller scales of the cosmic web, thereby allowing to characterize and define an adequate host environment for halos and other cosmological structures. The next Figure shows the results of calculating the distributions for each one of the eigenvalues of the shear velocity tensor (distributions of environment), for both, the cells of the simulations, and the host cells of the halos of the *GH* sample.

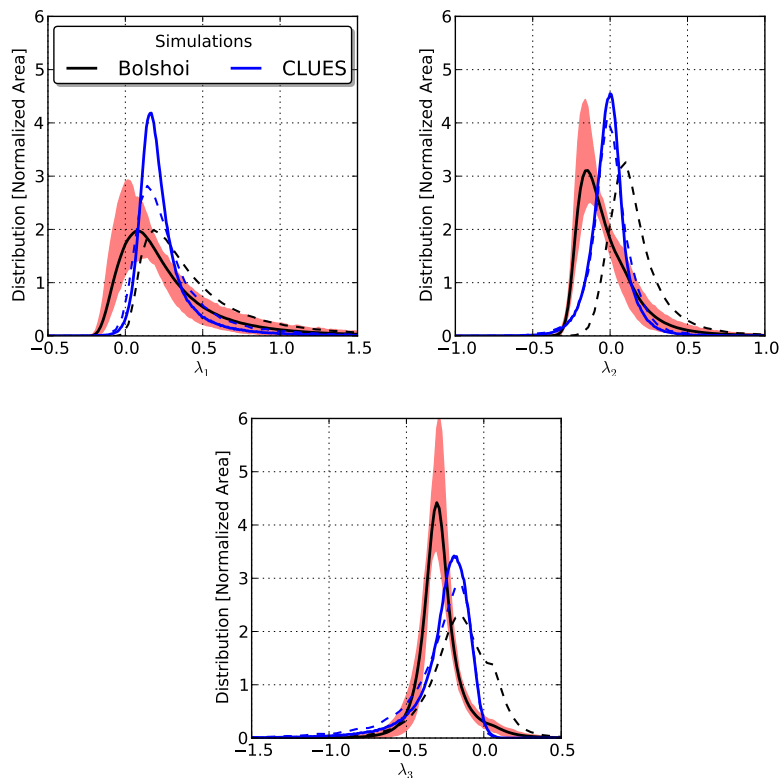


Figure 4.3: Distributions of eigenvalues of the V-web scheme calculated over all the volume cells (continuous lines) and over the host cells of the dark matter halos defined in the FOF catalogue (dashed lines). All the distributions are normalized such that their area is the unity. Resolution of $1.0h^{-1}$ Mpc/cell and softening parameter of one cell size.

4.1 Properties of the Simulations

The main result of the Figure 4.3 consists in the difference of the distributions for all the volume cells (continuous lines) between the Bolshoi simulation and the CLUES simulations¹. The effect of the cosmic variance (red regions) is included from the calculation of the distributions of environment over 64 sub-volumes of the Bolshoi simulation, with a similar size than the CLUES simulations. In spite of this, the distributions of environment of the CLUES simulations are outside the region of cosmic variance, thereby indicating a different cosmological large-scale structure between both simulations.

A second important result shown by the Figure 4.3 it is obtained from the distributions of environment for halos (continuous lines). In the case of Bolshoi, it is noticed an important bias between the distribution of environment associated to the volume cells and the host cells of the halos, thereby indicating that the spatial distribution of the halos is not a good tracer of the large-scale structure of the matter field. This result is consistent with the work of [25], where it has been found an important bias in the distributions of environment according to different mass ranges of the halos, also using the Bolshoi simulation. In the case of the CLUES simulations, the distributions of environment of the halos are significantly less biased regarding the volume cells, thus indicating for this case that halos do distribute spatially according to the cosmological environment quantified by using the V-web scheme.

Finally, in the Figure 4.4 it is shown the calculated mean densities and the volume fractions for each type of region (see section 3.3) according to the threshold value λ_{th} . The volume fraction functions are different between the CLUES and Bolshoi simulations, specially for values close to $\lambda_{th} = 0.1$, corresponding to sheet regions. This is due to the relative displacement of the peaks of the distributions of environment for each simulation (see Figure 4.3), what implies a different behaviour before the criterion to classify the type of region from the λ_{th} value. In spite of this, the volume fractions are more or less consistent for both simulations within the range $0.2 \leq \lambda_{th} \leq 0.4$ that corresponds to the range where the visual impression of the overall density field is better reproduced.

¹ Because of the high similitude between the distributions of the three CLUES simulations, and with the aim of obtaining a more significant statistics, they have been merged.

4. THE COSMOLOGICAL ENVIRONMENT AND THE LOCAL GROUP

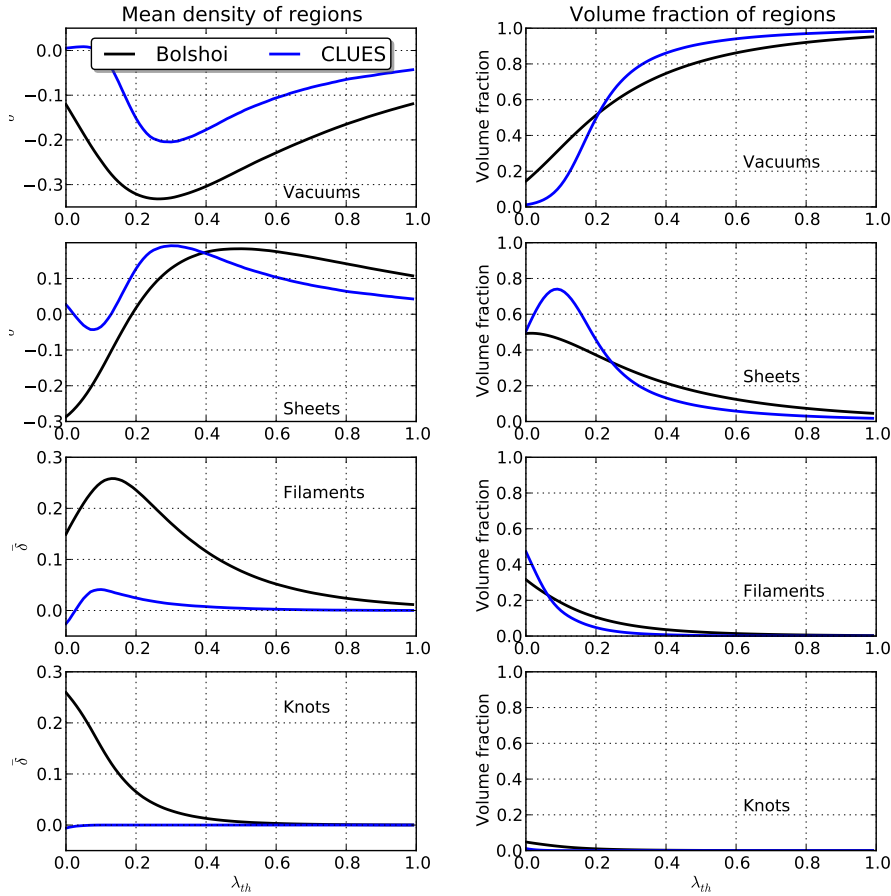


Figure 4.4: Mean density parameter for different type of regions in terms of the threshold value λ_{th} (left panels). Volume fractions normalized for different type of regions, also according to the threshold value λ_{th} (right panels).

In the figures of the mean density for each type of region, it is shown important results regarding the cosmological environment. The first thing that can be noticed is the difference between the mean densities of both simulations for each type of region. For instance for vacuum regions, in Bolshoi these correspond to regions with a mean density much less than the mean density of the entire simulation, whereas in the CLUES simulations, the sub-density of vacuum regions is not very pronounced. Due to the small fraction of knot regions in both simulations (because their zero-dimensional geometry), the global structure of the cosmic web can be understood just in terms of the spatial distribution of vacuums, sheets and filaments,

4.1 Properties of the Simulations

being filaments the counterpart of vacuums regarding the density parameter. From this it is expected that the difference of the sub-density values of vacuum regions between both simulations becomes compensated with a pronounced difference of the over-density values of filament regions between both simulations too. The latter has been obtained in the same figure, where it can be seen that filament regions of the Bolshoi simulation are notably denser than filaments in CLUES. In the case of sheet regions, these correspond to regions with intermediate values of density, within a range between filaments and vacuums, therefore it is expected that the difference of the mean density of these regions between both simulation is not very pronounced, such as it can be noticed in the same figure.

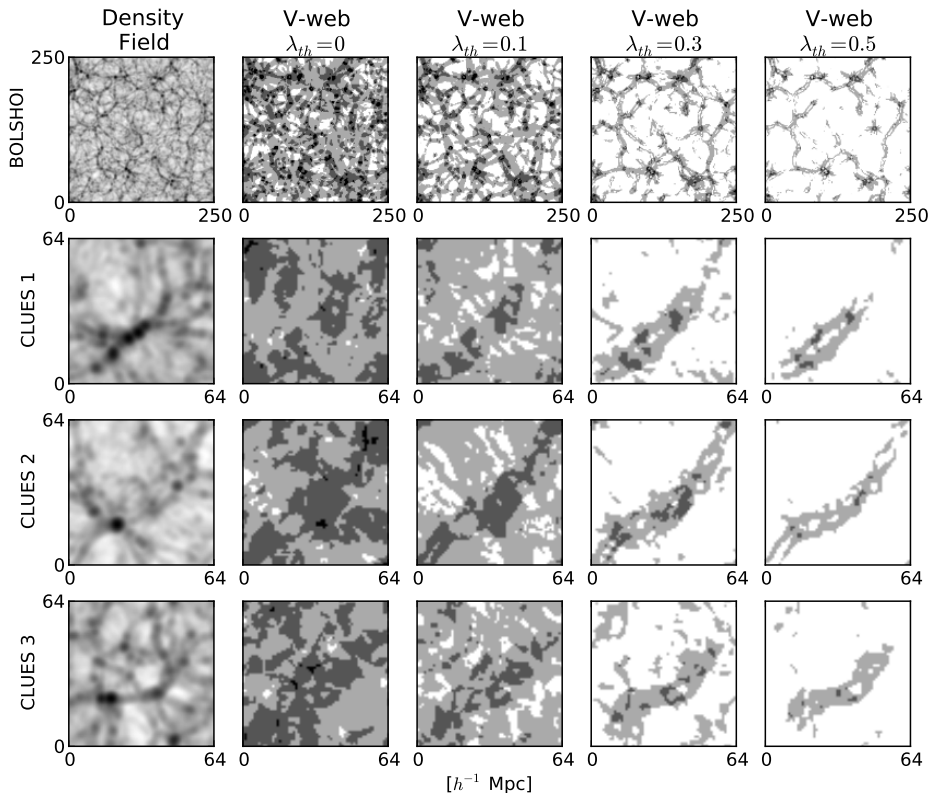


Figure 4.5: Comparison between the visual impression obtained by the V-web scheme for several values of the threshold parameter λ_{th} . It is used the next classification scheme (Black - Knot, Dark gray - Filament, Gray - Sheet, White - Vacuum). The resolution of each grid is $1.0 h^{-1} \text{ Mpc}/\text{cell}$ with a Gaussian softening of one cell size. The width of each slide is one cell.

4. THE COSMOLOGICAL ENVIRONMENT AND THE LOCAL GROUP

The second result shown in the Figure 4.4 consists in determining an optimal threshold parameter λ_{th} for reproducing the visual impression of the cosmic web. As it is shown in this figure, the volume fractions associated to vacuums and sheets are relatively high regarding the values of filaments and knots, and this for all the swept range of threshold values λ_{th} . From this it is expected that the visual impression of the large-scale matter field is completely dominated by the spatial distribution of vacuums and slightly less by filaments and sheets. In the case of a low value of the λ_{th} parameter, e.g. $\lambda_{th} < 0.2$, the mean density parameter of sheet regions becomes negative, thereby indicating that possibly these regions are invading zones that should be catalogued as vacuums, such as it can be noticed in the Figure 4.5 for $\lambda_{th} = 0$ o $\lambda_{th} = 0.1$. In the case of high values, e.g. $\lambda_{th} > 0.4 \sim 0.5$, the mean density parameter for vacuums is increasing, thus indicating that these regions are invading high density zones, which at first should be sheets or filaments. This can be noticed in the Figure 4.5 for $\lambda_{th} = 0.5$, where all the volume is widely dominated by vacuums, thereby loosing the characteristic structure of the cosmic web. This analysis suggests that the optimal value of λ_{th} may be that where the mean density of vacuum regions is minimized, since this type of region is the most dominant. A result that supports this hypothesis is that the found value of λ_{th} for both simulations is quite similar $\lambda_{th} \approx 0.3$, and coincides with the value obtained qualitatively by fitting at first glance the visual impression of the cosmological environment.

To conclude this section, it is discussed the results obtained for the distributions of environment. In spite of there is a significant bias between the spatial distribution of dark matter halos and the distribution of the matter field in the Bolshoi simulation, contrary case in the CLUES simulations, and there is a marked difference between the mean densities associated to each type of region for both simulations, the objective of constructing a *CLG* sample in the Bolshoi simulation from the *LG* systems found in CLUES, as it was mentioned in the chapter 3, it is to obtain a more faithful sample of isolated pairs that also reproduces the same local environment of those *LG* systems. Then, it is expected that the local dynamic, quantifying by the V-web scheme, is independent of the difference between the distributions mentioned above, retaining the validity of the proposed construction scheme for the *CLG* sample.

4.2 Properties of the *CLG* Sample

Once it has been determined the consistency between the defined samples for both simulations, the next step is to determine their properties. It is of special interest to analyse the *CLG* sample in Bolshoi, taking as the control sample the *IP* sample, and as the reference sample the *LG* sample in CLUES.

4.2.1 Determining the Environment

As it has been defined in the subsection 3.4.2 of the last chapter, the *CLG* sample in the Bolshoi simulation is constructed by imposing on the *IP* sample the extra condition of reproducing the cosmological environment of the *LG*-like systems found into the CLUES simulations. The main aim of doing this, it is to find a sample in the Bolshoi simulation analogous to the *LG* sample, regarding their physical properties as well as their abundance. With respect to the latter, it is natural to assume, considering the consistency between the simulation already determined, that the abundance of a certain sample should scale approximately as the volume of the simulation. This fact can be considered as the first success of the proposed construction scheme, since it is reproduced approximately this scale law for the *CLG* sample in Bolshoi and the *LG* samples in CLUES (see Table 3.2).

In spite of the latter, this construction scheme just consists of a cut in the *IP* sample with respect to the eigenvalues of the shear velocity tensor of the V-web, evaluated over the host cells of the pair systems, which does not imply an adequate reproduction of neither the physical properties nor the local cosmological environment of *LG*-like systems. For this reason, below it will be analysed possible bias in the distributions of environment for the host cells of the *CLG* systems.

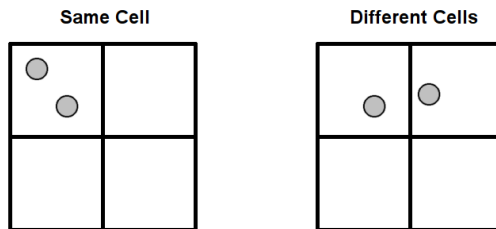


Figure 4.6: Pathological situation regarding the environment of a pair system.

4. THE COSMOLOGICAL ENVIRONMENT AND THE LOCAL GROUP

One of the first considerations that should be taken into account for quantifying the environment of pair systems (*P*, *IP*, *CLG* and *LG* samples), it is that the two halos of the pair may be embedded into different cells, such as it is shown in the Figure 4.6. This pathological situation is presented due to the non-point nature of this type of systems and the finite resolution of the grid.

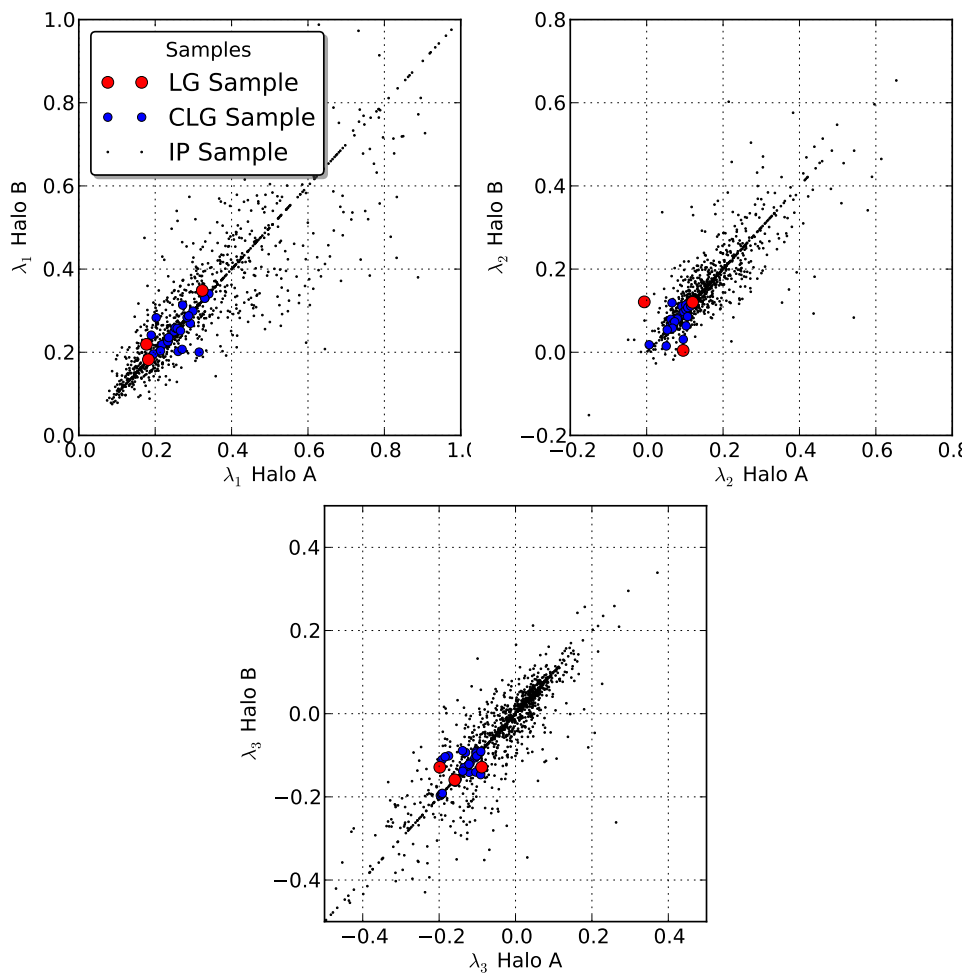


Figure 4.7: Comparison between the distributions of the eigenvalues of the V-web for the two halos of each pair system of the *LG*, *CLG* and *IP* samples.

In order to quantify this effect, in the Figure 4.7 are plotted the distributions of each eigenvalue of the V-web for each one of the halos in the pair samples. The ideal situation, where both halos share the same cell, it would correspond to a

4.2 Properties of the CLG Sample

straight line with a slope of 45° , whereas the pathological situations are responsible of the observed dispersion. A way to solve this issue is to decrease the resolution of the grid, such that both halos are embedded in the same cell, but this would cause a losing of information regarding the local environment of the pair system. Due to the Gaussian softening of one cell size ($\sim 1h^{-1}$ Mpc) that has been applied a priori over the eigenvalues fields, possible variations between neighbour cells are neglected, such as it is shown for the most of *IP* systems in the figure. Taking into account the latter and the local dynamic of pair systems is dominated by the more massive dark halo, by convention it will be taken the host cell of this halo as the representative of the entire system.

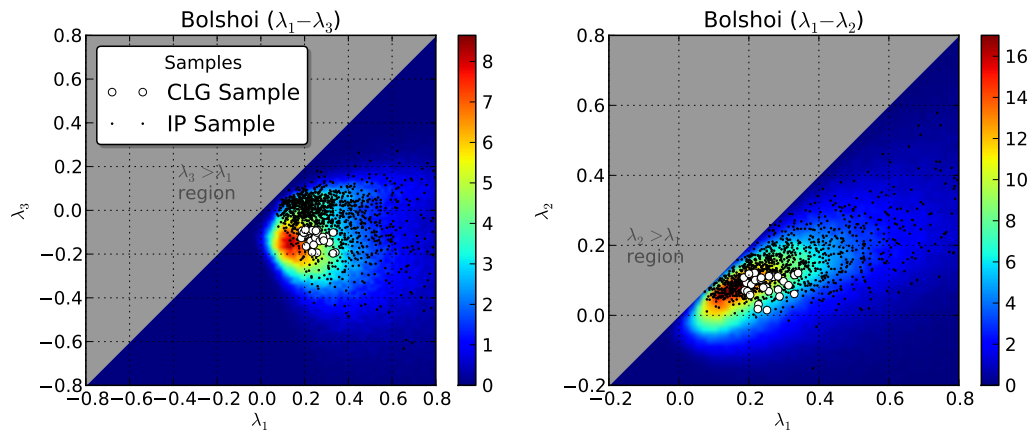


Figure 4.8: 2D distributions of the cosmological environment for the defined samples, $\lambda_1 - \lambda_3$ (left panel) and $\lambda_1 - \lambda_2$ (right panel). The background histogram, plotted in colours, corresponds to the distribution of environment for all the halos in Bolshoi (*GH* sample), its resolution is 100×100 for the shown range and it is normalized with respect to its area. The black dots corresponds to the distribution of the *IP* sample and finally the white dots to the *CLG* sample.

Once it has been determined how to quantify the environment of pair systems, in the Figure 4.8 is illustrated the distribution of the samples *GH*, *IP*, *CLG*. As it has been shown in the subsection 4.1.2, the distribution of environment for halos in Bolshoi are considerably biased with respect to the distribution of the volume cells. In spite of this, and taking into account that the construction of pair systems

4. THE COSMOLOGICAL ENVIRONMENT AND THE LOCAL GROUP

it is made from the sample of halos, it is more interesting to perform comparisons between the distributions associated to halos (coloured histograms in the same figure). As it was defined in the subsection 3.4.2, the *IP* sample is constructed such that it is guaranteed its gravitational isolation with respect to more massive halos and other structures, that is why there are two effects that compete regarding the distribution of environment of these systems. In the first effect, it is expected that the abundance of pairs is more favourable around environments where there are more halos, whereas in the second effect, precisely the over-abundance of halos becomes unfavourable due to the criterion of gravitational isolation. According to the results, the second effect is more dominant on the *IP* sample with respect to all the halos, while for the *P* sample the bias is not longer presented¹

In order to conclude the analysis of the previous figure, it is discussed about the distribution of environment for the *CLG* systems in the Bolshoi simulation. In spite of this distribution is artificially biased because of the selection criterion, it is interesting to notice that the range of the eigenvalues that delimits this sample is relatively reduced, thereby indicating that the three LG-like systems in the CLUES simulations share a similar local dynamic. Although the latter may be an effect established a priori by construction due to the constrained nature of the CLUES simulations, it is still interesting the bias that this feature produces on the distribution of environment of the *CLG* sample regarding all the halos and the *IP* sample.

To quantify the produced biases in each sample regarding a specific type of environment (See Figure 3.9), in the next Figure 4.9 it is plotted the fractions of objects into each type of region. In the optimal range of the threshold value $0.2 \leq \lambda_{th} \leq 0.4$, defined in the subsection 4.1.2, it is noticed important differences between each one of the samples, specially for the *CLG*. As it has been previously mentioned, the effect of the gravitational isolation produces a bias between the distribution of environment of the halos *GH* and the distribution of the *IP* systems. This can be clearly noticed for each one of the number fractions in the optimal range of λ_{th} . In the case of vacuums, the dominant fraction is that associated to *IP*, but in the case of sheet regions, the fraction of both samples are comparable, and even more, in the filament and knot regions, the dominant fractions is that corresponding to halos *GH*. This indicates that *IP* systems are more abundant in regions

¹ The latter is not shown in the Figure 4.8, but it is easily computed.

4.2 Properties of the *CLG* Sample

of low to middle density of halos, but even so, there are still a considerable fraction within sheet and filament regions, so it is not possible to associate a specific type of region to these systems. Finally, the *CLG* systems present an important bias compared with the two previously discussed samples, being specially interesting that produces regarding the *IP* sample, due to the *CLG* sample is a sub-sample of this. Again, taking into account the optimal range of λ_{th} , it is possible, in this case, to associate a certain type of region to the *CLG* sample, being these systems preferentially in sheet and vacuum regions.

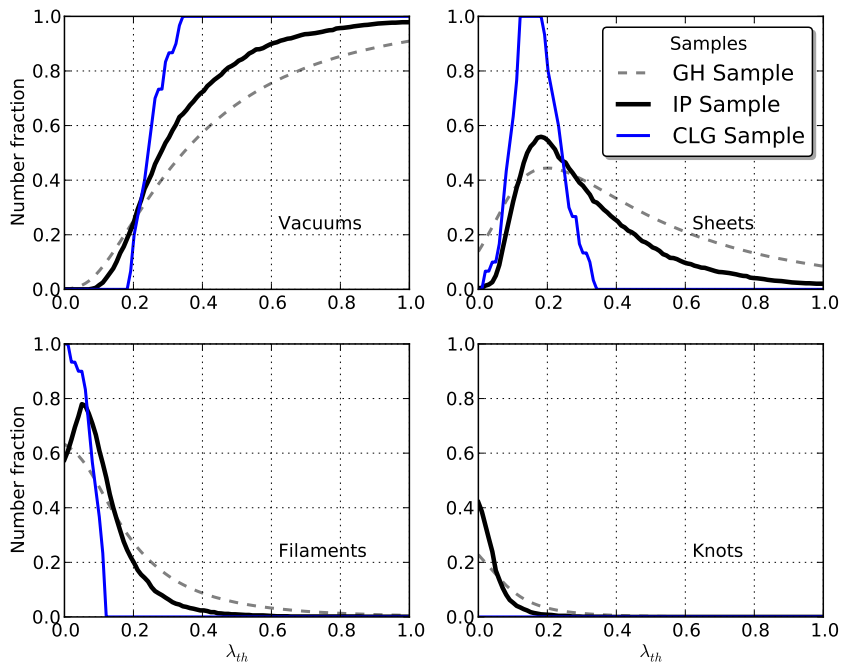


Figure 4.9: Object fractions in different regions in terms of the threshold value λ_{th} . In the case of the *GH* sample, it is counted the number of halos, whereas for the *IP* and *CLG* samples it is counted the number of pair systems.

In spite of the classification scheme used, the above conclusions depend on the selected λ_{th} parameter, and although it has been reasonably bounded in an optimal region where it is reproduced de visual impression, it is still a free parameter. In order to solve this, it is introduced the fractional of anisotropy (FA) with the normalization used in [25]

4. THE COSMOLOGICAL ENVIRONMENT AND THE LOCAL GROUP

$$FA = \frac{1}{\sqrt{3}} \sqrt{\frac{(\lambda_1 - \lambda_3)^2 + (\lambda_2 - \lambda_3)^2 + (\lambda_1 - \lambda_2)^2}{\lambda_1^2 + \lambda_2^2 + \lambda_3^2}} \quad (4.1)$$

This quantity allows to quantify the anisotropy degree of the local cosmic environment, being $FA = 1$ a highly anisotropic region, whereas $F = 0$ is instead a highly isotropic region. Furthermore this quantity is independent of any free parameter chosen a priori. According to the result obtained by [25], regions of low isotropy would correspond to knots due to their characteristic isotropic collapse, while regions of high isotropy would correspond to vacuums due to their non-uniform expansion. In the case of filament and sheet regions, the fractional anisotropy is extendedly distributed over middle values, thus indicating that the dynamic of these type of regions is more complex. Even so, there is a slight tendency towards low values in the case of filaments and high values for sheets.

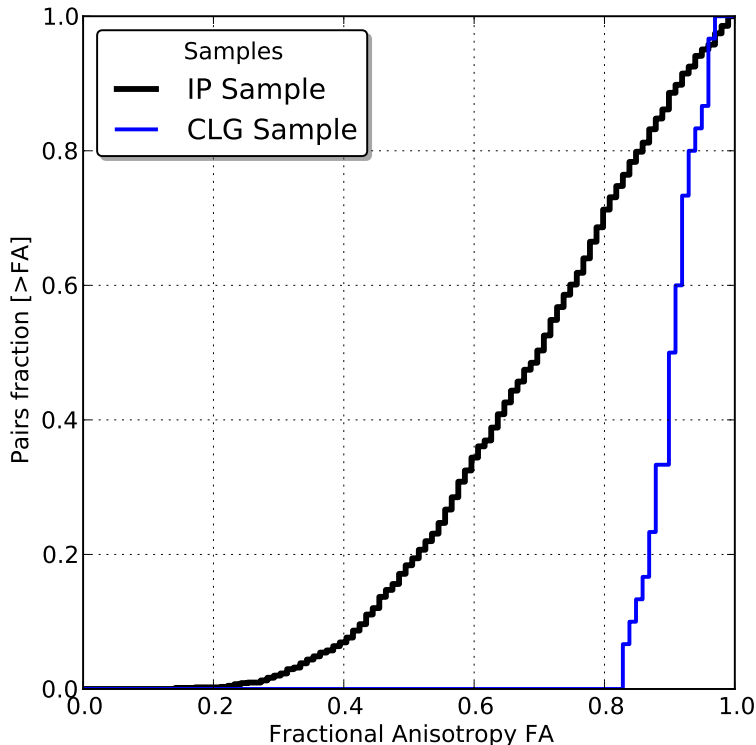


Figure 4.10: Integrated histogram of the fractional anisotropy for the *IP* and *CLG* samples.

4.2 Properties of the *CLG* Sample

In the Figure 4.10, it is calculated the integrated histograms of the fractional anisotropy for the *IP* and *CLG* samples. The first result is associated to the distribution of *IP* systems, which is highly homogeneous for middle values (approximately $0.4 < FA < 0.9$) as it is evidenced by the constant slope in the histogram. This implies that *IP* systems are distributed over middle to high anisotropy regions, in agreement with the number fractions found for vacuums, sheets and filaments. The second result is the bias in the distributions of the fractional anisotropy for the *CLG* sample. Unlike the case for *IP* systems, this distribution is concentrated in high anisotropy regions (approximately $0.8 < FA < 1.0$), what finally confirms that it is possible to associate certain type of cosmological environment to *CLG* systems, being in this case vacuum and sheet regions, or equivalently in terms of the eigen-directions defined by the V-web, regions that expand into two directions (associated to the λ_2 and λ_3 eigenvalues), while there is an expansion/collapse respectively into the third direction (associated to the eigenvalue λ_1).

The main advantage of using the fractional anisotropy lies in this quantity quantifies in just one value the dynamic of the cosmic environment, thereby allowing to establish a more natural and direct framework for studying possible environmental effects on physical quantities.

4.2.2 Mass of *CLG* Systems

As it was demonstrated in the subsection 4.1.1, the distribution of mass of the *GH* sample is consistent for both simulations, therefore it is expected that all the samples, but the *CLG* sample since that requires besides the specific host environment, are also consistent for both simulations. In order to study the mass of pair systems, it is proposed the use of two different quantities, the first one is the total mass of the system $M_{tot} = M_A + M_B$ and the second quantity is the mass ratio $\chi = M_B/M_A$, where by convention M_A is the more massive halo.

The next Figure 4.11 shows the result of calculating the integrated histograms for the total mass and the mass ratio. It is taken the *IP* sample as control sample, furthermore it is shown the obtained values for each one of the Local Groups systems in CLUES.

4. THE COSMOLOGICAL ENVIRONMENT AND THE LOCAL GROUP

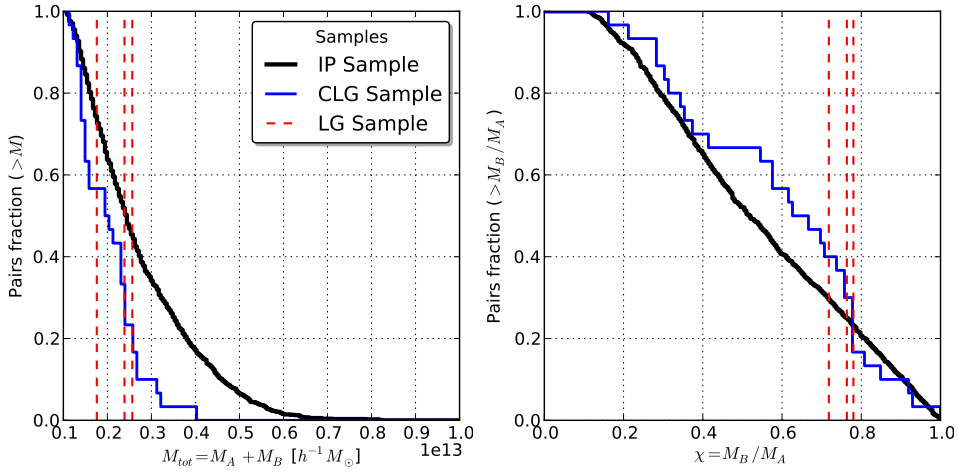


Figure 4.11: Integrated histograms for the total mass $M_A + M_B$ (left panel) and the mass ratio M_B/M_A (right panel), of the pair samples in Bolshoi.

An interesting result of this figure is that the ranges associated to the *LG* sample in CLUES are well-defined (vertical red lines). This evidence that *LG* systems share not only a same cosmological environment but a similar distribution of mass. As a possible explanation to this, it can be considered a selection effect in the samples due to the construction of the constrained simulations, while a more optimist point of view would be considering this as an evidence of a correlation between the mass and the local environment of the pair.

In order to answer the last question, it must be analysed the distribution of both mass parameter for the other samples. In the case of the total mass for *IP* systems, it is distributed according to the same distribution of halos (see Figure 4.2), as it is expected due to there is no restrictions regarding the environment. In the case of the mass ratio, it is obtained a distribution completely homogeneous. Now, for the *CLG* sample, which it is expected to be influenced by the environment, it is obtained a biased distribution of the total mass regarding the *IP* sample and centred approximately in the range defined by the *LG* systems. For the distribution of mass ratios of *CLG* systems, it is also found a uniform behaviour due to the lack of data, in spite of that, there is an apparent over-abundance around the mean value defined by the *LG* systems, but again, there are no data enough in order to conclude a possible relation.

4.2 Properties of the CLG Sample

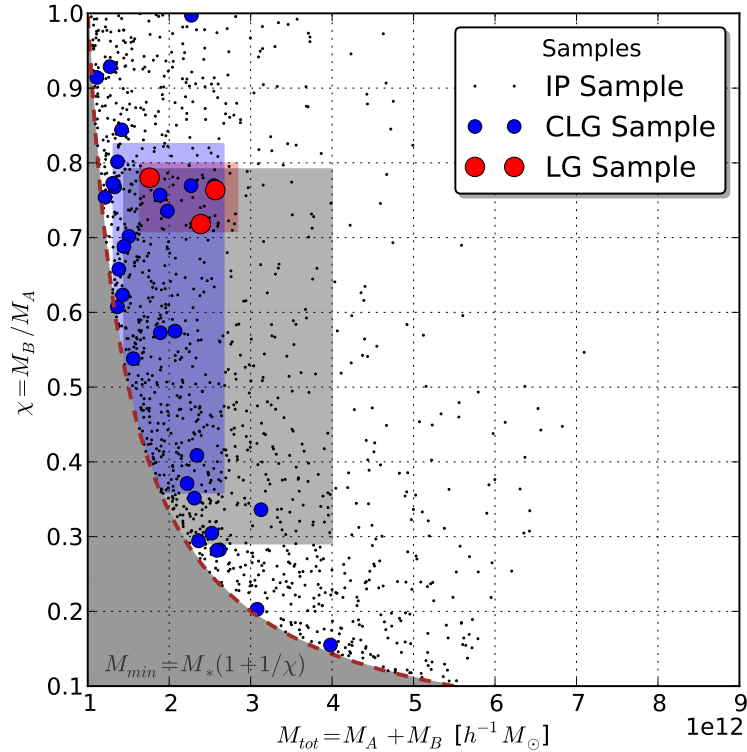


Figure 4.12: Diagram of dispersion for the defined mass parameters (M_{tot}, χ) and for each one of the pair samples. The square regions are made from the mean value and the standard deviation of the respective sample (same colour). The gray regions in the bottom corresponds to a cut off artificially imposed due to the minim mass range of the halos (M_*) for constructing the pair samples.

In the Figure 4.12, it is shown a diagram of dispersion for the mass parameters previously defined for the pair samples. The square regions represent the mean value and one standard deviation regarding the parameters labelled in each axis, what allows comparing the different distributions graphically. From this comparison it is confirmed that the proposed method for constructing *CLG* systems biases the total mass of pair systems within a range consistent with the mass of *LG* systems in the constrained simulations, whereas there is any selection effect regarding the mass ratio χ .

Finally, and with the aim of answering if there is a possible effect due to the local environment on the total mass of *CLG* systems, it is computed in the next

4. THE COSMOLOGICAL ENVIRONMENT AND THE LOCAL GROUP

Figure 4.13 diagrams of correlation between the fractional anisotropy and the mass parameters.

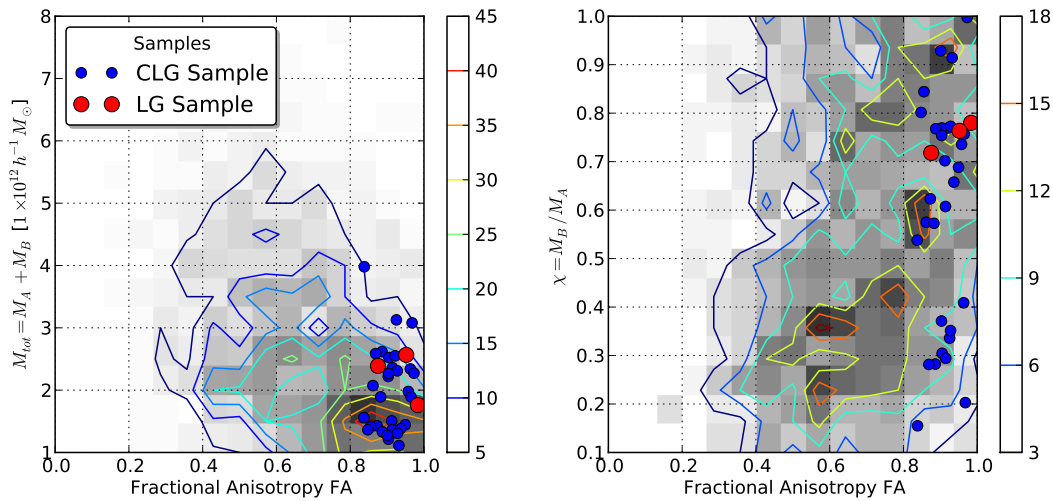


Figure 4.13: Diagrams of dispersion for the fractional anisotropy with respect to the mass parameters. The background map and the contour curves correspond to the *IP* sample.

In the case of the total mass M_{tot} of the *IP* samples, it can be noticed that pairs with low mass values lie preferentially within high anisotropy regions, while pairs with higher mass values lie within middle anisotropy regions. This can be thought as a correlation between the local environment and the total mass for the *IP* sample, whereof it is concluded that the criterion of construction of the *CLG* sample by using the properties of environment of the *LG* systems selects low mass pairs.

For the mass ratio χ , it is noticed a more dispersed distribution for the *IP* sample. In spite of that, it is noticed a slight over-abundance of pairs with low χ values in middle anisotropy regions, while in high anisotropy regions there are more pairs with higher χ values. This is consistent with the performed selection in the *CLG* sample, for which, approximately 66% of the pairs have mass ratio values such that $\chi > 0.5$. From this it can be intuited a possible correlation between the host environment and the mass ratio χ of the pairs, but due to the high dispersion of the distribution and the lack of data, it cannot be concluded.

4.2 Properties of the CLG Sample

4.2.3 Distributions of Energy and Angular Momentum

The energy and the angular momentum are other interesting physical properties of the pair systems. These quantities are defined here from the next expressions

$$e_{tot} = \frac{1}{M_A + M_B} \left[\frac{1}{2} (M_A v_A'^2 + M_B v_B'^2) - G \frac{M_A M_B}{|\mathbf{r}'_A - \mathbf{r}'_B|} \right] \quad (4.2)$$

$$\mathbf{L}_{orb} = \frac{1}{M_A + M_B} [M_A \mathbf{r}'_A \times \mathbf{v}'_A + M_B \mathbf{r}'_B \times \mathbf{v}'_B] \quad (4.3)$$

where \mathbf{r}'_i is the comoving position of the i halo and \mathbf{v}'_i is the total velocity¹ with respect to the center of mass of the pair.

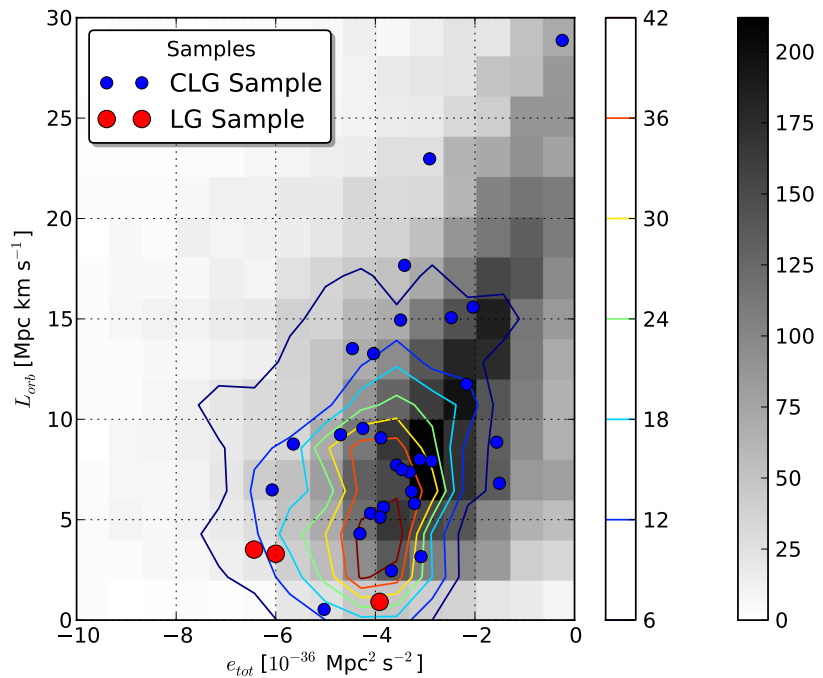


Figure 4.14: Diagram of dispersion for the total energy and the orbital angular momentum of pair systems. The background map corresponds to the distribution of the P sample, while the contour lines to the distribution of the IP sample, in both cases the value corresponds to the number of pairs.

¹ Total velocity because it is included the peculiar term and the Hubble flux with respect to the center of mass of the systems, so $\mathbf{v}'_i = \mathbf{v}_{pec,i} + H_0 \mathbf{r}'_i$.

4. THE COSMOLOGICAL ENVIRONMENT AND THE LOCAL GROUP

In the Figure 4.14 it is shown the distributions of the specific total energy and the specific orbital angular momentum for the samples. The first result that can be noticed is a significant bias between the distribution of the *IP* systems with respect to the *P* sample, what demonstrates that the criterion of gravitational isolation previously defined in the subsection 3.4.2 selects a range of energy and angular momentum lower than the general sample of pairs, being the *IP* gravitationally more bounded. In the case of the *CLG* sample, its distribution is similar to the *IP* one, whereof there is not an apparent selection due to the host environment. Finally, it is interesting to notice that the properties of the three *LG* systems of CLUES are quite similar, thereby indicating that they represent a well-defined type of systems, although as it has been mentioned, this can be a priori effect due to the construction of the CLUES simulations.

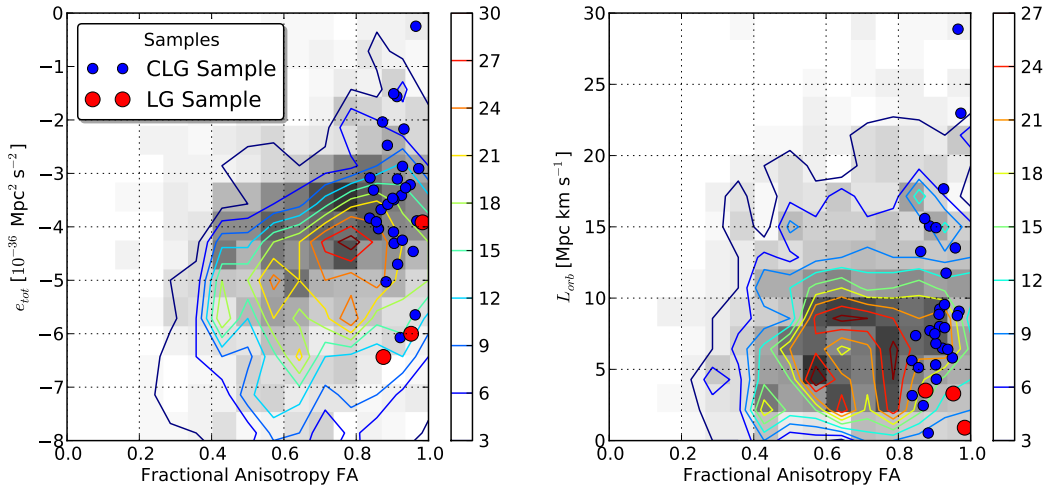


Figure 4.15: Diagrams of dispersion for the fractional anisotropy with respect to the energy and the angular momentum. The background map and the contour curves correspond to the number of pairs of the *IP* sample.

In the Figure 4.15, and with the aim of determining possible correlations, it is calculated diagrams of correlation for the energy and the angular momentum regarding the fractional anisotropy. In the case of the specific energy, *IP* pair systems with higher values of energy (less bounded), seem to be mostly distributed over

4.2 Properties of the *CLG* Sample

high anisotropy regions, whereas low energy systems (more bounded) are preferentially within middle anisotropy regions, what shows a correlation between these two quantities. For *CLG* systems, the selection by using the environment biases the distribution of energy to higher energy values than the mean distribution for *IP* systems, what is consistent with the found correlation. In this case, the *LG* systems seem to not follow this correlation, having much lower values of energy than expected. Finally, for the distribution of specific angular momentum, there is no a clear correlation, being any L_{orb} value of the pairs equally probable for any type of environment.

4.2.4 Angular Momentum Alignment

Finally, the last property to be analysed for the pair systems, it is their alignment regarding the cosmological environment. For this it is defined the angle ϕ_i as the angle formed between the eigen-vector $u_{\lambda i}$ of the V-web and the angular momentum of the i pair system \mathbf{L}_{orb} .

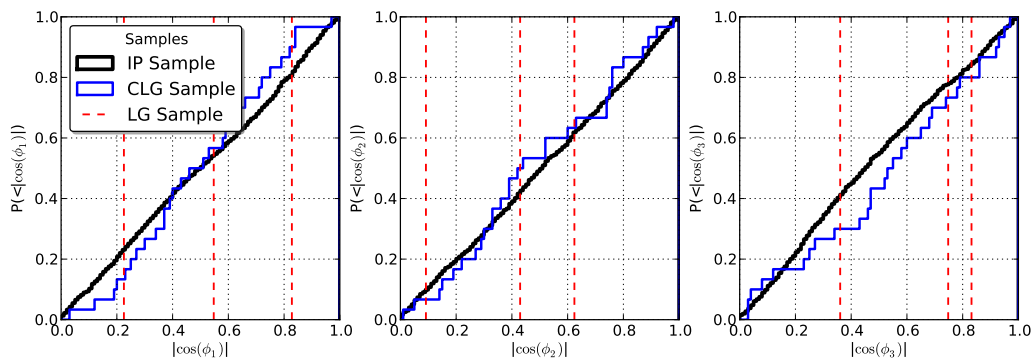


Figure 4.16: Integrated histograms for the angle formed between the angular momentum of each pair, that determines the orbital plane, and each one of the eigen-vectors defined by the V-web regarding the cosmological environment. It is performed for each one of the pair samples, *IP* and *CLG*, whereas the *LG*systems in CLUES are plotted with vertical red dashed lines.

In the Figure 4.16, it is calculated the integrated histograms for each one of the defined angles ϕ_i . As it can be noticed, the *CLG* and *IP* samples are homogeneous regarding the three distributions of angles, thereby indicating that there is no a

4. THE COSMOLOGICAL ENVIRONMENT AND THE LOCAL GROUP

preferred alignment with regard to the cosmological environment. This also is evidenced for the single values of the *LG* systems of the constrained simulations.

4.3 Conclusions

This section is dedicated to compile the main results obtained throughout this work. These results will be enumerated and discussed according to the order in which they were obtained.

- 1.** The method for constructing the *IP* sample was initially proposed by [8] with the aim of reproducing *LG*-like systems. In spite of this, the number of these systems found in the *Bolshoi* simulation is much bigger than that expected according to the abundance of *LG* systems in the constrained simulations. The method proposed here for constructing the *CLG* sample in *Bolshoi* from the cosmological environment of *LG* systems, produces a number of systems that is in agreement with the systems found in the constrained simulations. Moreover, applying this method to the constrained simulations themselves, it is found a *CLG* sample with a similar size to the *LG*.
- 2.** From the mean density values of different regions of the cosmological environment (Figure 4.4), it is proposed a scheme to select an optimal range of the threshold parameter λ_{th} for the V-web, with the aim of reproducing the visual appearance of the cosmic web. This scheme is based upon the minimisation of the mean density in vacuum regions due to the visual impression at large scales is dominated by this type of region. This criterion guarantees that vacuum regions do not invade higher density zones, which at first should be classified as sheets or filaments. This method gives an estimative of the optimal value of the threshold parameter, within a range approximately similar for all the used simulations ($0.2 \leq \lambda_{th} \leq 0.4$), furthermore it is properly reproduced the visual appearance (see Figure 4.5 for $\lambda_{th} = 0.3$). Despite of this, this parameter is still free, therefore it is not viable to use a classification scheme based upon it in order to determine possible correlations over physical properties of pair systems or other cosmological structures. Instead of this, it is introduced the fractional anisotropy normalized as [25].

4.3 Conclusions

3. The distributions of environment for the Bolshoi simulation and for the CLUES simulations differ notably between themselves, existing a pronounced difference between the mean density of vacuums and filaments, whereas this difference is slighter in the CLUES simulations. Despite of this, the volume fractions associated to each type of environment are approximately equal for both simulations in the optimal range of the threshold parameter λ_{th} . Though it is expected that the local dynamic characterized through the V-web scheme is independent of the global structure of the distribution of environment, so it is validated the proposed method to select *CLG* samples in Bolshoi.
4. The method for constructing *CLG* systems selects a common cosmological environment for these systems, being preferred sheet and vacuum regions. These regions present an high anisotropy, quantified by the fractional anisotropy (FA). In the case of *IP* systems, those lie preferentially within middle to high anisotropy regions, associated to low density zones, contrarily to halos, which are within high density and less anisotropic regions, like filaments and knots. Even so, the distribution of environment for *IP* systems is very wide and it cannot be associated to them a certain type of environment. The bias presented between *IP* systems and all the halos is due to the criterion of gravitational isolation used in order to construct the *IP* sample, therefore regions with a high number of halos are not suitable due to the strong gravitational influence.
5. It is found a correlation between the total mass of *IP* systems and the fractional anisotropy of the host environment, where higher values of mass are more abundant in middle anisotropy regions, whereas pairs with smaller values of mass are common in high anisotropy regions. This implies the selection of the environment performed on the *CLG* systems biases the mass into a smaller range than *IP* systems. In the case of the mass ratio, it is not found any significant correlation with respect to the environment, even so, it can be noticed a slight over-abundance of high values of the mass ratio in high anisotropy regions, but it is necessary more data in order to have a robust statistic and a definitive conclusion.

4. THE COSMOLOGICAL ENVIRONMENT AND THE LOCAL GROUP

6. It has been found a correlation between the specific energy of *IP* systems and the host environment, obtaining high energy values in high anisotropy regions and lower values in middle anisotropy zones. This correlation selects a range of energy for *CLG* systems, although this range is not consistent with the range defined by the *LG* in CLUES. For the angular momentum it is not found any correlation with respect to the environment
7. Finally, it is found that there are not preferred alignments between the angular momentum (orbital plane) for *CLG* pair systems and the directions defined by the eigen-vector of the V-web

Bibliography

- [1] A.W. Appel. *Undergraduate Thesis, Princeton University*. SIAM J. Sci. Stat. Comput. 6, 85, 1985. 48
- [2] J. Barnes and P. Hut. A hierarchical $o(n \log n)$ force-calculation algorithm. *Nature*, 324:446–449, 1986. 48
- [3] J. Binney and S. Tremaine. *Galactic Dynamics*. Princeton University Press, USA, second edition, 2008. ISBN 978-0-691-13027-9. 42
- [4] H. Curtis. The scale of the universe. *Bull. Nat. Res. Coun*, 2:171, 1921. 3
- [5] J.M. Dawson. Particle simulation of plasmas. *Reviews of Modern Physics*, 55:403–447, 1983. 44
- [6] A. Einstein. Grundlage der allgemeinen relativitätstheorie. *Annalen der Physik*, 49(4):769–822, 1916. 3
- [7] J. Forero-Romero, Y. Hoffman, S. Gottlöber, A. Klypin, and G. Yepes. A dynamical classification of the cosmic web. *Mon.Not.Roy.Astron.Soc*, 396: 1815–1824, 2009. 56
- [8] J. Forero-Romero, Y. Hoffman, G. Yepes, S. Gottlöber, R. Piontek, A. Klypin, and M. Steinmetz. The dark matter assembly of the local group in constrained cosmological simulations of a lambda cold dark matter universe. *Mon.Not.Roy.Astron.Soc*, 417:1434–1443, 2011. 60, 61, 86

BIBLIOGRAPHY

- [9] J.E. Forero-Romero, Y. Hoffman, S. Bustamante, S. Gottlöber, and G. Yepes. The kinematics of the local group in a cosmological context. *Accepted to publication in ApJ Letters*, 2013. 8, 61
- [10] A. Friedman. On the curvature of space. *General Relativity and Gravitation*, 31:1991, 1999. 4
- [11] A. Friedman. On the possibility of a world wih constant negative curvature of space. *General Relativity and Gravitation*, 31:2009, 1999. 4
- [12] S. Gottlöber, Y. Hoffman, and G. Yepes. Constrained local universe simulations (clues). *Proceedings of High Performance Computing in Science and Engineering*, pages 309–322, 2010. 53
- [13] O. Hahn, C. Porciani, M. Carollo, and A. Dekel. Properties of dark matter haloes in clusters, filaments, sheets and voids. *Mon.Not.Roy.Astron.Soc*, 375: 489–499, 2007. 54
- [14] W. Herschel. On the construction of the heavens. *Philosophical Transactions of the Royal Society of London*, 75(I):213–266, 1785. v, 2
- [15] R.W. Hockney and J.W. Eastwood. *Computer Simulation Using Particles*. IOP Publishing Ltd, Great Britain, first edition, 1988. ISBN 0-85274-392-0. 46
- [16] Y. Hoffman and E. Ribak. Constrained realizations of gaussian fields: A simple algorithm. *ApJ*, 380:L5–L8, 1991. 52
- [17] Y. Hoffman, O. Metuki, G. Yepes, G. Gottlöber, J. Forero-Romero, N. Libeskind, and A. Knebe. A kinematical classification of the cosmic web. *Mon.Not.Roy.Astron.Soc*, 425:2049–2057, 2012. 56
- [18] E.P. Hubble. Extragalactic nebulae. *ApJ*, 64:321–369, 1926. 3
- [19] J.D. Jackson. *Classical Electrodynamics*. John Wiley & Sons, Inc., USA, third edition, 1999. ISBN 0-471-30932-X. 28

BIBLIOGRAPHY

- [20] N. Jarosik et al. Seven-year wilkinson microwave anisotropy probe (wmap) observations: Sky maps, systematic errors, and basic results. *ApJS*, 192:14, 2011. 10, 21
- [21] J.G. Jernigan. Dynamic of star clusters. *IAU Symposium 113*, page 131, 1985. 48
- [22] A. Klypin, Y. Hoffman, A. Kravtsov, and S. Gottlöber. Constrained simulations of the real universe: the local supercluster. *ApJ*, 596:19–33, 2003. vii, 51, 52
- [23] A.A. Klypin, S. Trujillo-Gomez, and J. Primack. Dark matter halos in the standard cosmological model: Results from the bolshoi simulation. *ApJ*, 740:102, 2011. 50
- [24] G. Lemson and G. Kauffmann. Environmental influences on dark matter halos and consequences for the galaxies within them. *Mon.Not.Roy.Astron.Soc*, 302:111, 1999. 66
- [25] N. Libeskind, Y. Hoffman, J. Forero-Romero, S. Gottlöber, A. Knebe, M. Steinmetz, and A. Klypin. The velocity shear tensor: tracer of halo alignment. *Mon.Not.Roy.Astron.Soc*, 428:2489–2499, 2013. 66, 69, 77, 78, 86
- [26] M.S. Longair. *Galaxy Formation*. Springer, New York, second edition, 2008. ISBN 978-3-540-73477-2. vi, 2, 3, 13, 15, 17, 18, 19, 21, 24, 26, 36, 39
- [27] T. Padmanabhan. *Structure Formation in the Universe*. Cambridge University Press, Great Britain, first edition, 1995. ISBN 0-521-42486-0. 13, 19, 20, 23, 32, 34, 39, 43
- [28] R.K. Pathria. *Statistical Mechanics*. Butterworth-Heinemann, Great Britain, second edition, 1996. ISBN 0-7506-2409-8. 28
- [29] S. Pfalzner and P. Gibbon. *Many-Body Tree Methods in Physics*. Cambridge University Press, USA, first edition, 1996. ISBN 0-521-49564-4. 42, 45, 48
- [30] D. Porter. *PhD Thesis*. University of California, Berkeley, 1985. 48

BIBLIOGRAPHY

- [31] W. Press and P. Schechter. Formation of galaxies and clusters of galaxies by self-similar gravitational condensation. *ApJ*, 187:425–438, 1974. 67
- [32] H. Shapley. The scale of the universe. *Bull. Nat. Res. Coun*, 2:164, 1921. 3
- [33] S. Weinberg. *Gravitation and Cosmology: Principles and Applications of the General Theory of Relativity*. John Wiley & Sons, Inc., New York, first edition, 1972. ISBN 0-471-92567-5. 14, 16
- [34] A. Yoshisato, M. Morikawa, N. Gouda, and H. Mouri. Why is the zel'dovich approximation so accurate? *ApJ*, 637:555–560, 2006. 38
- [35] S. Zaroubi, Y. Hoffman, and A. Dekel. Wiener reconstruction of large-scale structure from peculiar velocities. *ApJ*, 520:413–425, 1999. 52
- [36] Y.B. Zeldovich. Gravitational instability: an approximate theory for large density perturbations. *Astronomy and Astrophysics*, 5:84–89, 1970. 38